

University of Kentucky

UKnowledge

Theses and Dissertations--Earth and
Environmental Sciences

Earth and Environmental Sciences


2021

Admittance Modeling for Elastic Thickness Across the Mars Crustal Dichotomy Boundary

Aspen Davis

University of Kentucky, adavis1@alumni.mines.edu

Author ORCID Identifier:

 <https://orcid.org/0000-0001-6398-9723>

Digital Object Identifier: <https://doi.org/10.13023/etd.2021.331>

[Right click to open a feedback form in a new tab to let us know how this document benefits you.](#)

Recommended Citation

Davis, Aspen, "Admittance Modeling for Elastic Thickness Across the Mars Crustal Dichotomy Boundary" (2021). *Theses and Dissertations--Earth and Environmental Sciences*. 87.

https://uknowledge.uky.edu/ees_etds/87

This Master's Thesis is brought to you for free and open access by the Earth and Environmental Sciences at UKnowledge. It has been accepted for inclusion in Theses and Dissertations--Earth and Environmental Sciences by an authorized administrator of UKnowledge. For more information, please contact UKnowledge@lsv.uky.edu.

STUDENT AGREEMENT:

I represent that my thesis or dissertation and abstract are my original work. Proper attribution has been given to all outside sources. I understand that I am solely responsible for obtaining any needed copyright permissions. I have obtained needed written permission statement(s) from the owner(s) of each third-party copyrighted matter to be included in my work, allowing electronic distribution (if such use is not permitted by the fair use doctrine) which will be submitted to UKnowledge as Additional File.

I hereby grant to The University of Kentucky and its agents the irrevocable, non-exclusive, and royalty-free license to archive and make accessible my work in whole or in part in all forms of media, now or hereafter known. I agree that the document mentioned above may be made available immediately for worldwide access unless an embargo applies.

I retain all other ownership rights to the copyright of my work. I also retain the right to use in future works (such as articles or books) all or part of my work. I understand that I am free to register the copyright to my work.

REVIEW, APPROVAL AND ACCEPTANCE

The document mentioned above has been reviewed and accepted by the student's advisor, on behalf of the advisory committee, and by the Director of Graduate Studies (DGS), on behalf of the program; we verify that this is the final, approved version of the student's thesis including all changes required by the advisory committee. The undersigned agree to abide by the statements above.

Aspen Davis, Student

Dr. Dhananjay Ravat, Major Professor

Dr. Michael McGlue, Director of Graduate Studies

ADMITTANCE MODELING FOR ELASTIC THICKNESS
ACROSS THE MARS CRUSTAL DICHOTOMY BOUNDARY

THESIS

A thesis submitted in partial fulfillment of the
requirements for the degree of Master of Science in the
College of Arts and Sciences
at the University of Kentucky

By

Aspen Davis

Lexington, Kentucky

Director: Dr. Dhananjay Ravat, Professor of Geophysics

Lexington, Kentucky

2021

Copyright © Aspen Davis 2021
<https://orcid.org/0000-0001-6398-9723>

ABSTRACT OF THESIS

ADMITTANCE MODELING FOR ELASTIC THICKNESS ACROSS THE MARS CRUSTAL DICHOTOMY BOUNDARY

We use a Bouguer mass-sheet approximation for spectral admittance and correlation modeling to estimate elastic thickness, crustal thickness, crustal density, and load density across the Mars crustal dichotomy boundary near the landing site of NASA's InSight Lander. We derive and constrain the parameter ranges using RMS misfit between the observed and theoretical admittance and their error bars. Spherical cap windows of 15° (900 km) radius are used to study 15 locations in the Northern Lowlands, the Southern Highlands and near and on the boundary which suggest distinct, but not sharp, difference in lithospheric properties. Elastic thickness estimates range generally between 0 and 30km in the Northern Lowlands, between 0 and 50km in the South Highlands and between 0 and 40km on the boundary itself. Crustal density varies from generally $2300\text{-}2900\text{kgm}^{-3}$ in the Northern Lowlands to $2200\text{-}2500\text{kgm}^{-3}$ in the Southern Highlands with intermediate values of $2200\text{-}2600\text{kgm}^{-3}$ directly on the boundary. It was not possible to adequately constrain well the surface (load) density for any of regions studied. No elastic thickness estimates for this region were thicker than 50km and the elastic thickness was always smaller than the crustal thickness. This region of the Northern Lowlands could have originally had similar elastic thickness as the neighboring Southern Highlands, and the large impacts that re-molded the northern hemisphere into the Northern Lowlands may have also increased the crustal density and reduced elastic thickness. In a couple of locations on the Highlands, however, the elastic thickness is small and these parts could have been weakened by local tectono-thermal processes after the formation of the boundary.

KEYWORDS: Mars, crustal dichotomy boundary, elastic thickness, admittance modeling, crustal thickness, crustal density

Aspen Davis

(Name of Student)

7/30/2021

Date

ADMITTANCE MODELING FOR ELASTIC THICKNESS
ACROSS THE MARS CRUSTAL DICHOTOMY BOUNDARY

By
Aspen Davis

Dr. Dhananjay Ravat
Director of Thesis

Dr. Michael McGlue
Director of Graduate Studies

7/30/2021
Date

ACKNOWLEDGMENTS

Throughout the writing of this thesis, I have received invaluable assistance from a number of individuals who have helped me grow as a scientist and person. This work would not have been possible without the diligent advisement of my advisor, Dr. Dhananjay Ravat. I am immensely grateful for the opportunity to have learned an incredible amount from him and to get to work on this project. I also thank him for being an excellent example of a professor who is dedicated to students learning and for taking me on as a student. Additionally, I am very thankful for my committee members, Dr. Keely O'Farrell, Dr. Ed Woolery and Dr. David Clark for their advisement.

Much of my conceptual understanding of the Mars elastic thickness problem, how to create codes for this problem and practically interpret the results would not have been possible without the outstanding help through correspondence with Dr. Mark Wieczorek and Dr. Adrien Broquet. Their insight was truly essential to the success of this project and I can not express adequate thanks for their open communication. I would also like to thank my lab peer, Dr. Ratheesh Kumar, for many exciting and insightful conversations regarding aspects of elastic thickness and planetary science. It was a sincere pleasure to work in the lab with him and benefit from his creativity.

I could not have finished the program or this work without the unfailing support and comradery of the graduate students in our department. I would like to thank all those involved in G3 leadership and participation, particularly Alex Reis, Autumn Helfrich, Edward Lo, Hillary Johnson, Felicia Harris, Mitchell Clay, Hilary Johnson and Leandro Luz for keeping the spirit of community alive through incredibly difficult times.

To Dr. Mike McGlue, thank you for trusting me to coordinate Rast-Holbrook Seminar Series with G3, and the first ReSEES with co-chair Cooper Cearley. These opportunities became true passion projects throughout much of my time in the department and I never could have imagined how much I would learn from the experiences. Thank you to every single person who had a hand in making these events two of my proudest accomplishments.

I would also like to thank all members of AWG, specifically Gina Lukoczki, Sarah Arpin and Antonia Bottoms for exhibiting the finest quality of leadership in every regard. The three of you have provided *invaluable* representation and hope for me throughout this program. Thank you for inspiring me to continue working towards creating a more inclusive STEM environment for future female and minority scientists.

TABLE OF CONTENTS

ACKNOWLEDGMENTS.....	iii
LIST OF TABLES	vii
LIST OF FIGURES.....	viii
CHAPTER 1. INTRODUCTION.....	1
1.1 <i>Significance</i>	1
1.2 <i>Geologic History</i>	4
1.3 <i>Crustal Dichotomy Boundary</i>	6
1.4 <i>Elastic Thickness</i>	7
1.5 <i>Spherical Harmonics</i>	11
CHAPTER 2. DATA AND SOFTWARE PROGRAMS.....	16
2.1 <i>Topography and Gravity Models</i>	16
2.2 <i>SHTOOLS, GMT and other software</i>	16
CHAPTER 3. METHODS.....	18
3.1 <i>Mass-sheet approximation gravitational potential transfer function</i>	18
3.1.1 <i>Surface Loading</i>	21
3.2 <i>Admittance model</i>	23
3.3 <i>Localization and study locations</i>	26
3.4 <i>Selection Criteria</i>	30
3.5 <i>Error and Noise</i>	32
CHAPTER 4. RESULTS.....	34
4.1 <i>Admittance modeling in the Southern Highlands south of the CDB</i>	34
4.2 <i>Admittance modeling in the Northern Lowlands north of the CDB</i>	52
4.3 <i>Special Cases</i>	65
4.3.1 <i>Locations centered on the CDB</i>	65
4.3.2 <i>Window of 30° spherical cap angular radius</i>	73
CHAPTER 5. DISCUSSION	79
5.1 <i>Lithospheric properties across the CDB</i>	79

5.1.1	Crustal Thickness	79
5.1.2	Crustal Density	83
5.1.3	Load Density	85
5.1.4	Elastic Thickness.....	85
5.2	<i>Effect of increased window size</i>	91
5.3	<i>Suitability of the mass-sheet approximation for admittance modeling</i>	92
5.4	<i>Inclusion of subsurface loads</i>	95
CHAPTER 6. CONCLUSION		98
APPENDIX A.		101
Examples of spectra that are acceptable within error estimates of both observed and theoretical admittance curves		101
APPENDIX B		106
VITA		110

LIST OF TABLES

Table 3.1 – Parameters, symbolic representation, value range and units for parameters used in calculation of mass – sheet approximation based theoretical admittance.	19
Table 4.1 Study locations, spectral range, and acceptable parameter ranges of elastic thickness, load density, crustal thickness and crustal density estimates.	64
Table 4.2 Study locations on the CDB and their spectral range used, and acceptable parameter ranges of elastic thickness, load density, crustal thickness and crustal density estimates.	78

LIST OF FIGURES

Figure 1.1 Mars surface features with shaded MOLA topography. Low topography is colored in blue and high topography is in red. Approximate outline of crustal dichotomy boundary shown by dashed line. Star shows location of Insight landing site and diamond shows Perseverance.....	2
Figure 1.2 GMM-3 free-air gravity anomaly map of Mars from Genova et al. (2016).	3
Figure 1.3 Bouguer gravitational anomaly of Mars over shaded relief from Genova et al. (2016).	4
Figure 1.4 Conceptual visualization of elastic thickness (T_e) and its relation to gravity anomalies on Mars. The left endmember represents a case of no elastic thickness, where there is full Airy isostatic compensation. This will create the free air and bouguer anomalies.....	9
Figure 1.5 Observed global admittance signal (black) and observed global correlation (blue). The gravitational model used is GMM3.	14
Figure 3.1 Global theoretical admittance model showing the dependency of the model on load density, elastic thickness, crustal density and crustal thickness. In all panels, only one parameter is varied while the rest are held constant at $\rho_l=2900\text{kgm}^{-3}$, $\rho_c=3300\text{kgm}^{-3}$, $T_e=50\text{km}$, and $T_c=57\text{km}$. The theoretical model has a visible dependency on each of the parameters being tested.	24
Figure 3.2 Main study locations shown on MOLA topography and intensity. Crustal dichotomy boundary is approximated by red dashed line with Elysium and Hellas locations noted. Insight and Perseverance landing sites are shown by white star and black outline star.	29
Figure 3.3 Main study locations shown on GMM3 free-air gravitational anomaly. Crustal dichotomy boundary is approximated by white dashed line with Elysium and Hellas locations noted. Insight and Perseverance landing sites are shown by white star and black outline star. Cool colors refer to larger, negative free-air gravitational anomaly while hotter colors refer to large positive anomalies.	30
Figure 4.1 Observed (light blue) and theoretical (black) admittance for the 15° spherical cap windowed region centered at 10°S , 98°E . Overlapping parts of observed and theoretical admittances are shown in red on the theoretical spectrum. (a) the minimum RMS case and (b) a case of an ill-fitting spectrum outside of the acceptable criteria range. Elastic thickness, crustal thickness, load density, crustal density and the spectral range used for each theoretical curve are noted. Theoretical degree correlation is shown in dark blue. Vertical bars are standard error estimates on the spectra.	36
Figure 4.2 RMS of the parameter space of crustal thickness, elastic thickness, and load density at location 10°S , 98°E . This plot uses a constant crustal density of 2500kgm^{-3} , which corresponds to the crustal density yielding the lowest RMS parameter combination (noted by the black circle, corresponding to Figure 4.1a).	39

Figure 4.3 Observed (light blue) and theoretical (black) admittance for the 15° spherical cap windowed region centered at 11°S, 116°E. Overlapping parts of observed and theoretical admittances are shown in red on the theoretical spectrum. (a) the minimum RMS case and (b) a case of an ill-fitting spectrum outside of the acceptable criteria range. Elastic thickness, crustal thickness, load density, crustal density and the spectral range used for each theoretical curve are noted. Theoretical degree correlation is shown in dark blue. Vertical bars are error estimates on the spectra..... 40

Figure 4.4 RMS of the parameter space of crustal thickness, elastic thickness, and load density at location 11°S, 116°E. This plot uses a constant crustal density of 2400kgm⁻³, which corresponds to the crustal density yielding the lowest RMS parameter combination (noted by the black circle, corresponding to Figure 4.3a)..... 42

Figure 4.5 Observed (light blue) and theoretical (black) admittance for the 15° spherical cap windowed region centered at 18°S, 132°E. Overlapping parts of observed and theoretical admittances are shown in red on the theoretical spectrum. (a) the minimum RMS case and (b) a case of an ill-fitting spectrum outside of the acceptable criteria range. Elastic thickness, crustal thickness, load density, crustal density and the spectral range used for each theoretical curve are noted. Theoretical degree correlation is shown in dark blue. Vertical bars are error estimates on the spectra..... 43

Figure 4.6 RMS space of crustal thickness, elastic thickness, and load density at location 18°S, 132°E. This plot uses a constant crustal density of 2500kgm⁻³, which corresponds to the crustal density leading to the lowest RMS parameter combination (noted by the black circle, corresponding to Figure 4.5a). 44

Figure 4.7 Observed (light blue) and theoretical (black) admittance for the 15° spherical cap windowed region centered at 24°S, 149°E. Overlapping parts of observed and theoretical admittances are shown in red on the theoretical spectrum. (a) the minimum RMS case and (b) a case of an ill-fitting spectrum outside of the acceptable criteria range. Elastic thickness, crustal thickness, load density, crustal density and the spectral range used for each theoretical curve are noted. Theoretical degree correlation is shown in dark blue. Vertical bars are error estimates on the spectra..... 45

Figure 4.8 RMS space of crustal thickness, elastic thickness, and load density at location 24°S, 149°E. This plot uses a constant crustal density of 2300kgm⁻³, which corresponds to the crustal density leading to the lowest RMS parameter combination (noted by the black circle, corresponding to Figure 4.7a). 47

Figure 4.9 Observed (light blue) and theoretical (black) admittance for the 15° spherical cap windowed region centered at 32°S, 165°E. Overlapping parts of observed and theoretical admittances are shown in red on the theoretical spectrum. (a) the minimum RMS case and (b) a case of an ill-fitting spectrum outside of the acceptable criteria range. Elastic thickness, crustal thickness, load density, crustal density and the spectral range used for each theoretical curve are noted. Theoretical degree correlation is shown in dark blue. Vertical bars are error estimates on the spectra..... 48

Figure 4.10 RMS space of crustal thickness, elastic thickness, and load density at location 32°S, 165°E. This plot uses a constant crustal density of 2300kgm⁻³, which corresponds to the crustal density leading to the lowest RMS parameter combination (noted by the black circle, corresponding to Figure 4.9a). 49

Figure 4.11 Observed (light blue) and theoretical (black) admittance for the 15° spherical cap windowed region centered at 24°S, 185°E. Overlapping parts of observed and theoretical admittances are shown in red on the theoretical spectrum. (a) the minimum RMS case and (b) a case of an ill-fitting spectrum outside of the acceptable criteria range. Elastic thickness, crustal thickness, load density, crustal density and the spectral range used for each theoretical curve are noted. Theoretical degree correlation is shown in dark blue. Vertical bars are error estimates on the spectra..... 50

Figure 4.12 RMS space of crustal thickness, elastic thickness, and load density at location 24°S, 185°E. This plot uses a constant crustal density of 2400kgm⁻³, which corresponds to the crustal density leading to the lowest RMS parameter combination (noted by the black circle, corresponding to Figure 4.11a). 51

Figure 4.13 Observed admittance spectra for 20°N, 98°E. Error bars are standard error as in the other figures..... 52

Figure 4.14 Observed (light blue) and theoretical (black) spectra for 19°N, 116°E. The modeled degree range is in red with theoretical correlation in dark blue. The parameter values used to produce each theoretical curve are given on the figure. (a) minimum RMS case and (b) trial of a model attempting to fit the first peak in the observed spectrum. Theoretical degree correlation is shown in dark blue. Vertical bars are standard error estimates on the spectra..... 53

Figure 4.15 RMS space of crustal thickness, elastic thickness, and load density at location 19°S, 116°E. This plot uses a constant crustal density of 2600kgm⁻³, which corresponds to the crustal density leading to the lowest RMS parameter combination (noted by the black circle, corresponding to Figure 4.15a). 54

Figure 4.16 Observed (light blue) and theoretical (black) spectra for 12°N, 132°E. The modeled degree range is in red with theoretical correlation in dark blue. The parameter values used to produce each theoretical curve are given on the figure. (a) the minimum RMS case and (b) a case of an ill-fitting spectrum outside of the acceptable criteria range. Theoretical degree correlation is shown in dark blue. Vertical bars are standard error estimates on the spectra..... 55

Figure 4.17 RMS space of crustal thickness, elastic thickness, and load density at location 12°S, 132°E. This plot uses a constant crustal density of 2900kgm⁻³, which corresponds to the crustal density leading to the lowest RMS parameter combination (noted by the black circle, corresponding to Figure 4.17a)..... 56

Figure 4.18 Observed (light blue) and theoretical (black) spectra for 5°N, 149°E. The modeled degree range is in red with theoretical correlation in dark blue. The parameter values used to produce each theoretical curve are given on the figure. (a) the minimum RMS case and (b) a case of an ill-fitting spectrum outside of the acceptable criteria range. Theoretical degree correlation is shown in dark blue. Vertical bars are standard error estimates on the spectra..... 57

Figure 4.19 RMS space of crustal thickness, elastic thickness, and load density at location 5°S, 149°E. This plot uses a constant crustal density of 2700kgm⁻³, which corresponds to the crustal density leading to the lowest RMS parameter combination (noted by the black circle, corresponding to Figure 4.18a). 58

Figure 4.20 Observed (light blue) and theoretical (black) spectra for 2°S, 185°E. The modeled degree range is in red with theoretical correlation in dark blue. The parameter values used to produce each theoretical curve are given on the figure. (a) the minimum RMS case and (b) a case of an ill-fitting spectrum outside of the acceptable criteria range. Theoretical degree correlation is shown in dark blue. Vertical bars are standard error estimates on the spectra. 59

Figure 4.21 RMS space of crustal thickness, elastic thickness, and load density at location 2°S, 185°E. This plot uses a constant crustal density of 2600kgm⁻³, which corresponds to the crustal density leading to the lowest RMS parameter combination (noted by the black circle, corresponding to Figure 4.21a). 60

Figure 4.22 Observed (light blue) and theoretical (black) spectra for 1°N, 200°E. The modeled degree range is in red with theoretical correlation in dark blue. The parameter values used to produce each theoretical curve are given on the figure. (a) the minimum RMS case and (b) a case of an ill-fitting spectrum outside of the acceptable criteria range. Theoretical degree correlation is shown in dark blue. Vertical bars are standard error estimates on the spectra. 61

Figure 4.23 RMS space of crustal thickness, elastic thickness, and load density at location 1°S, 200°E using spectral degrees 30 - 50. This plot uses a constant crustal density of 2400kgm⁻³, which corresponds to the crustal density leading to the RMS parameter combination shown in Figure 4.22a. 62

Figure 4.24 RMS space of crustal thickness, elastic thickness, and load density at location 1°S, 200°E using spectral degrees 40 - 60. This plot uses a constant crustal density of 2500kgm⁻³, which corresponds to the crustal density leading to the lowest RMS with reasonable parameter combination (noted by the black circle, corresponding to Figure 4.22b). 63

Figure 4.25 Special cases spherical cap window locations on Mola intensity and topography. White star denotes Insight landing spot, black outline star shows Perseverance rover landing spot and red dashed line approximates the CDB. The large circle shows the spherical cap of radius 30° centered on 32°S, 165°E that is discussed in section 4.3.2. 66

Figure 4.26 Special cases spherical cap window locations on GMM3 free air gravity anomaly. White star denotes Insight landing spot, black outline star shows Perseverance rover landing spot and white dashed line approximates the CDB. 67

Figure 4.27 Observed (light blue) and theoretical (black) spectra for 7°N, 119°E. The modeled degree range is in red with theoretical correlation in dark blue. The parameter values used to produce each theoretical curve are given on the figure. (a) the minimum RMS case and (b) a case of an ill-fitting spectrum outside of the acceptable criteria range. Theoretical degree correlation is shown in dark blue. Vertical bars are standard error estimates on the spectra. 68

Figure 4.28 RMS space of crustal thickness, elastic thickness, and load density at location 7°N, 119°E. This plot uses a constant crustal density of 2200kgm⁻³, which corresponds to the crustal density leading to the lowest RMS parameter combination (noted by the black circle, corresponding to Figure 4.27b). 69

Figure 4.29 Observed (light blue) and theoretical (black) spectra for 2°S, 132°E. The modeled degree range is in red with theoretical correlation in dark blue. The parameter values used to produce each theoretical curve are given on the figure. (a) the minimum RMS case and (b) a case of an ill-fitting spectrum outside of the acceptable criteria range. Theoretical degree correlation is shown in dark blue. Vertical bars are standard error estimates on the spectra. 70

Figure 4.30 RMS space of crustal thickness, elastic thickness, and load density at location 2°S, 132°E. This plot uses a constant crustal density of 2500kgm⁻³, which corresponds to the crustal density leading to the lowest RMS parameter combination (noted by the black circle, corresponding to Figure 4.29b). 71

Figure 4.31 Observed (light blue) and theoretical (black) spectra for 9°S, 149°E. The modeled degree range is in red with theoretical correlation in dark blue. The parameter values used to produce each theoretical curve are given on the figure. (a) the minimum RMS case and (b) an attempt to model the peak from degrees 30 to 50, but does not fit observed admittance for the range of degrees 50 - 100. Theoretical degree correlation is shown in dark blue. Vertical bars are standard error estimates on the spectra. 72

Figure 4.32 RMS space of crustal thickness, elastic thickness, and load density at location 9°S, 149°E. This plot uses a constant crustal density of 2400kgm⁻³, which corresponds to the crustal density leading to the lowest RMS parameter combination (noted by the black circle, corresponding to Figure 4.31b). 73

Figure 4.33 Observed (light blue) and theoretical (black) spectra for 32°S, 165°E using spectral degrees 40 to 65 and a 30° angular radius of the spherical cap window. The modeled degree range is in red with theoretical correlation in dark blue. The parameter values used to produce each theoretical curve are given on the figure. (a) the minimum RMS case and (b) a case of an ill-fitting spectrum outside of the acceptable criteria range. Theoretical degree correlation is shown in dark blue. Vertical bars are standard error estimates on the spectra. 75

Figure 4.34 Observed (light blue) and theoretical (black) spectra for 32°S, 165°E using spectral degrees 30 to 55 and a 30° angular radius of the spherical cap window. The modeled degree range is in red with theoretical correlation in dark blue. The parameter values used to produce each theoretical curve are given on the figure. (a) the minimum RMS case and (b) a case of an ill-fitting spectrum outside of the acceptable criteria range. Theoretical degree correlation is shown in dark blue. Vertical bars are standard error estimates on the spectra. 75

Figure 4.35 RMS space of crustal thickness, elastic thickness, and load density at location 32°S, 165°E for a 30° angular radius of the spherical cap window using spectral degrees 40 to 65. This plot uses a constant crustal density of 2300kgm⁻³, which corresponds to the crustal density leading to the lowest RMS parameter combination (noted by the black circle, corresponding to Figure 4.32a). 76

Figure 4.36 RMS space of crustal thickness, elastic thickness, and load density at location 32°S, 165°E for a 30° angular radius of the spherical cap window using spectral degrees 30 to 55. This plot uses a constant crustal density of 2500kgm⁻³, which corresponds to the crustal density leading to the lowest RMS parameter combination (noted by the black circle, corresponding to Figure 4.33a). 77

Figure 5.1 Contours (white lines) of the mean estimated crustal thickness for the range of possible estimates at each study location and spherical cap windows (gray circles) over MOLA topography. The mean value for each location is noted near an “x” at the center of the spherical cap. Spherical cap windows centered on the boundary are not shown, but their center and associated estimate are marked. The approximate CDB is shown by the red dashed line with InSight landing site marked by a white star. Contours that are greater than 10° away from an estimate are not connected and it is noted that drawing contours with this few points may be misleading. 81

Figure 5.2 Contours (white lines) of the mean estimated crustal density (kgm^{-3}) for the range of possible estimates at each study location and spherical cap windows (gray circles) over MOLA topography. The mean value for each location is noted near an “x” at the center of the spherical cap. Spherical cap windows centered on the boundary are not shown, but their center and associated estimate are marked. The approximate CDB is shown by the red dashed line with InSight landing site marked by a white star. Contours that are greater than 10° away from an estimate are not connected and it is noted that drawing contours with this few points may be misleading. 84

Figure 5.3 Contours (white lines) of the mean estimated elastic thickness for the range of possible estimates at each study location and spherical cap windows (gray circles) over MOLA topography. The mean value for each location is noted near an “x” at the center of the spherical cap. Spherical cap windows centered on the boundary are not shown, but their center and associated estimate are marked. The approximate CDB is shown by the red dashed line with InSight landing site marked by a white star. Contours that are greater than 10° away from an estimate are not connected and it is noted that drawing contours on this few points may be misleading. 87

Figure 5.4 Contours (white lines) of the elastic thickness corresponding to the minimum RMS parameter combination for each study location and spherical cap windows (gray circles) over MOLA topography. The mean value for each location is noted near an “x” at the center of the spherical cap. Spherical cap windows centered on the boundary are not shown, but their center and associated estimate are marked. The approximate CDB is shown by the red dashed line with InSight landing site marked by a white star. Contours that are greater than 10° away from an estimate are not connected and it is noted that drawing contours on this few points may be misleading. 88

CHAPTER 1. INTRODUCTION

1.1 Significance

The Mars crustal dichotomy boundary (CDB) is a planetary scale, relatively sharp topographic transition between the Northern Lowlands and the Southern Highlands. Across the boundary, Mars has contrasting surface expressions, suggesting that crustal evolution was not uniform across the planet (Wieczorek, 2007). This dichotomy boundary is easily observable (Figure 1 – topographic dichotomy), but its cause and evolution are not well understood (Watters et al., 2007). As one of the most distinctive Martian crustal features, the boundary is a key element for better understanding the thermal evolution, mantle convection, magnetic field dynamo, and Tharsis volcanism on Mars (Watters et al., 2007).

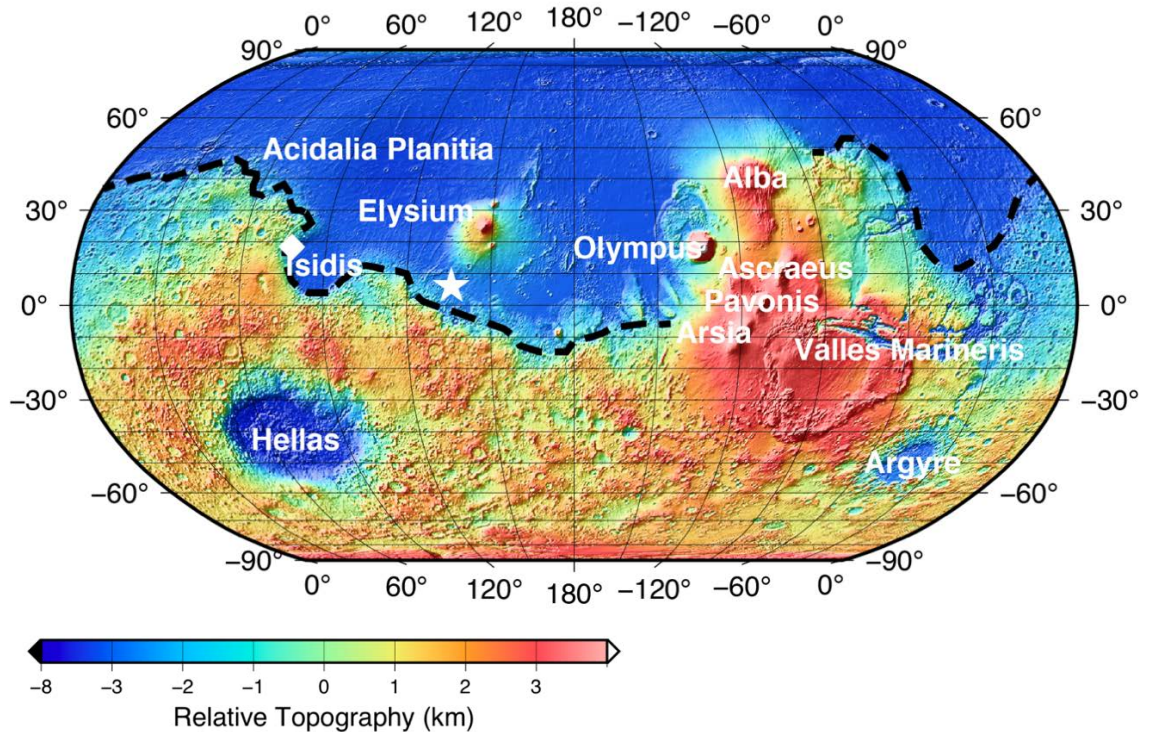


Figure 1.1 Mars surface features with shaded MOLA topography. Low topography is colored in blue and high topography is in red. Approximate outline of crustal dichotomy boundary shown by dashed line. Star shows location of Insight landing site and diamond shows Perseverance.

The goal of this study is to better understand the structure and evolutionary history of the CDB of Mars by using the latest and highest resolution geophysical and geological databases. To understand the formation of the dichotomy and differences in crustal evolution across it, knowledge of topography, gravity, crustal thickness, elastic thickness, ages, rock types and magnetic variations is necessary (Wieczorek, 2007). Elastic thickness is a measure of flexural rigidity which describes how the lithosphere behaves in different loading scenarios (Turcotte and Schubert, 1982) and thus is reflective of lithospheric strength and rheological nature (Thor, 2016). How elastic thickness varies on either side of the CDB will be indicative of the thermal and

rheological conditions during its formation. With the currently limited types of geophysical data coverage on Mars, it is difficult to gain insight into the mechanical nature of the deep lithosphere without understanding the variation of elastic thickness across this boundary (McKenzie et al., 2002). The global gravitational field for Mars has been resolved up to spherical harmonic degree 120 (Genova et al., 2016) and is shown in Figure 1.2 and 1.3.

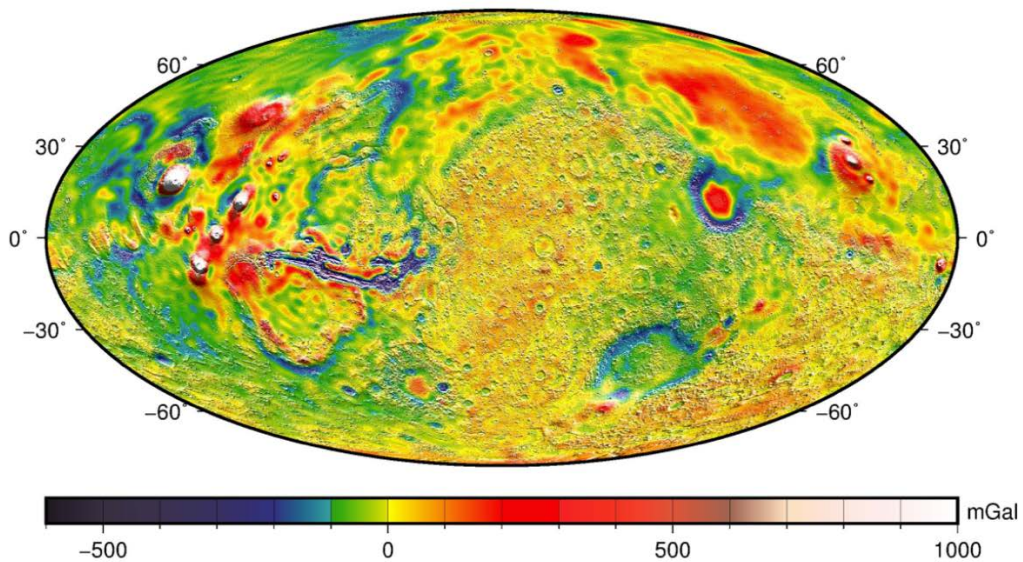


Figure 1.2 GMM-3 free-air gravity anomaly map of Mars from Genova et al. (2016).

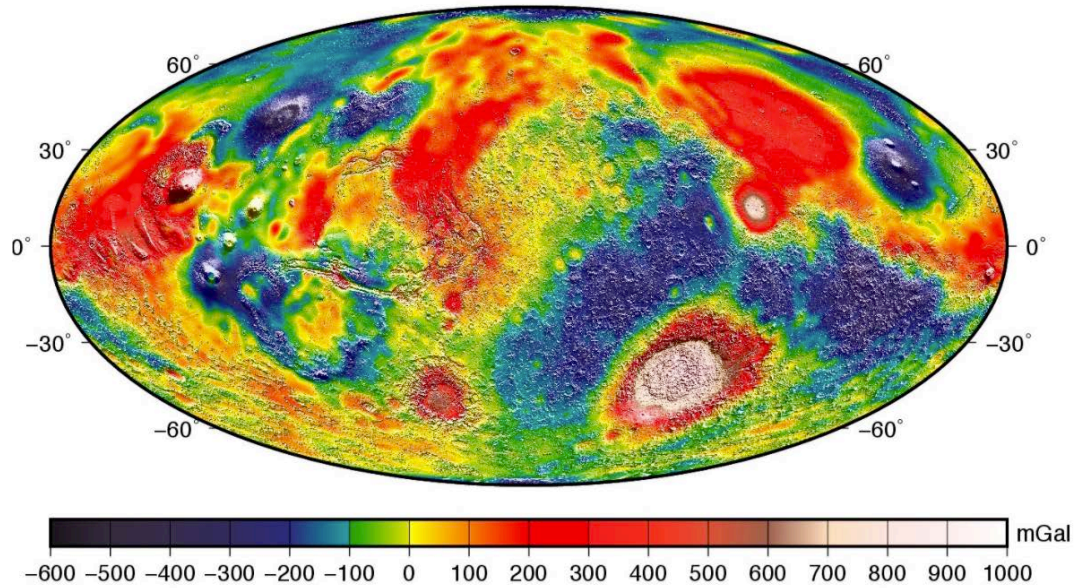


Figure 1.3 Bouguer gravitational anomaly of Mars over shaded relief from Genova et al. (2016).

1.2 Geologic History

Planetary spacecraft missions since the 1990s have delivered a wide range of geologic and geophysical observations that have been used to understand some aspects of the geologic evolution of the planet. These databases provide insight into the geologic history of Mars, but due to the limited nature of observations, knowledge of the formation and evolution of this boundary is still largely unknown.

Mars has experienced three distinct geologic periods, the Noachian, Hesperian and Amazonian (Carr and Head, 2010). Not much is known about the pre-Noachian, which began at the time of the formation of the planet 4.5Gya. Mars likely differentiated into crust, mantle and core within a few tens of millions of years (Carr and Head, 2010). However, there is magnetic anomaly evidence that a planetary magnetic field was active during this time (Solomon et al., 2005). The crustal dichotomy boundary is thought to be one of the oldest crustal features on Mars, and likely formed well before the end of the

pre-Noachian approximately 4.1Gya (further discussed in next section, Carr and Head, 2010).

The Noachian period is marked with the formation of Hellas approximately 4.1Gya and included high rates of cratering, erosion and valley formation (Carr and Head, 2010). Formation of significant geologic features, such as the Tharsis volcanic province, likely began during the Noachian, but there was not wide-spread volcanic resurfacing (Phillips et al., 2001). Magnetic field sources correlating with the ancient cratered terrain of the Martian high-lands was discovered, however, the absence of crustal magnetism near large impact basins such as Hellas and Argyre implies the internal dynamo likely ceased during the early Noachian (Acuña et al., 1999). Evidence from buried impact basins suggests the lowlands are no younger than Early Noachian, and absolute age models constrain the age of buried lowlands to be 4.04-4.11Gya (Frey, 2006). Hydrous weathering products, such as phyllosilicates, indicate that there was at least occasional widespread fluvial activity during warm, wet conditions similar to those resulting from large volcanic events (Carr and Head, 2010). Average erosion rates were high compared with later epochs but began to slow down towards the end of the period. This decrease coincided with dropping rates of impacts, valley formation and weathering, while volcanism continued at a high average rate (Carr and Head, 2010).

The Hesperian began approximately 3.7Gya as erosion, impacts, and valley formation of the Noachian slowed. Continued volcanism is thought to have resurfaced approximately 30% of the surface of the planet (Head et al., 2002). Although impacts continued during the beginning of the Hesperian, they soon decreased to near the low rate that is seen today (Carr and Head, 2010). There is little evidence of hydrous weathering

during this period, but large episodic floods are thought to have occurred. These episodic floods may have left behind large bodies of water that developed large networks of outflow channels (Carr and Head, 2010). Canyon formation greatly increased through the Hesperian, and much of Valles Marineris might have begun opening (Montgomery et al., 2009). Changes at the end of the Noachian likely suppressed most aqueous activity at the surface other than large floods, but water activity perhaps did not end, as evidenced by discrete sulfate rich deposits, sulfate concentration in soils and presence of Hesperian valley networks (Carr and Head, 2010).

Approximately 3.0Gya, the Hesperian transitioned into the Amazonian epoch as geologic activity further slowed. Volcanism decreased gradually to about a factor of ten lower than that of the Hesperian, but there were likely punctuated events confined to Tharsis and Elysium (Carr and Head, 2010). The main era of water flooding was over, although small floods occurred episodically until geologically recent times. Canyon development was restricted to formation of large landslides while erosion and weathering rates were extremely low (Carr and Head, 2010).

1.3 Crustal Dichotomy Boundary

The crustal dichotomy boundary (CDB) creates a bimodal distribution of elevations, with a difference of up to 5.5km between the two hemispheres (Aharonson et al., 2001). The hemispherical elevational transition (Figure 1.1) is generally reflected in other lithospheric properties such as crustal thickness (Genova et al., 2016) and crustal density (Goossens et al., 2017). As one of the oldest geologic surface features of Mars, the boundary is thought to have developed during the pre-Noachian, between crustal

formation 4.5Gya and the oldest of the superimposed impact basins 4.1Gya, such as Utopia and Chryse (Carr and Head, 2010).

Remnants of old craters that poke through the younger plains and vague circular outlines in images suggest that the difference in cratering of the two hemispheres is largely superficial, as there might be a densely cratered surface at depths below the present Hesperian Amazonian surface north of the dichotomy (Nimmo and Tanaka, 2005). The presence of a buried, densely cratered surface would exclude the possibility of CDB being formed from creation of new crust, such as during seafloor spreading (Sleep, 1994).

Another possible explanation is that the boundary could be the result of one or more large impacts (Wilhelms and Squyres, 1984; Andrews-Hanna and Zuber, 2008). However, there is no clear evidence of extreme crustal thinning, as would be expected of an impact of that size, or a perceptible rim around the basin (Carr and Head, 2010). Two main mechanisms have been proposed; early internal origin tied to global mantle convection (Zhong and Zuber, 2001; Andrews-Hanna and Zuber, 2008), and an oblique impact by a body 1600-2700km in diameter (Marinova et al., 2008). Models using buried impact basins suggest that quickly operating mechanisms early in the history of Mars may be more likely than endogenic models (Frey, 2006). None of these formation mechanisms have been confirmed, and thus further research of the boundary is necessary.

1.4 Elastic Thickness

The strength of the lithosphere will determine how much it bends in response to loading (Turcotte and Schubert, 1982), and elastic thickness is a way to measure this

lithospheric strength (Broquet and Wieczorek, 2019). It can be determined using the relationship between gravity anomalies and topography at different harmonics in an inverse modeling approach (Dorman and Lewis, 1970; Turcotte et al., 1981; Forsyth, 1985). It primarily depends on age, temperature, thermal gradient, composition, flexural plate curvature and deviatoric stresses (Tesauro et al., 2012; Thor, 2016).

Alternatively, in a rheological forward modeling approach, the total lithospheric strength is the depth-integrated yield strength of the lithosphere (i.e., the difference between the maximum and minimum of the principal normal stresses or $(\sigma_1 - \sigma_3)$ over the entire thickness of the lithosphere). It has also been estimated as the cumulative strength of the lithosphere layer by layer (see formulas in Burov and Diament, 1995; Tesauro et al., 2012). As a terrestrial planet cools, the lithosphere will strengthen which increases elastic thickness. Therefore, the spatial variability of elastic thickness is a powerful tool in understanding lateral variability in the structure of the lithosphere, its thermal evolution, deformation and regional surface features (Grott and Breuer, 2010).

When there is no strength in the crust (or no elastic thickness), topography and other intracrustal loads will be fully isostatically compensated at the Moho and there will be lithospheric deflection in response (Turcotte and Schubert, 1982). Thus, a surface load associated with zero elastic thickness would produce a small, positive free air gravitational anomaly (Figure 1.4). As elastic thickness and strength of the lithosphere increase, there is a decreasing amount of lithospheric deflection, corresponding with less isostatic compensation. Therefore, increasing elastic thickness generates a narrower and more positive free air gravitational response as shown by the progression of Figure 1.4.

Free Air and Bouguer anomalies in relation to Airy isostasy and elastic thickness on Mars

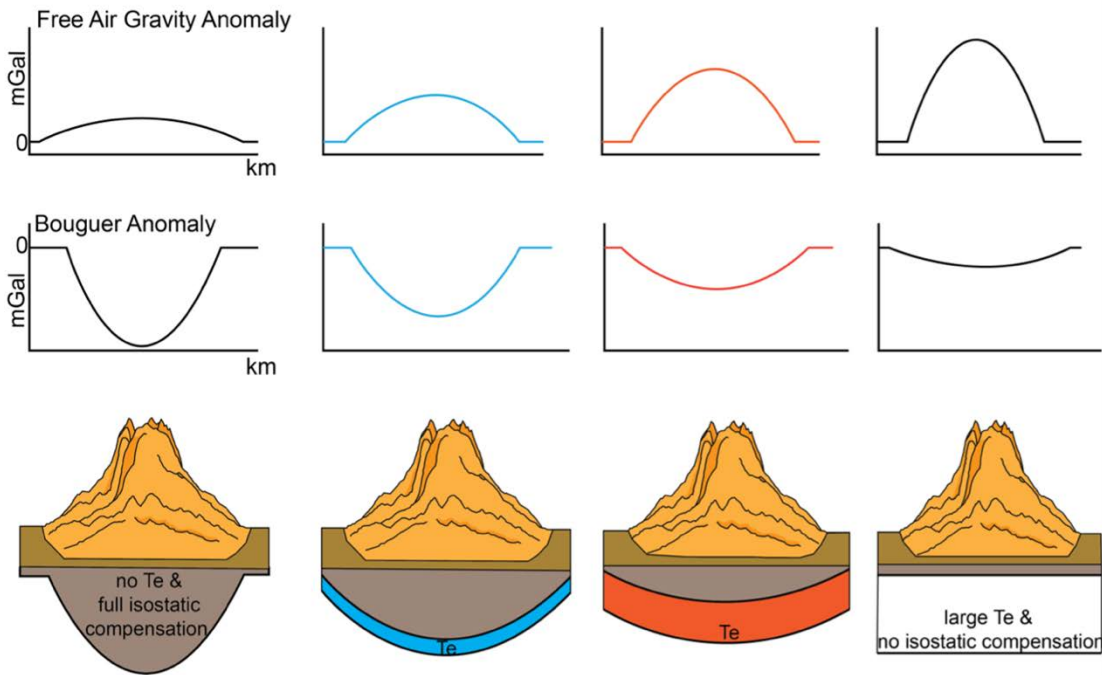


Figure 1.4 Conceptual visualization of elastic thickness (T_e) and its relation to gravity anomalies on Mars. The left endmember represents a case of no elastic thickness, where there is full Airy isostatic compensation. This will create the free air and bouguer anomalies.

While free air anomalies are not corrected for the effects of topography, Bouguer anomalies are (Hinze et al., 2013). The Bouguer correction attempts to remove the gravitational influence of all wavelengths of topographic variation (Hinze et al., 2013). If an area has no elastic thickness, the full isostatic compensation of the load will result in a strongly negative Bouguer anomaly (Hinze et al., 2013). As elastic thickness increases, lithospheric deflection and isostatic compensation decrease. When there is a large elastic thickness, the associated Bouguer anomaly will be small and negative. The progression of the middle row in Figure 1.4 demonstrates this conceptually. Thus, gravity anomalies

are useful for the elastic thickness estimation because of its response to loading scenarios and isostatic compensation.

Several elastic thickness studies have been conducted globally and over localized regions of Mars using a variety of techniques, and this study aims to look specifically at the CDB. Zuber et al. (2000) computed global elastic thickness measurements that distinctively showed lower elastic thickness in the northern hemisphere with much higher elastic thickness in the Southern Highlands. This suggested that the Southern Highlands were much older while the northern hemisphere was a locus of heat flow where the elastic thickness increases with time of loading (Zuber et al., 2000). Localized estimates were found by McGovern et al. (2002) using the spectral admittance method that show a generally decreasing thickness with increasing age of the lithospheric load. Line of sight (LOS) acceleration of spacecraft response to internal masses are related to free-air gravity anomalies, and admittance estimates from LOS gravity and topography, rather than their spherical harmonic coefficients, were used by McKenzie et al. (2002) to estimate the thickness of the elastic lithosphere over several localized regions. The results showed Tharsis having a larger elastic thickness than the poles, Elysium and Valles Marineris. Localized volcanic loads were modeled for elastic thickness by Belleguic et al. (2005), which were all above 50km. In the Northern Lowlands region, Hoogenboom and Smrekar (2006) found low estimates of elastic thickness, ranging from 10-24km, for localized regions of the Northern Lowlands using Cartesian multitaper analysis. Elastic thickness at the northern pole was determined to be 196km by a model produced in Grott and Breuer (2010) for heat flow models. Global admittance estimates are provided by Thor (2016) via multitaper analysis. A globally averaged thickness of

the elastic lithosphere was calculated to be in the range of 90 ± 10 km from spherical harmonic coefficient expansion by Turcotte et al. (2002).

These studies have used a wide range of methods to derive widely varying elastic thickness estimates. Elastic thickness can indicate the formation and cooling scenario, which is especially important for understanding the drastically different surface expressions of the Northern Lowlands and the Southern Highlands.

1.5 Spherical Harmonics

Mars is a small, approximately spheroidal body (in comparison to the Earth) with an average volumetric radius of 3389.5km. In localized admittance analysis for understanding the elastic lithosphere variation on Mars, the curvature of the planet will affect calculations more than on a larger body such as Earth (Broquet and Wiczorek, 2019). Thus, it is advantageous to do calculations for localized regions of Mars in spherical coordinates rather than cartesian. Using spherical coordinates requires that the gravitational field and topography be expanded into their spherical harmonic representations, which is reviewed here through the convention used by Broquet and Wiczorek (2019). Spherical harmonics are the natural set of basis functions to represent and model physical quantities and mathematical functions defined on a sphere. Any function defined on the surface of a sphere can be written as the sum of its orthogonal basis functions. This can be defined as

$$g(\theta, \phi) = \sum_{l=0}^{\infty} \sum_{m=-l}^l g_{lm} Y_{lm}(\theta, \phi) , \quad (1.1)$$

where Y_{lm} is the spherical harmonic function of degree l and order m , g_{lm} is the corresponding spherical harmonic expansion coefficient and θ, ϕ represent the position on a sphere in colatitude and longitude. Thus, any function over the sphere is represented as the sum of its basis functions at a position. For this study, the common geodesy 4π normalization is used over all degrees and orders. When looking at signals in their spherical harmonic representations, each degree will represent different information about the signal. Gravity signals at low degrees will represent parts of the signal that are contributed by masses of large dimensions, such as Olympus Mons and the Tharsis volcanic region. Similarly, the low degrees in topography arise from wide topographic features. Higher spherical harmonic degrees will therefore represent smaller wavelength features of the signal and can potentially be masked by the contribution of longer wavelengths and vice versa depending on their amplitudes. To understand the contribution of signal at each degree and order, a power spectrum can be constructed, which defines how the strength of the function varies with spherical harmonic degree. For a given function g , the total power is given by

$$\frac{1}{4\pi} \int_{\theta, \phi} g^2(\theta, \phi) \sin\theta \, d\theta \, d\phi = \sum_{l=0}^{\infty} S_{gg}(l) \quad , \quad (1.2)$$

where

$$S_{gg}(l) = \sum_{m=-l}^l g_{lm}^2 \quad , \quad (1.3)$$

is the power spectrum. Further, it can be advantageous to see how the power of two signals covaries with degree. To do this, a cross power spectrum of two functions, g and t can be computed

$$\frac{1}{4\pi} \int_{lm} t(\theta, \phi) g(\theta, \phi) \sin\theta d\theta d\phi = \sum_{l=0}^{\infty} S_{tg}(l) \quad , \quad (1.4)$$

Using the cross-power spectrum of gravity and topography, S_{tg} and the power spectrum of topography S_{tt} , admittance can be defined as

$$Z(l) = \frac{S_{tg}(l)}{S_{tt}(l)} \quad . \quad (1.5)$$

Admittance is useful for analyzing how gravity and topography signals are related and is affected by a range of lithospheric properties (such as elastic thickness and crustal density). A widely used spectral method of estimating lithospheric parameters is to calculate observed admittance, then compare it to a theoretical admittance that estimates $Z(l)$ (Eqn. 1.5). It is also useful to know the phase relationship between the signals, which is done through computing correlation as described by

$$\gamma(l) = \frac{S_{tg}(l)}{\sqrt{S_{tt}(l)S_{gg}(l)}} \quad , \quad (1.6)$$

with S_{gg} being the power spectrum of the gravity signal. Correlation is bounded between minus one and plus one, with correlations closer to +1 one representing greater phase similarity. Correlations close to zero would indicate little or no relationship between the signals, whereas correlations close to -1 would indicate a strong inverse dependence. The global admittance and correlation for Mars, using the GMM3 gravity model (discussed in Chapter 2), are shown in Figure 1.5.

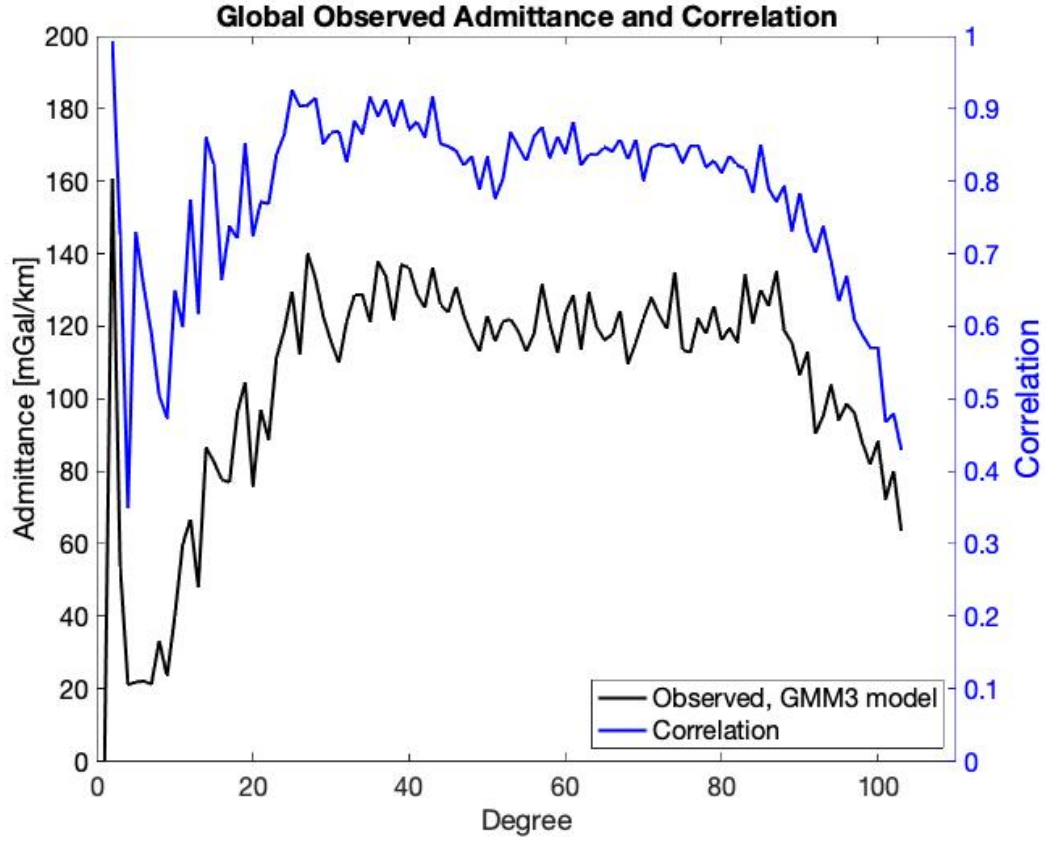


Figure 1.5 Observed global admittance signal (black) and observed global correlation (blue). The gravitational model used is GMM3.

For manipulating the gravity signal, it is convenient to represent it as the gravitational potential (as gravitational acceleration is the gradient of the potential).

Expanding the gravitational potential, U , into spherical harmonics as

$$U(r) = \frac{GM}{r} \sum_{l=0}^{\infty} \sum_{m=-l}^{\infty} \left(\frac{R_0}{r}\right)^l C_{lm} Y_{lm}(\theta, \phi) , \quad (1.7)$$

where G is the gravitational constant, M is the mass of the object and R_0 is the reference radius of the spherical harmonic coefficients. Gravitational acceleration is the gradient of the potential, written as

$$g(r) = \frac{GM}{r^2} \sum_{l=0}^{\infty} \sum_{m=-l}^l \left(\frac{R_0}{r}\right)^l (l+1) C_{lm} Y_{lm}(\theta, \phi) \quad . \quad (1.8)$$

Thus, it is possible to use the spherical harmonic expansion of gravitational potential to arrive at gravitational acceleration for calculating admittance.

The next chapter of this thesis will briefly review the data and programs used. Then, we describe the method of admittance modeling using a mass sheet approximation, our selection criteria, possible sources of noise and the study locations. Modeled admittance spectra and estimated parameter ranges are then presented for each location, followed by a discussion of interpretations and conclusions.

CHAPTER 2. DATA AND SOFTWARE PROGRAMS

2.1 Topography and Gravity Models

This study makes use of the highest available resolution topography and gravity models of Mars. Aboard the Mars Global Surveyor (MGS), the Mars Orbital Laser Altimeter (MOLA) collected topography data using infrared radar pulses from 1997 to 2005. MOLA was the first altimeter sent to Mars and greatly improved the accuracy, precision, and resolution of topography in the vertical and horizontal directions. Data from this mission are freely available on the Planetary Data System (PDS) Geosciences node (<http://pds-geosciences.wustl.edu>). Mark Wieczorek expanded the MOLA topography data up to spherical harmonic degree and order 2600 and processed it into a form convenient for geophysical investigation. We use his model up to degree and order 720 for mapping (Figure 1) and up to degree 120 for admittance calculations (Wieczorek and Meschede, 2018).

Data from MGS, Mars Reconnaissance Orbiter (MRO) and Mars Odyssey were used to update the gravitational field solutions for Mars. I use the GMM3_120 free-air gravitational model (Genova et al., 2016), which has been expanded up to spherical harmonic degree 120 (Nyquist wavelength ~ 180 km). The global free-air and Bouguer gravitational anomalies are shown in Figures 1.2 and 1.3.

2.2 SHTOOLS, GMT and other software

To calculate spherical harmonic expansions, perform analysis and generate maps, a computationally efficient modeling software package Spherical Harmonic Tools (SHTOOLS, Wieczorek and Meschede, 2018) was utilized. A key component in the

calculations needed for the analysis of this study is the ability to expand a data set into spherical harmonics coefficients, localize the signal over spherical caps, and reconstruct spherical harmonic coefficients to the spatial domain. SHTOOLS enables many aspects of this analysis using the standard geodesy 4π normalized spherical harmonic functions. Localization, admittance, correlation and error estimate calculations are done with SHTOOLS functions further discussed in Chapter 3.

In addition to SHTOOLS, modeling code was developed using Matlab and FORTRAN that enable construction of a theoretical admittance signal and testing of combinations of a range of parameters. Calculation of a theoretical global gravitational potential signal and error analysis were programmed in Matlab while FORTRAN was used for SHTOOLS calculations which were strung together and automatized in loops in bash scripts. For site location and mapping of results, Generic Mapping Tools version 6 (Wessel et al., 2019) was used.

CHAPTER 3. METHODS

3.1 Mass-sheet approximation gravitational potential transfer function

The methods of this study use comparisons of observed and theoretical admittance functions to deduce model parameters (e.g., surface density, the thickness of the crust and elastic lithosphere). For creating a theoretical admittance signal, gravity can be expressed as

$$g_{lm} = Q_l t_{lm} \quad , \quad (3.1)$$

with Q_l being the degree-only dependent potential transfer function relating the topography, t_{lm} , to gravity, g_{lm} . By multiplying both sides of equation (1) by t_{lm} and summing over all m , the potential transfer function Q_l can be shown to be equivalent to the admittance signal $Z(l)$ (equation 1.5). Q_l is thus a powerful tool for modeling the effect of lithospheric properties on the admittance signal, as in its schematic representation (Broquet and Wiczorek, 2019):

$$Q_l = Q_l(r_{loc}, T_e, T_c, \rho_l, \rho_c, \rho_m, L, z, E, \nu) \quad , \quad (3.2)$$

where r_{loc} is local planetary radius, T_e is elastic thickness, T_c is crustal thickness, ρ_l is the density of the topographic load, ρ_c is crustal density, ρ_m is the density of the mantle, L is the ratio of surface and subsurface loading, z is the depth of the subsurface load, E is Young's modulus and ν is Poissons ratio. Parameter value ranges investigated in this study and symbols are shown in Table 3.1.

Table 3.1 – Parameters, symbolic representation, value range and units for parameters used in calculation of mass – sheet approximation based theoretical admittance.

Parameter	Symbol	Value	Unit
Mean Planetary Radius	R_{loc}	3389.5	km
Elastic Thickness	T_e	0-80	km
Crustal Thickness	T_c	10-90	km
Load Density	ρ_l	2200-3400	kg/m^3
Crustal Density	ρ_c	2200 -3400	kg/m^3
Mantle Density	ρ_m	3500	kg/m^3
Load Ratio	L	0	-
Depth to Load	z	50	km
Young's Modulus	E	100	GPa
Poisson's Ratio	v	0.25	-

A formulation of the potential transfer function, Q_1 from equation (3.1), is given here from Appendix B of Broquet and Wieczorek (2019). The original forms of these equations are found in Kraus (1967) and Turcotte et al. (1981). This construction of Q_1 relies on the assumption that the gravitational signal can be estimated using a mass – sheet approximation. The mass-sheet approximation calculates the gravitational potential resulting from a spherical wedge of a Bouguer slab located at a defined height (Turcotte and Schubert, 1982). In this study, the spherical wedge of a Bouguer slab is placed on the average planetary radius (Figure A.9). The Bouguer slab approximates gravity without effects from local (short wavelength) topography and represents the effect of loads that are large enough to significantly influence mantle deflection (Figure A.9, Turcotte and Schubert, 1982).

This simplification is necessary to avoid complexities of finite amplitude calculation, which would include the effect of local, short wavelength topography on the potential (Broquet and Wieczorek, 2019). Mass – sheet approximations also require a certain amount of topographical variation in the localized area. If the topography within the localization window is too flat lying, the slab will not be able to accurately approximate the signal. While simplifying calculations, this approach will not produce localized variations in the observed admittance signals; the signals represent gradually increasing and decreasing smooth slopes of admittance (no large dips or bumps) and slope primarily in one direction. In several cases, this is sufficient to make first order parameter determinations from the resulting theoretical admittance signal along the dichotomy boundary while avoiding localized loads (such as volcanoes) which cannot be approximated by mass sheets. A schematic diagram of a windowed mass sheet and accompanying densities and layers is shown in Figure B.1.

The following development is taken primarily from Appendix B of Broquet and Wieczorek (2019). An important parameter in the formulation of Q_l using a mass – sheet approximation is the deflection of the lithosphere due to loading. Flexural rigidity will partially control the response and it is written as (Turcotte and Schubert, 1982; Banks et al., 2000)

$$D = \frac{ET_e^3}{12(1 - \nu^2)} \quad , \quad (3.3)$$

which depends on T_e , as elastic thickness, E as Young's modulus, and ν as Poisson's ratio. Using spherical harmonics to represent the gravitational field and topography, the load and deflection are expanded into spherical harmonic functions, q_{lm} and w_{lm} ,

respectively. Using these representations, one can link the load to the resulting deflection via

$$w_{lm} = \zeta_l q_{lm} \quad , \quad (3.4)$$

where the wavelength dependent parameter ζ_l is composed of the elastic properties of the shell;

$$\zeta_l = -\frac{R_e^4 [l(l+1) - 1 + \nu]}{Dn^3 + 2Dn^2 + ET_e R_e^2 n} \quad . \quad (3.5)$$

Here, $n = l(l+1) - 2$ and R_e is the mid-point of the elastic shell representing the lithosphere, thus $R_e = R - \frac{1}{2}T_e$ with R being the mean radius of the planet.

3.1.1 Surface Loading

There are three different loading scenarios that could occur within this model: surface loading, internal loading, and combination surface and internal loading. For the non-volcano-bearing regions of crustal dichotomy boundary being examined in this study, one could assume that the internal loads are not correlated and thus not important. Assuming all interfaces are deflected by the same amount, one can write the total load acting on the lithosphere (Broquet and Wiczorek, 2019) as

$$q_{lm} = w_{lm}(\Delta\rho_l g_0 + \Delta\rho_c g_m) + \rho_l g_0 h_{lm}^s - \Delta\rho_c U_{lm}(R - T_c) - \rho_c U_{lm}(R) \quad , \quad (3.6)$$

where U_{lm} is gravitational potential, $\Delta\rho_l = \rho_c - \rho_l$, $\Delta\rho_c = \rho_m - \rho_c$, g_0 and g_m are the vertical gravitational acceleration at the surface and at the crust-mantle boundary and h_{lm}^s is the surface topography. Using the mass sheet approximation, the potential at the base of the crust resulting from deflecting each interface is given by

$$U_{lm}(R) = \frac{3g_0}{\bar{\rho}(2l+1)} \left[\rho_l h_{lm}^s + \Delta\rho_l w_{lm} + \Delta\rho_c w_{lm} \left[\frac{R - T_c}{R} \right]^{l+2} \right] \quad , \quad (3.7)$$

and

$$U_{lm}(R - T_c) = \frac{3g_0}{\bar{\rho}(2l + 1)} \left[[\rho_l h_{lm}^s + \Delta\rho_l w_{lm}] w_{lm} \left[\frac{R - T_c}{R} \right]^l + \Delta\rho_c w_{lm} \left[\frac{R - T_c}{R} \right] \right], \quad (3.8)$$

using $4\pi G = \frac{3g_0}{\bar{\rho}R}$. Inserting equation (3.6) into equation (3.7) and then using equation

(3.4), we arrive at

$$w_{lm} = -\frac{\rho_l \bar{C}_l^s}{\Delta\rho_c} h_{lm} \quad , \quad (3.9)$$

where

$$\bar{C}_l^s = \frac{1 - \frac{3}{\rho(2l + 1)} [\rho_c + \Delta\rho_c \left(\frac{R - T_c}{R}\right)^l]}{\frac{g_m}{g_0} + \frac{\Delta\rho_l}{\Delta\rho_c} - \frac{1}{\zeta^l g_0 \Delta\rho_c} - \frac{3}{\rho(2l + 1)} [\Delta\rho_l \left(\frac{R - T_c}{R}\right) + \rho_c \left(\frac{\Delta\rho_l}{\Delta\rho_c} + \left(\frac{R - T_c}{R}\right)^{l+2}\right)]}. \quad (3.10)$$

Using equation (3.10), the spherical harmonic gravitational coefficients at the surface can be written using a linear degree- dependent free air top loading transfer function linking potential to topography

$$U_{lm}^s(R) = Q_l^s h_{lm}^s \quad , \quad (3.11)$$

with the transfer function defined as

$$Q_l^s(R) = \frac{3g_0\rho_l}{\bar{\rho}(2l + 1)} \left[1 - \frac{\Delta\rho_l}{\Delta\rho_c} \bar{C}_l^s - \bar{C}_l^s \left(\frac{R - T_c}{R}\right)^{l+2} \right]. \quad (3.12)$$

The transfer function in Eqn. 3.12 allows us to express the gravitational potential in Eqn. 3.11. To convert this into radial gravity and obtain admittance in mGal/km, we take the radial derivative of the potential (Eqn. 3.11),

$$Z(l) = \left(\frac{l+1}{R}\right) Q_l^s(R) \quad . \quad (3.13)$$

Expressions for internal loads and combined surface and internal loads are given in Broquet and Wieczorek (2019).

3.2 Admittance model

The admittance model used for this study is based on the first order mass-sheet approximation using the potential transfer function described above. Figure 3.1 demonstrates that the transfer function model of admittance (Eqn. 3.13), does substantially depend on elastic thickness (T_e), crustal thickness (T_c), load density (ρ_l), and crustal density (ρ_c). In each panel, only one parameter is varied while the rest remain at a constant value. Elastic and crustal thicknesses are held at a low global estimate of 50km and 57km, respectively. Load density is constant at the average load density of volcanoes, 2900kgm^{-3} and crustal density is held at a high average for volcanic regions, 3300kgm^{-3} . When varied, elastic and crustal thicknesses were increased from a low estimate of 10km to a very high 150km. Load and crustal densities were varied between materials similar to the polar cap (1250kgm^{-3}) and Martian basalt (3300kgm^{-3}).

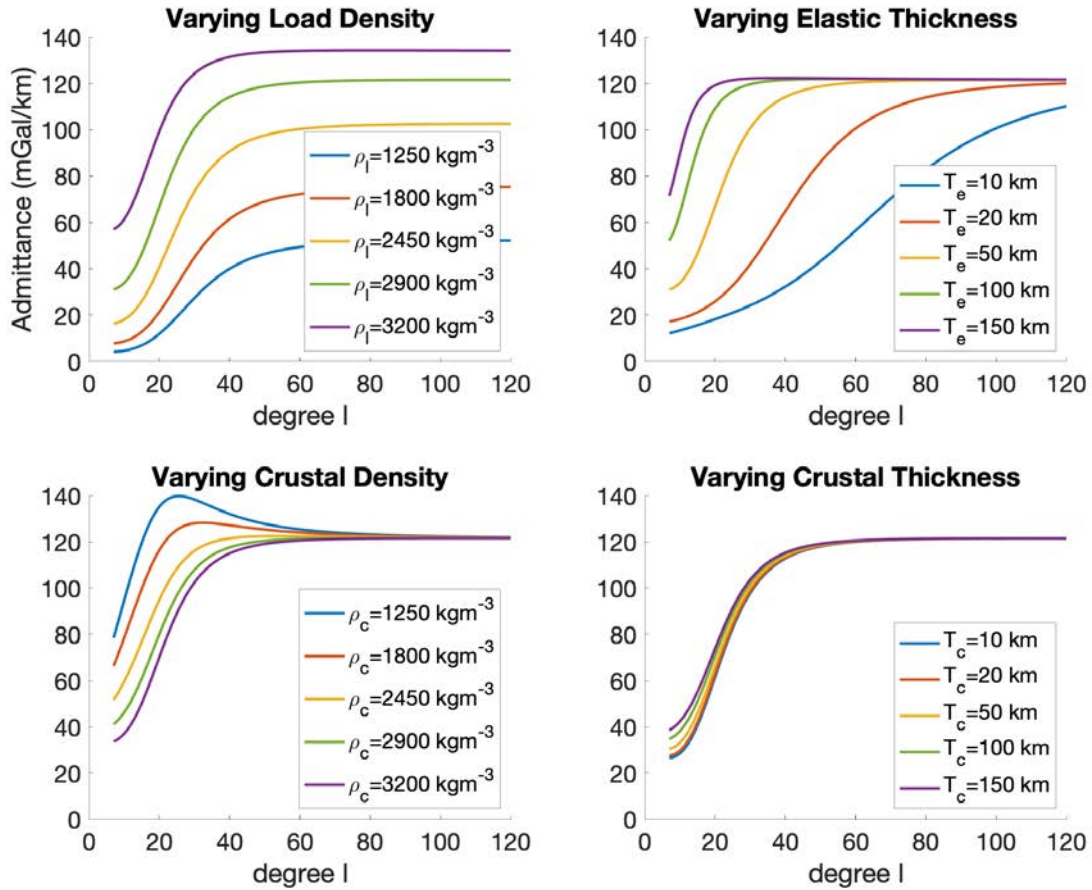


Figure 3.1 Global theoretical admittance model showing the dependency of the model on load density, elastic thickness, crustal density and crustal thickness. In all panels, only one parameter is varied while the rest are held constant at $\rho_l=2900\text{kgm}^{-3}$, $\rho_c=3300 \text{kgm}^{-3}$, $T_e=50\text{km}$, and $T_c=57\text{km}$. The theoretical model has a visible dependency on each of the parameters being tested.

Each parameter has a unique contribution to the overall theoretical signal, and different combinations of parameters are distinguishable from each other. Increasing the load density (upper left pane, Figure 3.1) did not have a major effect on the overall shape of the signal, however, the baselevel significantly increased as load density increased. When crustal density was increased (lower left, Figure 3.1), the signal base level decreased while the shape flattened. Elastic thickness had a major effect on both shape and baselevel, with the signal reaching an asymptotic value in lower degrees as thickness

increased (upper right, Figure 3.1). Crustal thickness had a similar, though much less significant, effect on the asymptotic value (lower right, Figure 3.1).

Figure 3.1 is similar to a revised version of Figure 3 from Broquet and Wiczorek (2019). Both are theoretical models of global (120 degree) admittance using GMM3 gravity model and the Q_1 potential function. Crustal density is shown to be laterally varying over Mars (Goossens et al., 2017), particularly between the low and highland sides of the dichotomy boundary. Varying this parameter allowed us to account for the non-uniform density of the crust along the CDB. Crustal thickness is also transitional on opposing sides of the boundary (Wiczorek and Zuber, 2004; Genova et al., 2016), with generally low crustal thickness (less than ~ 50 km) in the Northern Lowlands and higher (greater than ~ 50 km) in the Southern Highlands. There are regions of anomalous density and / or thickness, however, global estimations show clear distribution differences between opposing sides of the CDB (Genova et al., 2016).

Global observed admittance is shown in Figure 1.5 using the GMM3 gravitational model. Admittance and correlation were calculated via the global SHTOOLS admittance and correlation programs. On a global scale, Figure 1.5 shows low and wildly varying correlations in low degrees, 0-20, and again in high degrees, above 80. This is also generally true for localized observed spectra; low and high degrees have low correlations making interpretations of these portions of the spectra less reliable. It is of note that the first order approximation given by the mass-sheet gravitational potential will not be able to create the saw-toothing of the observed signals, this would require finite amplitude calculations as used by Broquet and Wiczorek (2019).

3.3 Localization and study locations

The global admittance signal in Figure 1.5 needs to be localized in order to model regions that are along the CDB. Localization is accomplished generally through multiplying a windowing function against the data and expanding the result in to spherical harmonics (Wieczorek and Simons, 2005; Wieczorek, 2007). This is written as

$$G(\theta, \phi) = g(\theta, \phi)h(\theta, \phi) \quad , \quad (3.14)$$

where g is the global function, h is the localization window and G is the resulting localized function. The use of spherical harmonics necessitates windows that are spherical caps (Wieczorek and Simons, 2005) of a defined angular radius, rather than cartesian rectangles, as in Nimmo (2002). After the spherical cap is constructed, it is rotated to the region of interest and multiplied against the global signal (Wieczorek and Simons, 2005) producing a circular localized region.

During multiplication of the global and windowing functions, if the window function is not constructed properly, smoothing in the spectral domain can occur (Broquet and Wieczorek, 2019). Smoothing can be countered by ensuring that the window's spectral bandwidth, L_w is minimized (Broquet and Wieczorek, 2019). Additionally, the windowing function should minimize the influence of signals coming from outside of the target region. Here, we ensure that the signal is properly located within the region of interest by adjusting the spectral bandwidth to concentrate 99% of the power within the spherical cap. Thus, a minimal part of the signal is from outside of the area of interest (Broquet and Wieczorek, 2019). The SHTOOLS package is used to construct windowing functions, rotate them to the location of interest and perform the localization.

Effects of localization on the spectra must be taken into consideration before making interpretations. In the wavelength range $l < L_w$, the windowed spectral estimates are heavily biased by wavelengths that are greater than the window size and the spectrum cannot be interpreted for $l > L_{\text{data}} - L_w$ where L_{data} is the maximum spectral resolution of the data (120). At these degrees, the localized spectrum depends upon degrees that have a higher resolution than the input field (Broquet and Wieczorek, 2019).

To avoid undesirable spectral effects, we will only analyze localized spectra between the limits L_w and $L_{\text{data}} - L_w$ (Broquet and Wieczorek, 2019). The portion of the spectra that is useful for interpretation will vary by window location. In some spectra, the correlation might be too low to validate interpretations of parameters from certain degree bands. Additionally, due to the inability of this model to capture saw tothing features, some sections of the spectra might be too irregular to properly model. This limitation, combined with our use of RMS selection criteria (discussed below), creates an unavoidable element of non-uniqueness between solutions that, for some section for the spectra, is unacceptably large and thus uninterpretable. We aim to use the widest range of spectra for each location while accounting for the spectral bandwidth of the function, $L_{\text{data}} - L_w$ and features that are difficult to reconstruct. The useable section of each spectrum for each window location is described in Table 4.1 and 4.2. In order to model the dichotomy boundary while maintaining reasonable resolution, all spherical cap windows have an angular radius of 15° . Every angular degree on Mars corresponds to 60km of physical distance, giving our windows an 1,800 km diameter. The GMM3 degree 90 model has spatial resolution of 4° , corresponding to 240km. Thus, our windows must be larger than 240km in order to have sufficient meaningful signal inside of the

localized area. An angular radius of 15° corresponds with a spectral bandwidth of $L_w = 17$ for all locations in this study (Broquet and Wieczorek, 2019).

To capture differences in elastic thickness across the CDB, we study 12 main locations; 6 within the Northern Lowlands and 6 within the Southern Highlands. They are located between 60°E to 190°E and 45°S to 30°N and are close to the zone of transition (Figure 3.2). This region was chosen for its easily observable topographic distinction along the boundary (Figure 3.2) and its relatively great distance from any large volcanic provinces that would greatly affect the localized spectra. Each location (excluding those along 165°E and 200°E) has a counterpart on the same line of longitude but opposing side of the CDB. This allows comparisons of the modeled elastic thickness along both sides of the boundary. Three special cases with centers located directly on the dichotomy boundary (Figure 4.25) and an example of a larger window are also included.

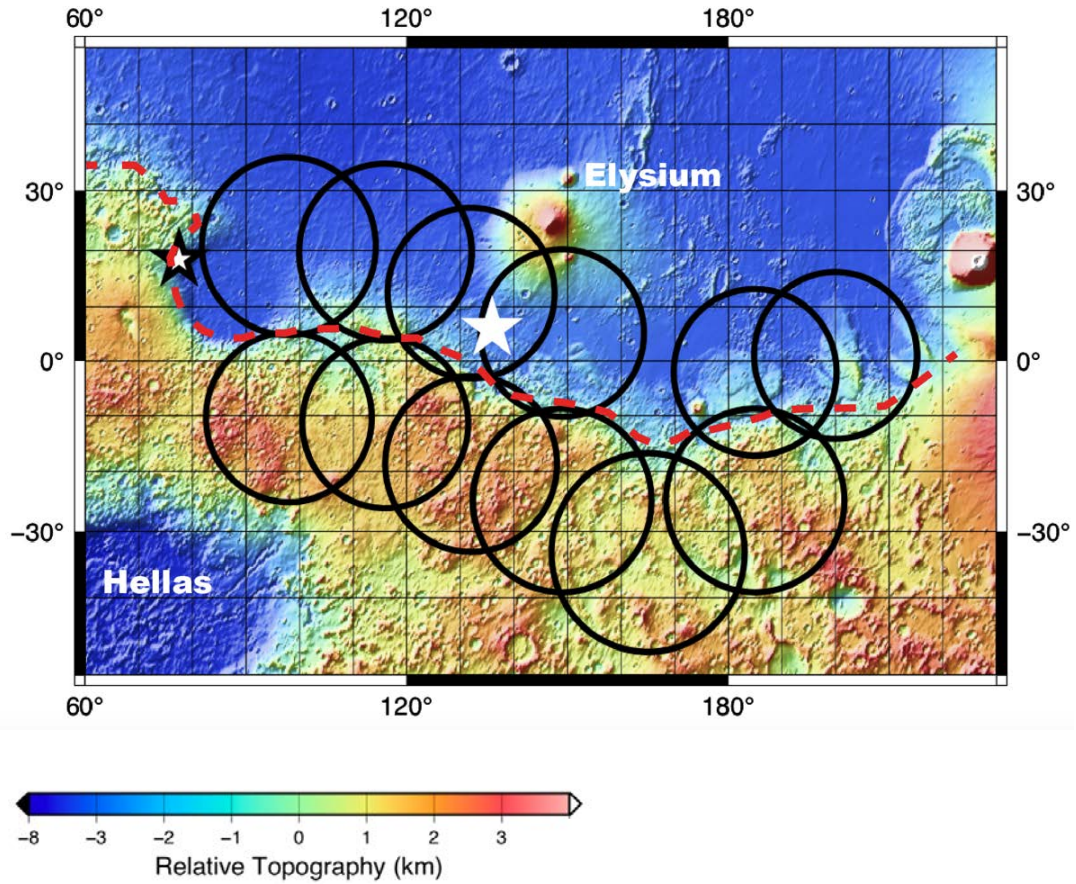


Figure 3.2 Main study locations shown on MOLA topography and intensity. Crustal dichotomy boundary is approximated by red dashed line with Elysium and Hellas locations noted. Insight and Perseverance landing sites are shown by white star and black outline star.

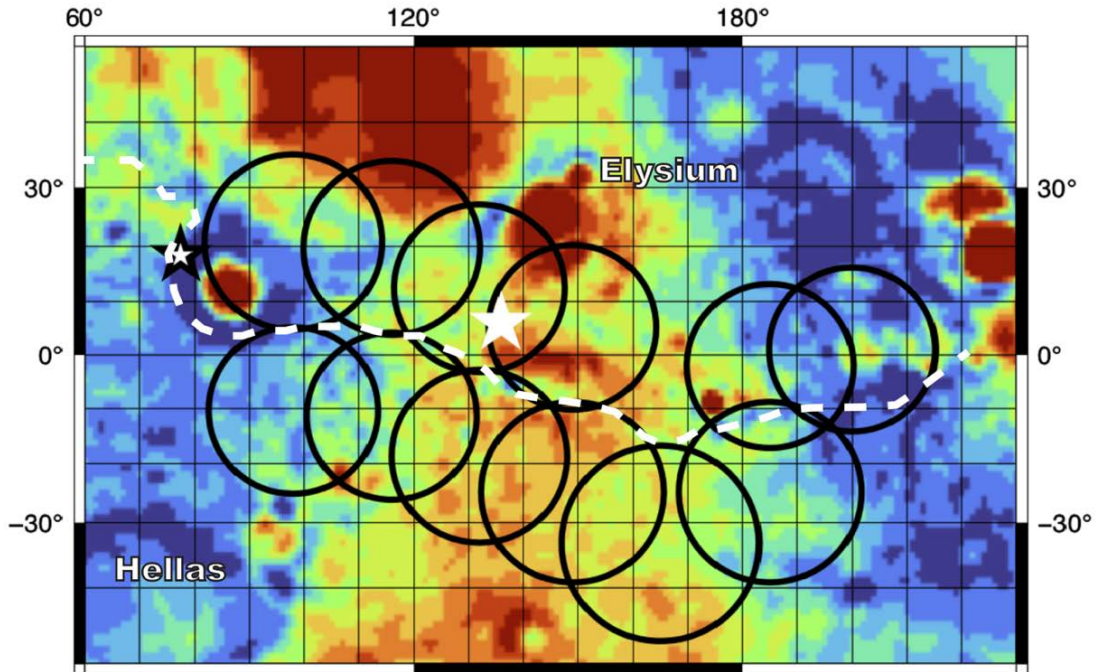


Figure 3.3 Main study locations shown on GMM3 free-air gravitational anomaly. Crustal dichotomy boundary is approximated by white dashed line with Elysium and Hellas locations noted. Insight and Perseverance landing sites are shown by white star and black outline star. Cool colors refer to larger, negative free-air gravitational anomaly while hotter colors refer to large positive anomalies.

3.4 Selection Criteria

To determine how well each combination of parameters models the observed admittance signal, the root mean squared (RMS) error is calculated. RMS calculates the difference between the modeled and observed spectra for each degree and takes the mean squared of all degrees. RMS is formulated as a variant of the method used by McGovern et al. (2002) and Hoogenboom and Smrekar (2006) described by Broquet and Wicczorek (2019)

$$rms(T_e, \rho_l, L) = \sqrt{\frac{1}{N} \sum_{l=l_{min}}^{l_{max}} [Z(l) - Z^{th}(l, T_e, \rho_l, L)]^2} \quad , \quad (3.15)$$

where N is the number of degrees in the spectral range, Z is the observed admittance and Z^{th} is the theoretical admittance. From this formulation, the RMS will depend on elastic thickness, density of the load and the load ratio. Since our model varies additional parameters, the calculation will include dependency on density of the crust and crustal thickness. We do not vary the load ratio, so it is not used in the calculation. Thus, the RMS from equation (3.15) becomes

$$rms(T_e, \rho_l, T_c, \rho_c) = \sqrt{\frac{1}{N} \sum_{l=l_{min}}^{l_{max}} [Z(l) - Z^{th}(l, T_e, \rho_l, T_c, \rho_c)]^2} \quad . \quad (3.16)$$

RMS by definition is non-unique, which arises from averaging along the spectral range; separate parameter combinations could produce similar rms values, but fits with different behavior. To account for non-uniqueness, we generate a space of acceptable solutions which allows for parameter combinations that generate different, but equally well-fitting, models (see Appendix for examples). The value that defines low or high RMS is relative to the location; some locations with highly irregular or sawtooth spectra will naturally be more difficult to model, and thus have an overall higher RMS. At all locations we are able to distinguish between grossly incorrect parameters due to a large difference between the highest and lowest RMS (for instance, location 18°S, 132°E had a lowest RMS of 2.5 and a largest RMS of 186.78) with a significant visual discrepancy (i.e. sloping in opposite directions or rarely matching the observed spectra).

Starting with relatively low RMS values, the fit of the spectra is inspected and accepted until there reaches a point where the solutions deviate from the observed admittance beyond their error bars. Not all parameter combinations within the solution space are equally representative of the signal, thus we use a pseudo 4D map of the RMS (such as Figure 4.2). This approach is advantageous because we are able to account for the non-uniqueness of both the first order mass sheet approximation and the RMS selection criteria.

3.5 Error and Noise

All geophysical observations will have some amount of noise present in the observed signal affecting the resolution of the data. In the gravity field model, the resolvable degree is determined to be where the amplitude of the noise is equal to the strength of the signal (Hoogenboom and Smrekar, 2006). Although there is an inevitable amount of noise in the topography field, it is significantly more accurate than the current gravitational field models. Noise in the gravitational and topography observations will carry over to create uncertainty in the observed admittance calculation, particularly in locations where there is low topographic variation and hence low power in the topography spectrum (Hoogenboom and Smrekar, 2006). Additionally, locations where there is low topography, but a large free air anomaly, have very low correlation, hence making it difficult to estimate elastic thickness (Hoogenboom and Smrekar, 2006).

For every spectral degree (when more than one taper is used), SHTOOLS calculates the standard error of the theoretical signal (Wieczorek and Meschede, 2018). Standard error is defined as

$$SE = \frac{\sigma}{\sqrt{N}} , \quad (3.17)$$

where σ is the standard deviation of that degree and N is the total number of tapers used. The standard error of the observed and theoretical admittance is plotted on the admittance plots for each model (Chapter 4). Tapering, or multiplying the windowing function with the data field in the spatial domain (Thor, 2016), is necessary to create small regions of study for elastic thickness modeling. The number of tapers, or windows, used will affect the localized admittance spectra and its associated error (Wieczorek and Simons, 2005). Calculating standard error of the spectra (eqn. 3.17) requires more than one taper, thus in this study two tapers are used (determined through experimentation and discussion with the authors of Broquet and Wieczorek, 2019) for the observed and calculated admittance spectra. Additionally, increasing tapers will increase the spectral bandwidth, L_w , and thus fewer spectral degrees will be meaningful for modeling. Finally, using a larger number of tapers will smooth the observed and theoretical signals, making them less representative of the original signal. Through experimentation, two tapers were determined to not over smooth the signals and maintain a reasonable number of meaningful degrees.

CHAPTER 4. RESULTS

Acceptable parameter spaces of elastic thickness, crustal thickness, load density and crustal density were determined using the RMS of the difference between the observed and modeled spectra in the selected degree ranges (as discussed in the previous chapter and in Broquet and Wieczorek, 2019). In addition, it was made sure that the fits were not discordant for any of the low RMS yielding spectra.

4.1 Admittance modeling in the Southern Highlands south of the CDB

Modeled admittance spectra in the highlands south of the CDB are plotted in Figures 4.1- 4.11. A slice of the pseudo 4-D RMS plot for each location is taken at the parameter combination with the minimum RMS (corresponding to the minimum RMS shown in Figure 4.1a-4.11a). Constant mantle density of 3500kgm^{-3} , angular radius of the spherical cap window of 15° and the corresponding spectral bandwidth of the window (L_w) of 17 (to maintain high power in the center of the localized window) are used throughout (see Wieczorek and Simons, 2005; Broquet and Wieczorek, 2019).

In order to identify theoretical spectra that have a good visual fit to the observed admittance curve, two criteria are used: first, the mass sheet approximate on is more consistent with lower degrees (\sim degree 30 or 720km wavelength) than high degrees, and hence matching at low degrees should be considered, and, second, the acceptable theoretical admittance curves should be in the range of the observed admittance curve (considering errors in both curves) for degrees approximately from 20 to 100. The selected optimum L_w already limits the lowest degrees that can be used. At low degrees,

correlation between theoretical gravity and topography is also generally low (see Figures 1.1 and 1.2). To not have too great a phase difference between gravity and topography, the observed correlation for the degree range being fit should not be less than 0.9 when possible (a correlation of 0.9 corresponds to $\sim 30^\circ$ of phase difference between the signals, which may be large for this application). Additionally, theoretical correlations above 0.9 are preferred for the modeled degree range. Towards the edges of the localized window, the data weights become progressively lower (zeroing out beyond the spherical cap). Thus, the usable degree range is further limited. We aim to find parameter combinations leading to admittance curves that remain within the middle of the observed curve (i.e., are not beyond the observed error bounds) between degrees 30 to 50. For some observed spectra (such as the one at location 11°S, 116°E, Figure 4.3), however, if one attempted to fit only these low degrees well, parts of the theoretical admittance curve would be beyond the range of the observed admittance. This is also not reasonable as local topographic and gravity features are also meaningful and their admittance should not be much beyond the observed admittance range. For these instances and where no reasonable fits were possible in the degree 30 – 50 range, we use the fit of degrees within 50 to 75 (the range derived empirically) to evaluate the parameter space. Finally, for the evaluation of the fit of the theoretical admittance curves, the readers are reminded that the mass-sheet approximation will not be able to reproduce ups and downs of the observed admittance curves.

Location 10°S, 98°E, on the westernmost edge of the highlands study region (Figure 3.2) has a minimum RMS of 2.8mGal/km between observed and theoretical admittance curves for degrees 48 to 71 for all the ranges of parameters investigated

(Figure 4.1a). Outside of this degree range (0 – 47 and 72 – 100), none of the parameter combinations are able to generate a theoretical spectrum that fits the observed changes in slope (such as between degrees 35 and 50) or large inflections (degrees 80 – 100). Further, the theoretical spectra beyond the acceptable degree range cannot match the observed spectrum and remain completely within the observed error range from degrees 20 to 100 due to the non-reproducible, large inflections (Figure 4.1).

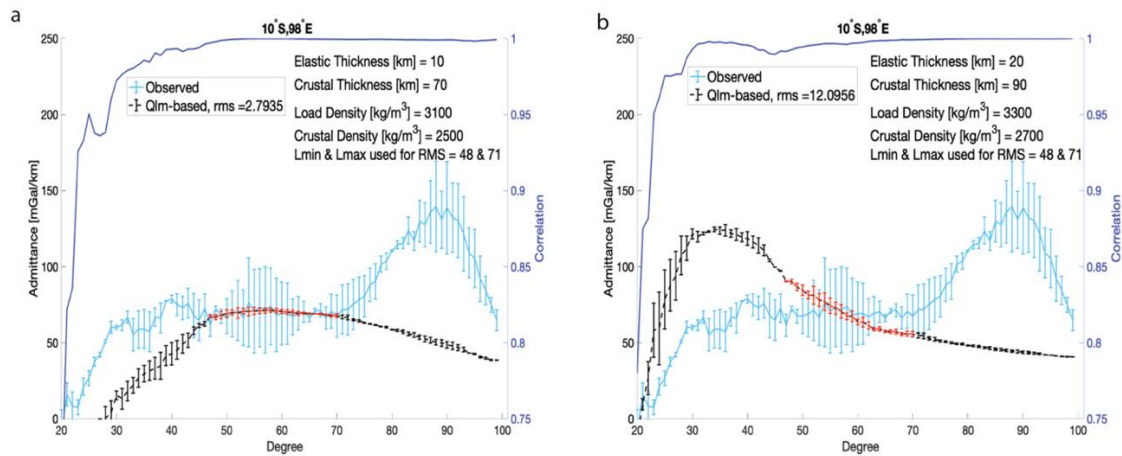


Figure 4.1 Observed (light blue) and theoretical (black) admittance for the 15° spherical cap windowed region centered at 10°S, 98°E. Overlapping parts of observed and theoretical admittances are shown in red on the theoretical spectrum. (a) the minimum RMS case and (b) a case of an ill-fitting spectrum outside of the acceptable criteria range. Elastic thickness, crustal thickness, load density, crustal density and the spectral range used for each theoretical curve are noted. Theoretical degree correlation is shown in dark blue. Vertical bars are standard error estimates on the spectra.

In general, there is a substantial difference between the overall minimum and maximum RMS values, and RMSs can be used to infer grossly incorrect parameter combinations. Distinctly incorrect parameter combinations will not meet the selection criteria and could have a completely opposite slope of the general observed trend (see Figure 4.1b). Here, observed and theoretical admittances from parameter combinations producing RMS greater than 12mGal/km are ill-fitting (i.e. outside of the error bars of

observed and theoretical, an example of such is in Figure 4.1b). Thus, with a maximum RMS of 113.72mGal/km for this case, 89.4% of the RMS space can be excluded from the acceptable solution space.

A general procedure adopted for systematically identifying the feasible parameter space is as follows. The numerically acceptable RMS space (e.g., 10% of the RMSs in the previous example) is further visually screened for the primary acceptance criteria described earlier. The combinations producing acceptable fit within error bars of observed and theoretical admittance are then further evaluated for realistic values. For instance, it would be unlikely for a low lying, topographically flat region (such as in the lowlands) to have a large crustal thickness like 90-100km based on the current models of Mars crustal thickness (Neumann et al., 2004; Goossens et al., 2017). It would also not be likely, for example, for an equatorial region on Mars to have a crustal density similar to that of materials at the polar cap (1250kgm^{-3}) or for a thick highlands crust to have an extremely small density (e.g., Goossens et al., 2017). Moreover, using the current crustal thickness models with constant and variable density crust (Goossens et al., 2017), one can additionally constrain crustal thickness and crustal density. For example, if the crustal thickness in both currently accepted models is greater than 50km, then one can exclude “acceptable” parameter combinations of less than 50km, and vice versa. Based on the results of Goossens et al. (2017), the bulk crustal density in a localized region cannot be effectively further constrained as it ranges from approximately 1800 to 3200kgm^{-3} . However, this overall approach of selecting ranges of parameter space based on global models of crustal thickness significantly helps constrain the remaining parameter ranges for possible load density and elastic thickness estimated from the resulting well-fitting,

constrained parameter combinations. This is additionally necessary because the theoretical mass sheet-based admittance model does not well constrain crustal thickness (Figure 3.1), thus external information is needed. The crustal thickness estimates of Goossens et al. (2017) and Genova et al. (2016) are based on different crustal density assumptions and so cover a large range of possible crustal thicknesses. Thus, although the results are constrained using external information, they still cover a breadth of realistic possibilities. Further, we estimate ranges of possible parameter values to account for non-uniqueness of RMS and fit within the observed and theoretical error selection criteria as many different parameter combinations with an RMS near the minimum RMS might produce good fits within error bars of observed and theoretical (see Figure A.1-A.3 for examples of this for 10°S, 98°E).

Using the above methodology, the region centered over 10°S, 98°E is estimated to have a crustal thickness of 50 – 70km (from models in Goossens et al., (2017), for the region, which yields feasible crustal density between 2200 – 2500kgm⁻³, a load density from 2900 – 3100kgm⁻³, and an elastic thickness of 10-30km.

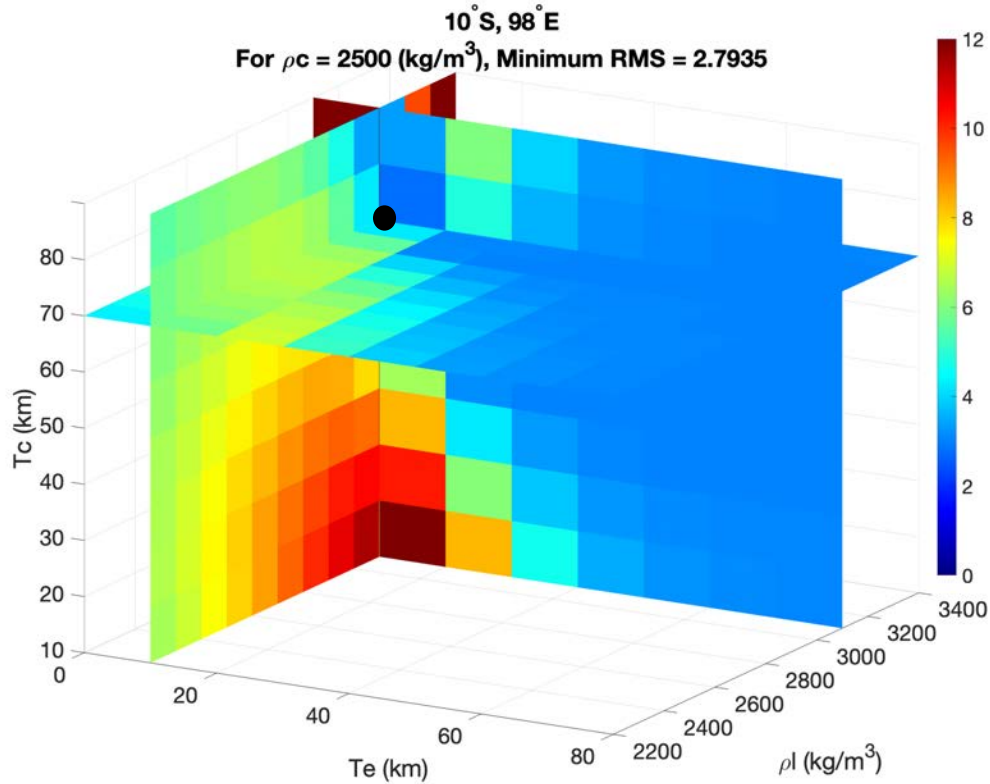


Figure 4.2 RMS of the parameter space of crustal thickness, elastic thickness, and load density at location 10°S, 98°E. This plot uses a constant crustal density of 2500kgm^{-3} , which corresponds to the crustal density yielding the lowest RMS parameter combination (noted by the black circle, corresponding to Figure 4.1a).

The next southern highland study location is on the western side of the CDB area being studied, centered at 11°S, 116°E. Figure 3.2 shows that this region is near a more diffuse transition zone of the boundary; the topography south of 0°S, near 116°E gradually increases southward, rather than the sharp difference near 0°S, 132°E. The observed admittance curve for this region (Figure 4.3) has a significant inflection and changing slope from degrees 30 – 50 that cannot be reproduced using the mass-sheet approximation. For degrees 50 – 75, the observed spectrum has a single upward trend that can be approximated.

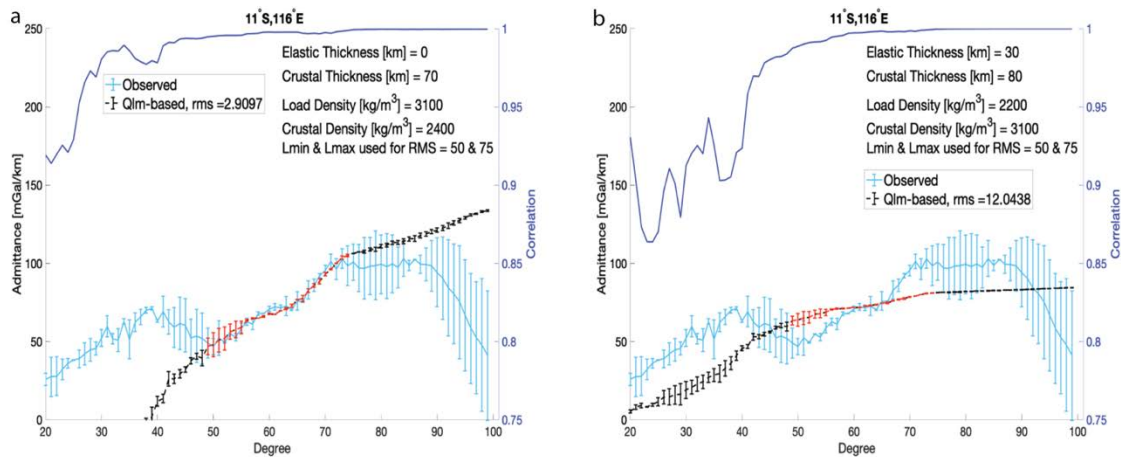


Figure 4.3 Observed (light blue) and theoretical (black) admittance for the 15° spherical cap windowed region centered at 11°S, 116°E. Overlapping parts of observed and theoretical admittances are shown in red on the theoretical spectrum. (a) the minimum RMS case and (b) a case of an ill-fitting spectrum outside of the acceptable criteria range. Elastic thickness, crustal thickness, load density, crustal density and the spectral range used for each theoretical curve are noted. Theoretical degree correlation is shown in dark blue. Vertical bars are error estimates on the spectra.

Using degrees 50-75, the maximum RMS between theoretical and observed admittance is 122.1mGal/km. The minimal RMS of 2.91mGal/km is shown in Figure 4.3a and is able to meet the criteria by fitting well within the error of the observed curve for degrees 50 - 75. Examples of spectra from unique perimeter combinations that produce RMS near the minimum RMS with fit within error bars of observed and theoretical are shown in Figure A.4 and A.5. Spectra with RMS beyond 11mGal/km, such as on Figure 4.3b, begin to exhibit a visually different slope than the observed for the degree range of interest (for example, on Figure 4.3b, modeled degrees have a less steep slope that does not match that of the observed) and thus are excluded from the feasible solution space. Although it appears that the observed and theoretical admittance curves in the degree 20-40 range may fit better as they have similar slopes (Figure 4.3b), the rest of that theoretical curve would exceed the range of the observed admittances

beyond degree 40. Moreover, the degree correlation reduces drastically below degree 40 and becomes wavy and hence such curves were not used.

A cutoff of 11 mGal/km results in ~9% of the RMS space consisting of fits within error bars of observed and theoretical and numerically acceptable solutions. The parameter space was further examined with the constant and variable density-based crustal thickness estimates in Goossens et al., (2017) as described in the general selection procedure earlier. After appropriately constraining the crustal thickness and crustal density, the solution space consists of crustal thickness of 40 – 80 km, crustal density of 2200 – 2400 kgm⁻³, load density of 2900 – 3100 kgm⁻³ and elastic thickness of 0 – 10 km.

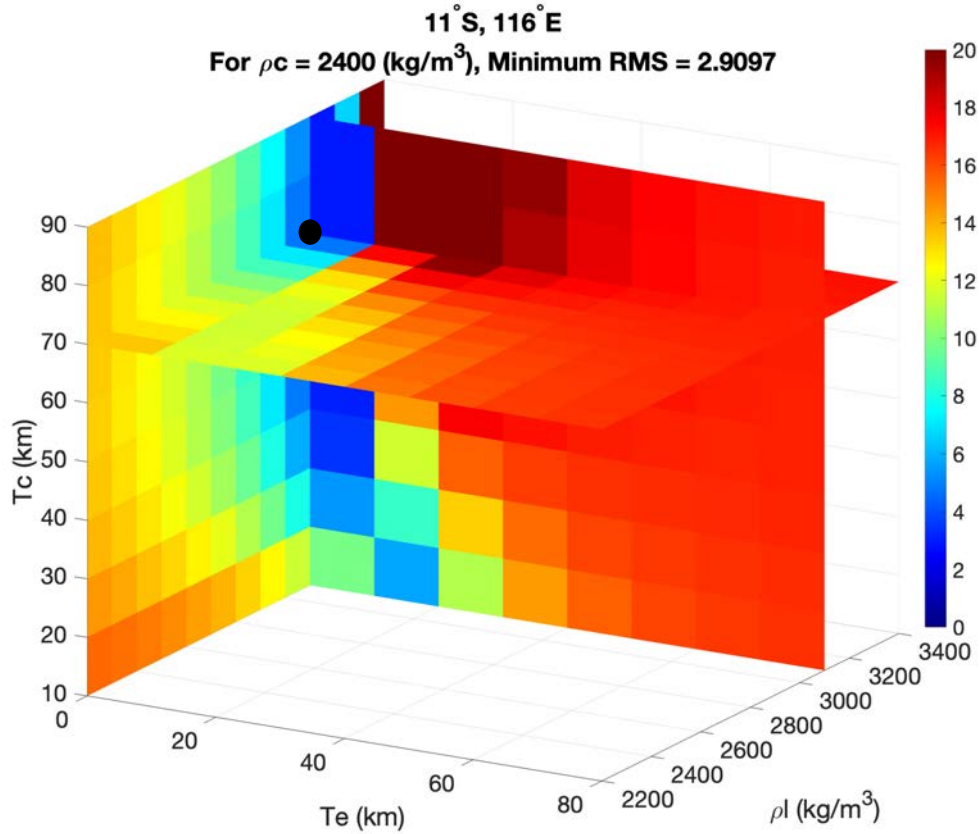


Figure 4.4 RMS of the parameter space of crustal thickness, elastic thickness, and load density at location 11°S, 116°E. This plot uses a constant crustal density of 2400 kg/m^3 , which corresponds to the crustal density yielding the lowest RMS parameter combination (noted by the black circle, corresponding to Figure 4.3a).

The windowed area over 18°S, 132°E is near the middle of the CDB region being studied and has cratering along with high elevation topographic features (Figure 3.2). The mass sheet approximation could reasonably estimate many parts of the observed spectra (Figure 4.5) and thus we are able to consider the lower degree range of 30 – 50 within observed error.

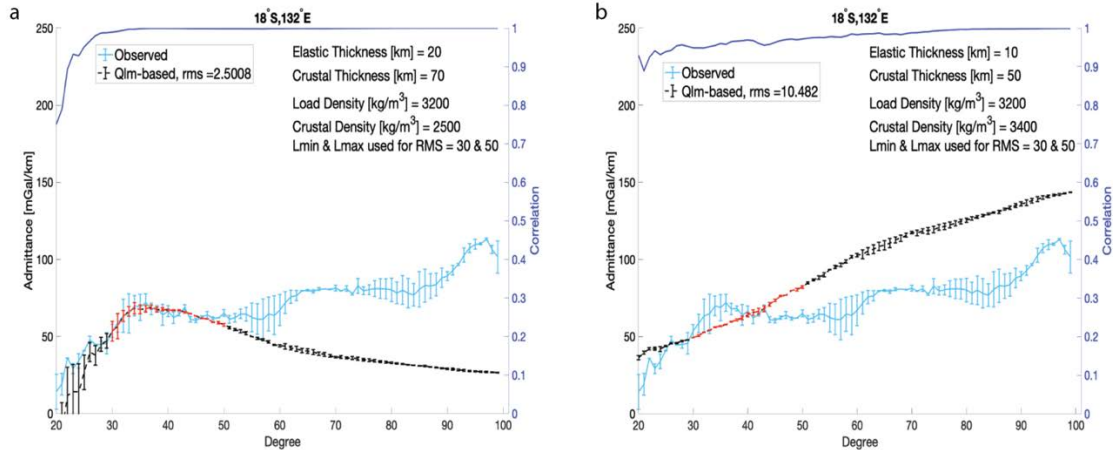


Figure 4.5 Observed (light blue) and theoretical (black) admittance for the 15° spherical cap windowed region centered at 18°S, 132°E. Overlapping parts of observed and theoretical admittances are shown in red on the theoretical spectrum. (a) the minimum RMS case and (b) a case of an ill-fitting spectrum outside of the acceptable criteria range. Elastic thickness, crustal thickness, load density, crustal density and the spectral range used for each theoretical curve are noted. Theoretical degree correlation is shown in dark blue. Vertical bars are error estimates on the spectra.

The minimum RMS, shown in Figure 4.5a, is 2.5mGal/km. Parameter combinations that produce theoretical curves fitting a majority of the degree range and matching the general slope are present until an RMS of 10mGal/km. After an RMS of 10mGal/km, parameter combinations often have an incorrect slope (Figure 4.5b) or a curve that is outside of the observed error for most of the degree range. With the maximum RMS of 186.78mGal/km, ~95% of the total RMS space can be excluded (using RMS and within error bars of observed and theoretical admittance). Acceptable parameters (using RMS and within error bars of observed and theoretical admittance) were further constrained via the crustal thickness and density estimates of models presented in Goossens et al. (2017). The parameter ranges are estimated to be a crustal thickness between 50-70km (40-70km in Goossens et al., 2017), crustal density of 2200-2500kgm⁻³, load density of 2300-3200kgm⁻³ and elastic thickness of 20-50km.

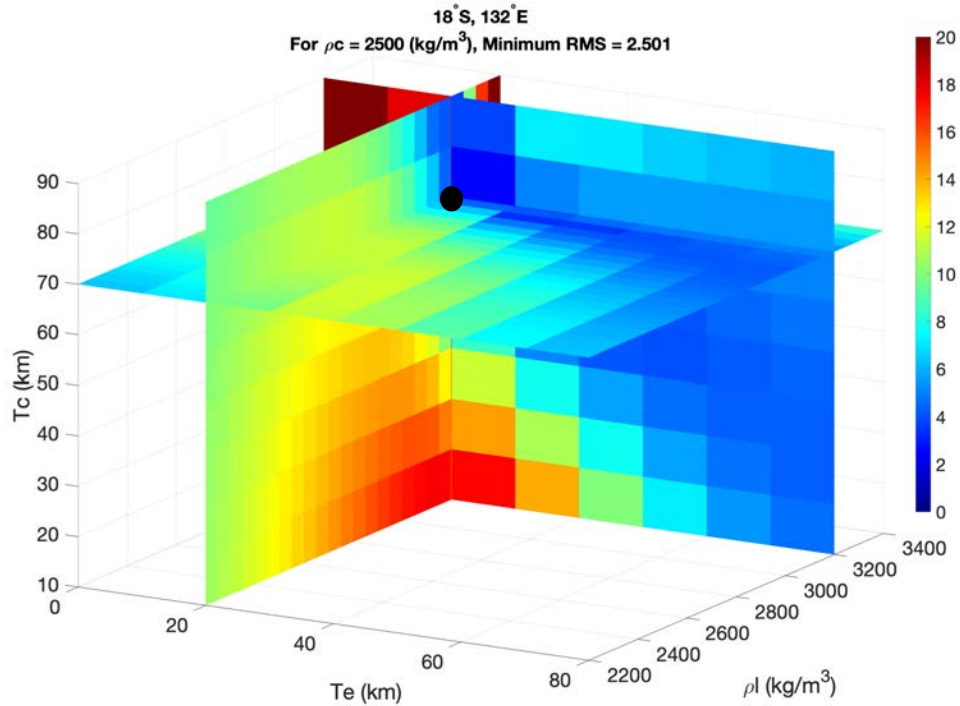


Figure 4.6 RMS space of crustal thickness, elastic thickness, and load density at location 18°S, 132°E. This plot uses a constant crustal density of 2500kgm⁻³, which corresponds to the crustal density leading to the lowest RMS parameter combination (noted by the black circle, corresponding to Figure 4.5a).

Continuing to move eastward along the CDB, location 24°S, 149°E has a substantial amount of topographic variation within the window (Figure 3.2). The observed admittance spectra within this window (Figure 4.7) can be better estimated by the mass-sheet approximation than any previous location because it has a relatively smooth, gradual slope from degrees 30 – 50 without any major inflections. There is a gradual dip in the observed curve from degrees 60 – 80, but since the mass sheet approximation best represents lower degrees, the range of 30 – 50 is used for analysis.

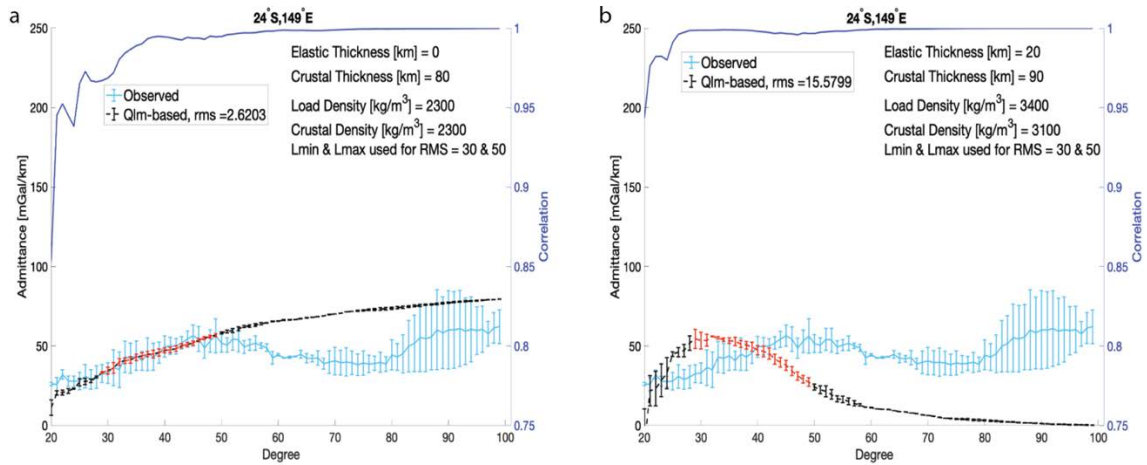


Figure 4.7 Observed (light blue) and theoretical (black) admittance for the 15° spherical cap windowed region centered at 24°S, 149°E. Overlapping parts of observed and theoretical admittances are shown in red on the theoretical spectrum. (a) the minimum RMS case and (b) a case of an ill-fitting spectrum outside of the acceptable criteria range. Elastic thickness, crustal thickness, load density, crustal density and the spectral range used for each theoretical curve are noted. Theoretical degree correlation is shown in dark blue. Vertical bars are error estimates on the spectra.

The minimum RMS of 2.62mGal/km for the above location (Figure 4.7a) remains within the observed error and matches the slope for the lower degrees region used. Outside of this, degrees 20-30 are well matched; however, it was difficult to match the portion of the spectra from 50 – 100 due to the drop in degree correlation for this range. Some acceptable fits within error bars of observed and theoretical were able to better capture the higher degree portion of the spectra (50-100); however, they were less well fitting within the range of interest (30 – 50) thus producing a slightly higher RMS. Since this observed curve can be decently well estimated by the mass sheet approximation, parameter combinations that are within the selection criteria are found until an RMS of 15mGal/km. The spectra beyond this value have opposing slope and are outside of the observed error (e.g., Figure 4.7b). Additionally, the fit outside of degrees 30 – 50 is worse than that with lower RMS as it does not overlap with the observed error and

follows a very different trend. Spectra with RMS near the minimum RMS but different parameter combinations are shown in Figure A.7 and A.8.

From the 9.2% of the RMS space that holds acceptable solutions (with maximum RMS of 163.48mGal/km), parameter ranges were able to be estimates as: crustal thickness of 50-80km, crustal density of 2200-2500kgm⁻³, load density of 2200-2700kgm⁻³ and elastic thickness of 0-50km. It is likely that the large range of elastic thickness values came from the suitability of the observed curve for the mass-sheet approximation; many parameter combinations were considered to be within error bars of observed and theoretical. Further, there were well fitting combinations that included an elastic thickness up to 70km however all spectra using an elastic thickness over 50km produced a wavy degree correlation lower than 0.9 for the majority of spectral degrees between 30 and 50. Since the lower degree correlation implies large phase difference between the topography and theoretical gravity signals, elastic thicknesses above 50km were not considered to be reliable estimates. Additionally, it is of note that many of the acceptable load and crustal density combinations were within 100-200kgm⁻³ of each other, implying that load and crustal density could be similar for this location.

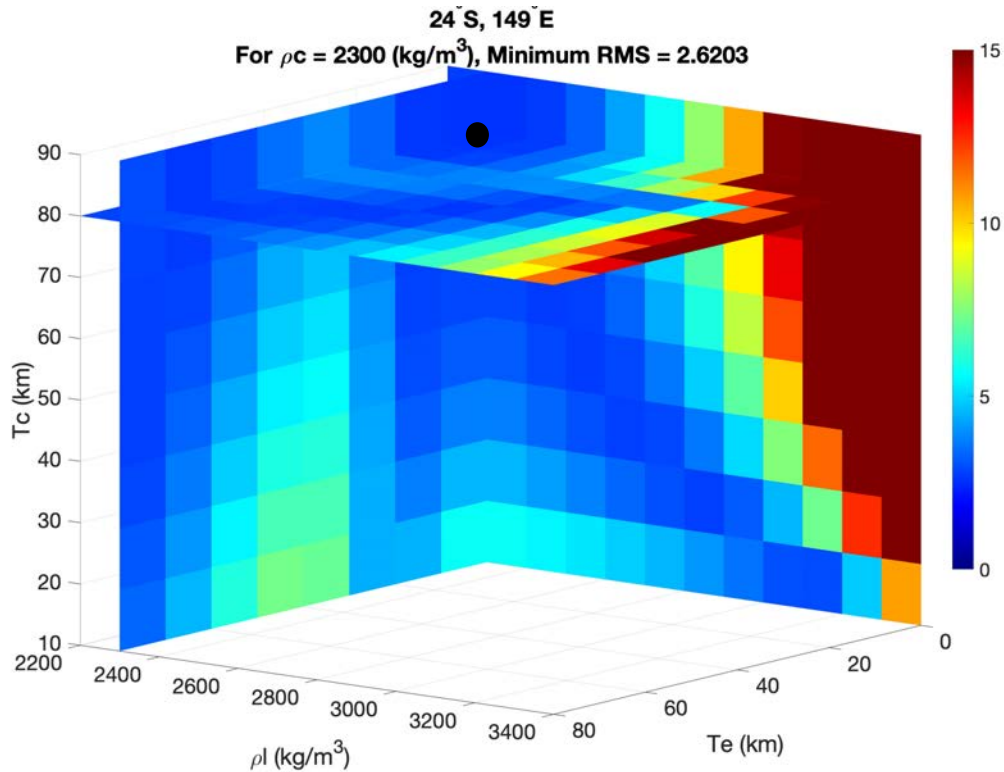


Figure 4.8 RMS space of crustal thickness, elastic thickness, and load density at location 24°S, 149°E. This plot uses a constant crustal density of 2300kgm^{-3} , which corresponds to the crustal density leading to the lowest RMS parameter combination (noted by the black circle, corresponding to Figure 4.7a).

On the eastern side of this region of the CDB, location 32°S, 165°E has a fair amount of cratering and slightly lower elevation topography than the previous region (Figure 3.2). Observed admittance spectra for this location have an inflection from degrees 20 – 35 that cannot be reproduced using localized admittance method with mass-sheet approximation. Degrees 40 – 65 are fit within error bars of observed by theoretical curves that match the slope, remain well within the observed error and follow the spectra from degrees 20 – 100 (Figure 4.9a).

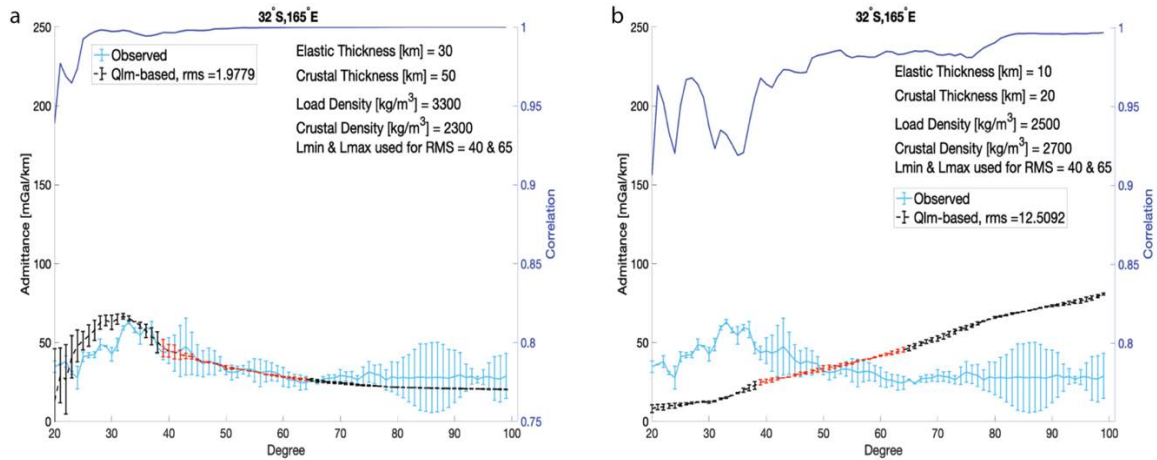


Figure 4.9 Observed (light blue) and theoretical (black) admittance for the 15° spherical cap windowed region centered at 32°S, 165°E. Overlapping parts of observed and theoretical admittances are shown in red on the theoretical spectrum. (a) the minimum RMS case and (b) a case of an ill-fitting spectrum outside of the acceptable criteria range. Elastic thickness, crustal thickness, load density, crustal density and the spectral range used for each theoretical curve are noted. Theoretical degree correlation is shown in dark blue. Vertical bars are error estimates on the spectra.

Using the theoretical and observed spectra between degrees 40 – 65, the minimum RMS obtained is 1.98mGal/km, which is one of the lowest RMS for all modeled spectra in the highlands region. Figure 4.9a shows that theoretical curves of low RMS are within selection criteria and are able to stay within the range of the observed admittance from 20-100 degrees sufficiently well. Many parameter combinations produce similarly well-fitting theoretical curves until an RMS of 12mGal/km. Exceeding that (Figure 4.9b), the mass-sheet admittances begin to exhibit opposing slopes to the observed and / or are well beyond the observed error range. Further, correlations are often less than 0.9 for portions of the spectra with RMS greater than 12mGal/km and degrees 20-100 cannot be well matched in terms of the range of observed admittance. A maximum RMS of 121.94mGal/km leads to 10% of the total RMS space containing numerically acceptable and visually reasonable (i.e., fitting within error bars of observed and theoretical)

parameter combinations. This results in estimates of crustal thickness 40-80km (40-65km in Goossens et al., 2017), crustal density 2200-2400kgm⁻³, load density 2800-3400kgm⁻³ and elastic thickness 20-50km.

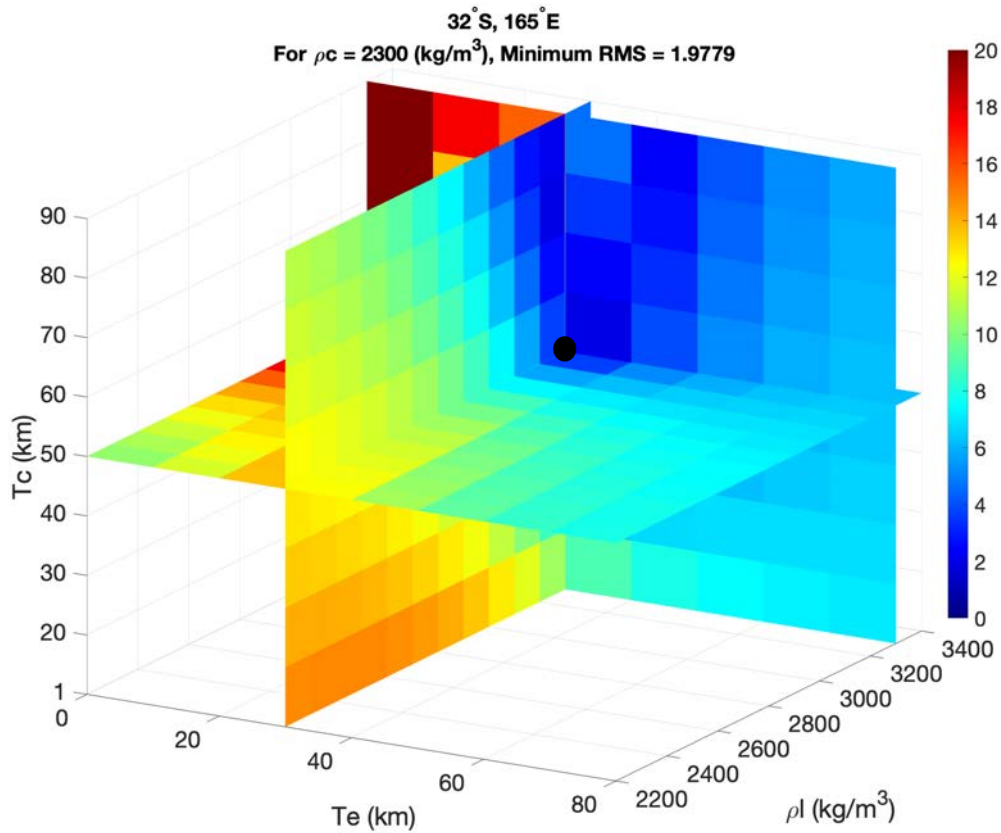


Figure 4.10 RMS space of crustal thickness, elastic thickness, and load density at location 32°S, 165°E. This plot uses a constant crustal density of 2300kgm⁻³, which corresponds to the crustal density leading to the lowest RMS parameter combination (noted by the black circle, corresponding to Figure 4.9a).

The final location in the Southern Highlands region of the CDB studied is 24°S, 185°E (Figure 3.2). In Figure 4.11a, a large hump is visible in the observed spectra between degrees 30 – 50 which cannot be replicated using a mass sheet approximation. However, degrees 55 – 75 have a smooth, gradual slope with relatively few inflections, making it possible to estimate parameters with the mass sheet approach. From this degree

range, the lowest RMS is 1.39mGal/km (Figure 4.11a), making it the lowest RMS achieved in both the highlands and lowlands regions investigated in this study. Figure 4.11a shows that most of the theoretical curve staying well within the middle of the observed error and matching the slope very well, except degrees 30-50 where admittances fall well below the observed range. Theoretical curves fit within error bars of observed and theoretical almost up to the RMS of 11mGal/km. Beyond 11mGal/km to the maximum RMS of 67mGal/km (an example in Figure 4.11b), the theoretical curves are not sufficiently within the range of the observed admittance error estimates and also have opposite slope to the observed with high misfit RMS value.

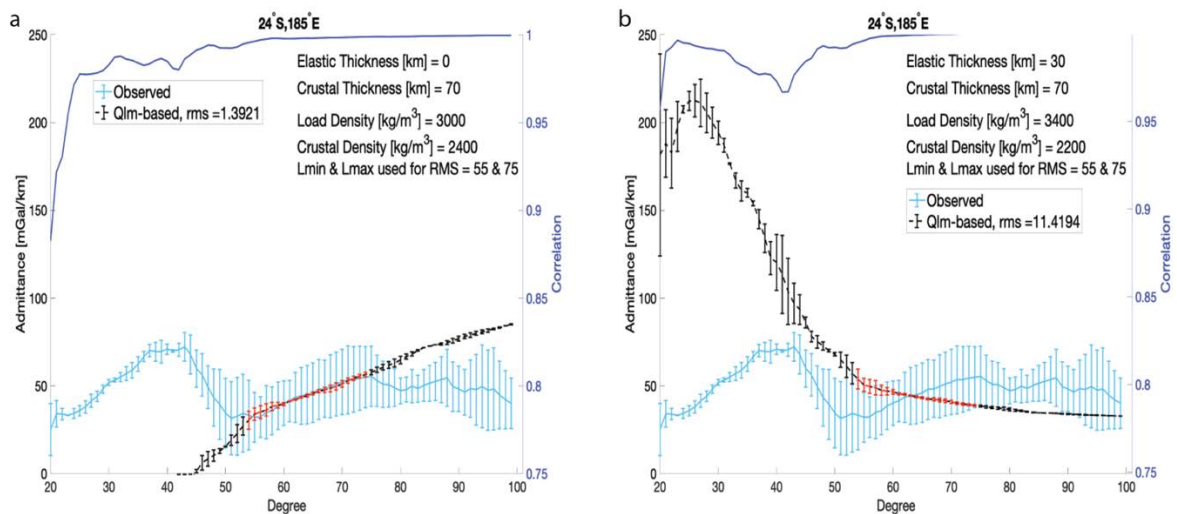


Figure 4.11 Observed (light blue) and theoretical (black) admittance for the 15° spherical cap windowed region centered at 24°S, 185°E. Overlapping parts of observed and theoretical admittances are shown in red on the theoretical spectrum. (a) the minimum RMS case and (b) a case of an ill-fitting spectrum outside of the acceptable criteria range. Elastic thickness, crustal thickness, load density, crustal density and the spectral range used for each theoretical curve are noted. Theoretical degree correlation is shown in dark blue. Vertical bars are error estimates on the spectra.

The maximum RMS of 67mGal/km is lower than other regions in the highlands.

Although it is still possible to discern grossly incorrect parameter combinations, it is

more difficult to determine parameter estimates within the acceptable solution space, which comprises 16% of the total RMS space. Estimated parameter ranges for this location are crustal thickness between 40 – 80km (50-70km in Goossens et al., 2017), crustal density between 2200-2500 kgm^{-3} , load density between 2200 – 3200 kgm^{-3} and elastic thickness between 0 – 20km.

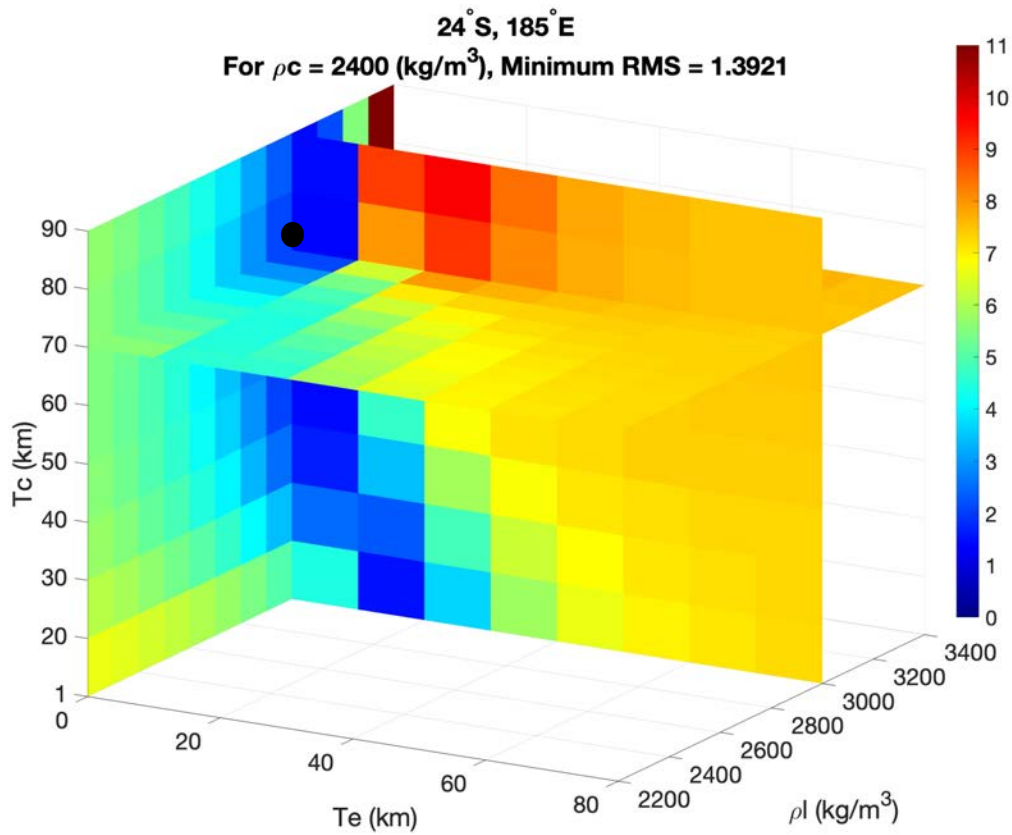


Figure 4.12 RMS space of crustal thickness, elastic thickness, and load density at location 24°S, 185°E. This plot uses a constant crustal density of 2400 kgm^{-3} , which corresponds to the crustal density leading to the lowest RMS parameter combination (noted by the black circle, corresponding to Figure 4.11a).

4.2 Admittance modeling in the Northern Lowlands north of the CDB

Beginning on the western side of the study region, the first location north of the CDB is 20°N , 98°E . This very low-lying, flat region is near the Isidis crater and Perseverance rover landing site (Figure 3.2). Figure 4.13 shows that the observed admittance spectrum for this location has many inflections that are difficult for theoretical curves to reproduce. Using the mass-sheet approach and the range of values tested here, we were unable to find an acceptable fit and thus could not estimate crustal thickness, crustal density, load density or elastic thickness.

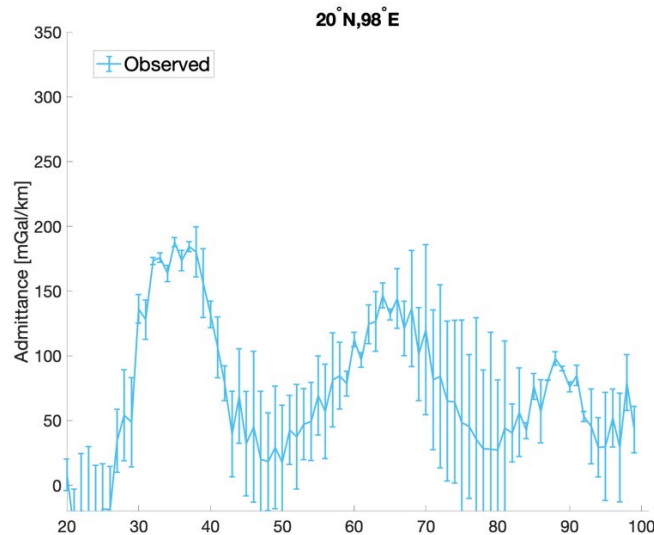


Figure 4.13 Observed admittance spectra for 20°N , 98°E . Error bars are standard error as in the other figures.

The region centered at 19°N , 116°E is east of Isidis crater and has slightly more, though still not significant, topographic variation and visible cratering (Figure 3.2). Since there is very little topographic variation in this region, fits that are within the observed error for low degrees will be more meaningful than higher degree fits. Considering the

observed spectrum (Figure 4.14) and meaningful degrees, we can fit degrees 30 - 55 within the error estimates of the two curves.

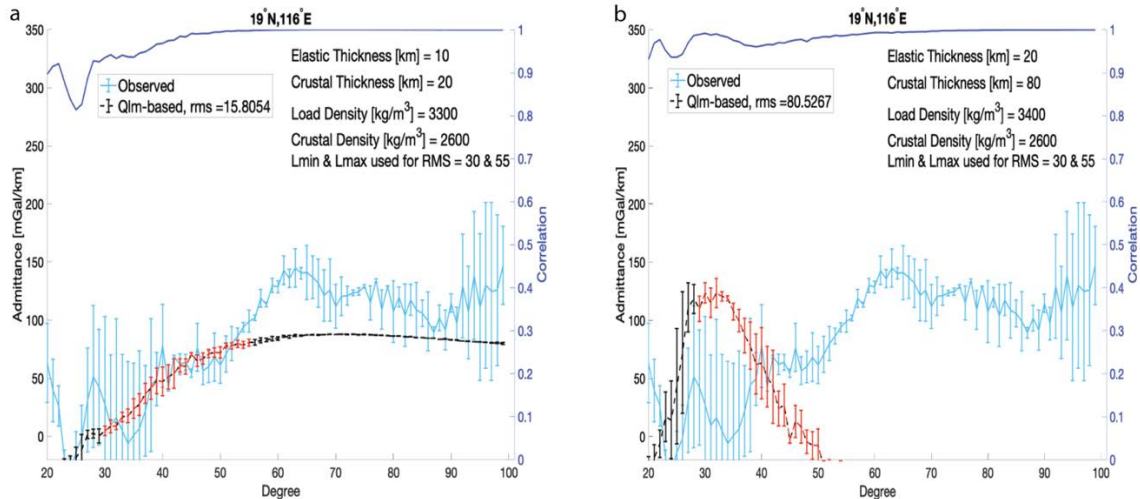


Figure 4.14 Observed (light blue) and theoretical (black) spectra for 19°N, 116°E. The modeled degree range is in red with theoretical correlation in dark blue. The parameter values used to produce each theoretical curve are given on the figure. (a) minimum RMS case and (b) trial of a model attempting to fit the first peak in the observed spectrum. Theoretical degree correlation is shown in dark blue. Vertical bars are standard error estimates on the spectra.

Figure 4.14a shows the minimum RMS case of 15.81mGal/km and the space of RMS misfit for crustal thickness, load density and elastic thickness is shown in Figure 4.15. Fits within error bars of observed and theoretical are found up to an RMS of 60mGal/km. Figure 4.15b shows an example of a grossly ill-fitting parameter combination that is well outside of the acceptable RMS range. With a maximum RMS of 235.4, 73% of the total RMS space can be excluded from the solution space by not meeting selection criteria. Within the remaining space, crustal thickness and density are constrained to 10 – 40km and 2300 – 2600kgm⁻³ (Goossens et al., 2017), load density is not able to be constrained (2200 – 3400kgm⁻³) and elastic thickness is estimated to be between 0 - 20km.

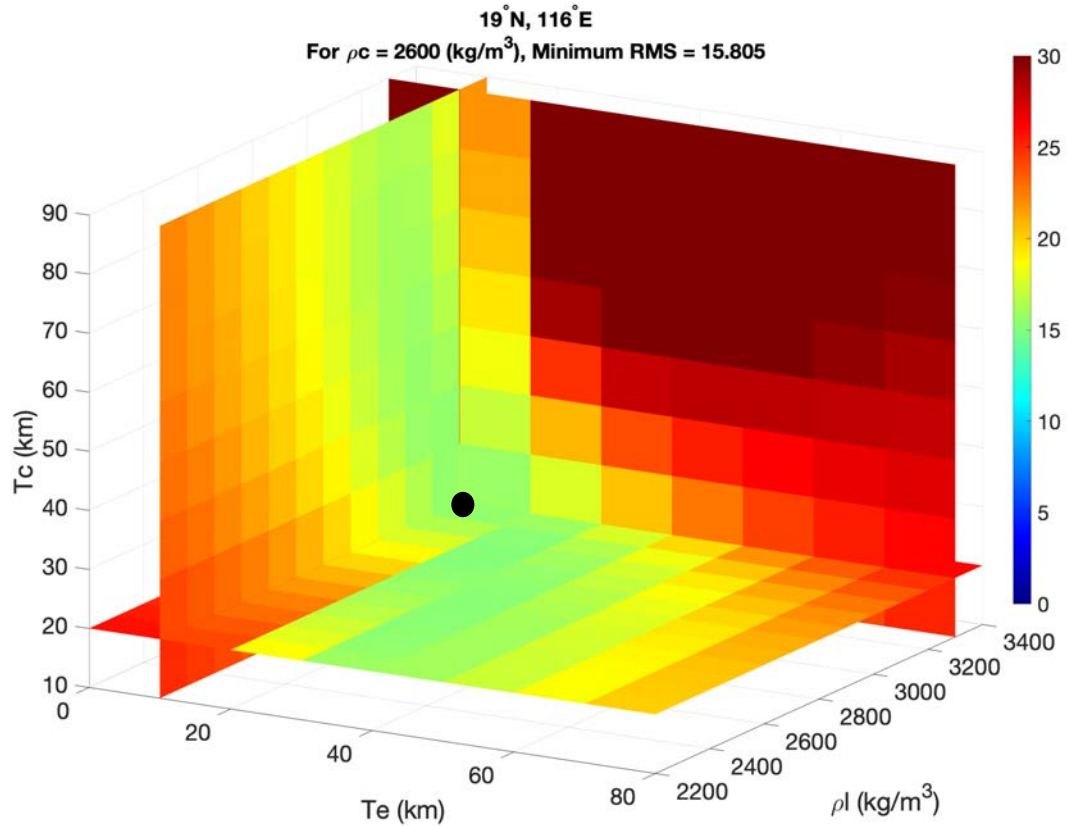


Figure 4.15 RMS space of crustal thickness, elastic thickness, and load density at location 19°S, 116°E. This plot uses a constant crustal density of 2600kgm^{-3} , which corresponds to the crustal density leading to the lowest RMS parameter combination (noted by the black circle, corresponding to Figure 4.15a).

Near the middle of the northern study region, location 12°N, 132°E is south of Elysium volcano and has slightly more topographic variation than the previous locations, although it is still predominantly flat and low-lying (Figure 3.2). This region is far enough away from Elysium to not be significantly affected by its topographic and gravitational signal. The observed admittance for 12°N, 132°E between degrees 25-55 is considered for the analysis as it is almost within the error estimates of the mass-sheet approximation (Figure 4.16a).

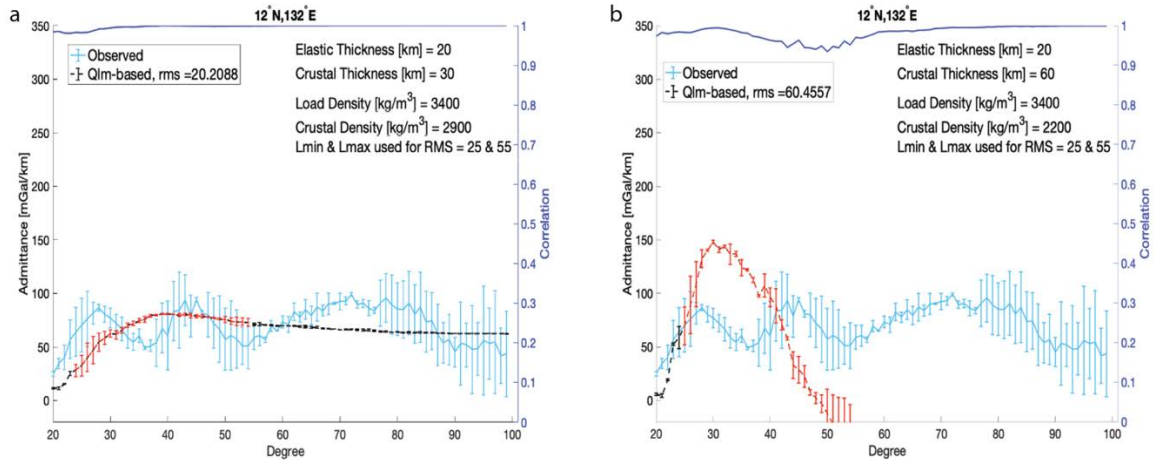


Figure 4.16 Observed (light blue) and theoretical (black) spectra for 12°N, 132°E. The modeled degree range is in red with theoretical correlation in dark blue. The parameter values used to produce each theoretical curve are given on the figure. (a) the minimum RMS case and (b) a case of an ill-fitting spectrum outside of the acceptable criteria range. Theoretical degree correlation is shown in dark blue. Vertical bars are standard error estimates on the spectra.

Figure 4.16b is an example of an incorrect parameter combination outside of the reasonably-fitting curves (RMS up to 45mGal/km). This is an example of a fit attempting to identify parameter combinations for modeling the peak from degrees 25 – 35 and shows that such peaks/features are not conducive for modeling with the mass sheet approximation.

Non-fitting curves make up the total RMS space beyond an RMS of 45mGal/km, thus ~85% of the RMS space is not considered. Within the remaining 15%, crustal thickness is estimated between 10 – 40km, crustal density between 2300 – 2900kgm⁻³, load density between 2800 – 3400kgm⁻³ and elastic thickness between 0 – 20km.

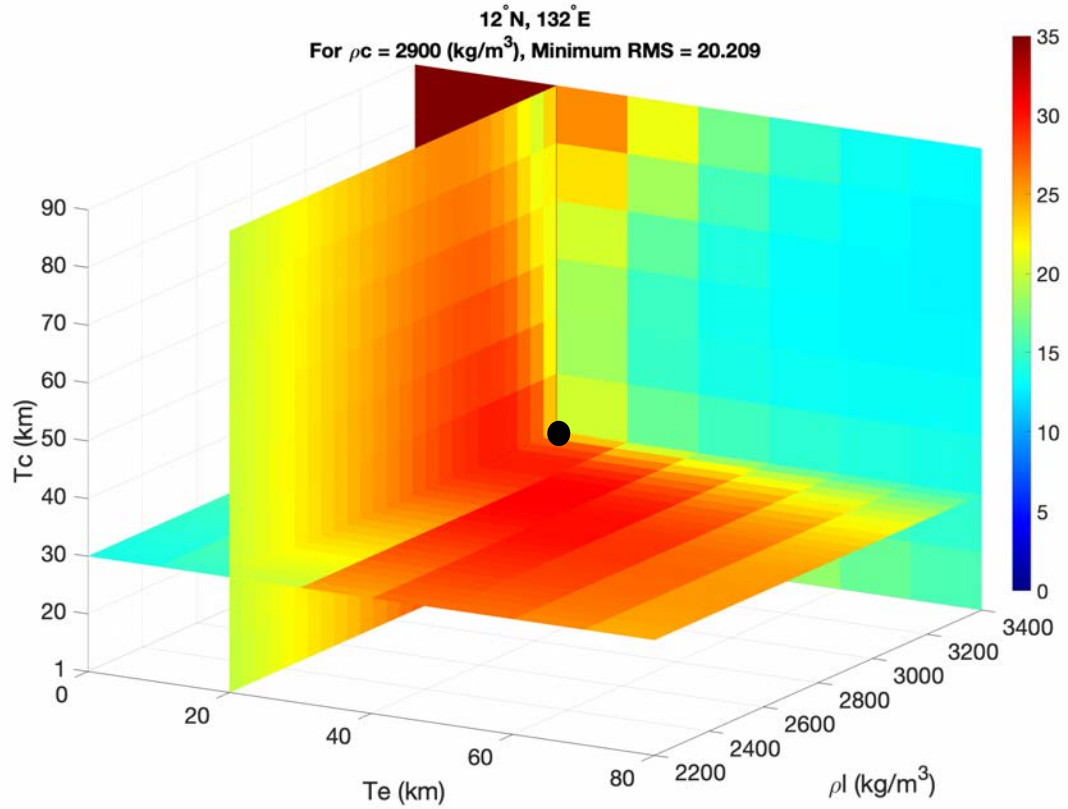


Figure 4.17 RMS space of crustal thickness, elastic thickness, and load density at location 12°S, 132°E. This plot uses a constant crustal density of 2900 kgm^{-3} , which corresponds to the crustal density leading to the lowest RMS parameter combination (noted by the black circle, corresponding to Figure 4.17a).

The next location north of the CDB in the lowlands is 5°N, 149°E and similarly to the previous location, it is near Elysium volcano, lacking much topographic variation. A degree range from 35 – 65 degrees is used for analysis here due to observed admittance features (Figure 4.18).

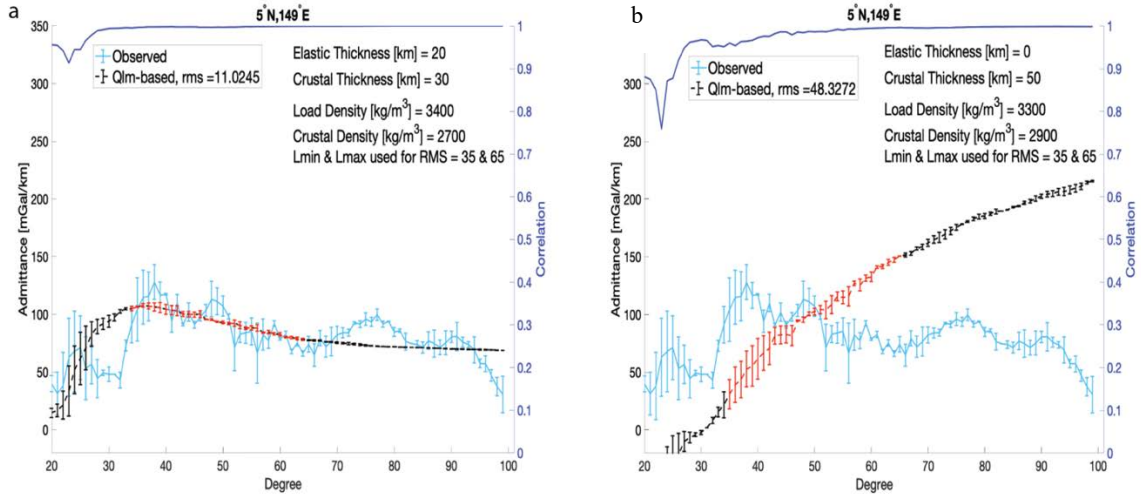


Figure 4.18 Observed (light blue) and theoretical (black) spectra for 5°N, 149°E. The modeled degree range is in red with theoretical correlation in dark blue. The parameter values used to produce each theoretical curve are given on the figure. (a) the minimum RMS case and (b) a case of an ill-fitting spectrum outside of the acceptable criteria range. Theoretical degree correlation is shown in dark blue. Vertical bars are standard error estimates on the spectra.

The minimum RMS for this location is 11.02mGal/km (Figure 4.18a) and the modeled fit is within the error estimates of the curves. Parameter combinations produce decent curve approximations until an RMS of 30mGal/km (example in Figure 4.18b). The parameter combination in Figure 4.18b is grossly incorrect, as the theoretical curve is well outside of the range of the observed admittance. The peak from degrees 30 – 40 could not be matched. Poor fits outside of the observed error range were produced from RMS of 30mGal/km to a maximum RMS of 229.68mGal/km. Thirteen percent of the theoretical curve within the entire RMS space produces fits within error bars of observed and theoretical. Using the same logic as previously discussed, crustal thickness is estimated between 10-30km, crustal density between 2500 – 2900kgm⁻³, load density of 2600-3400kgm⁻³ and elastic thickness between 0 – 30km.

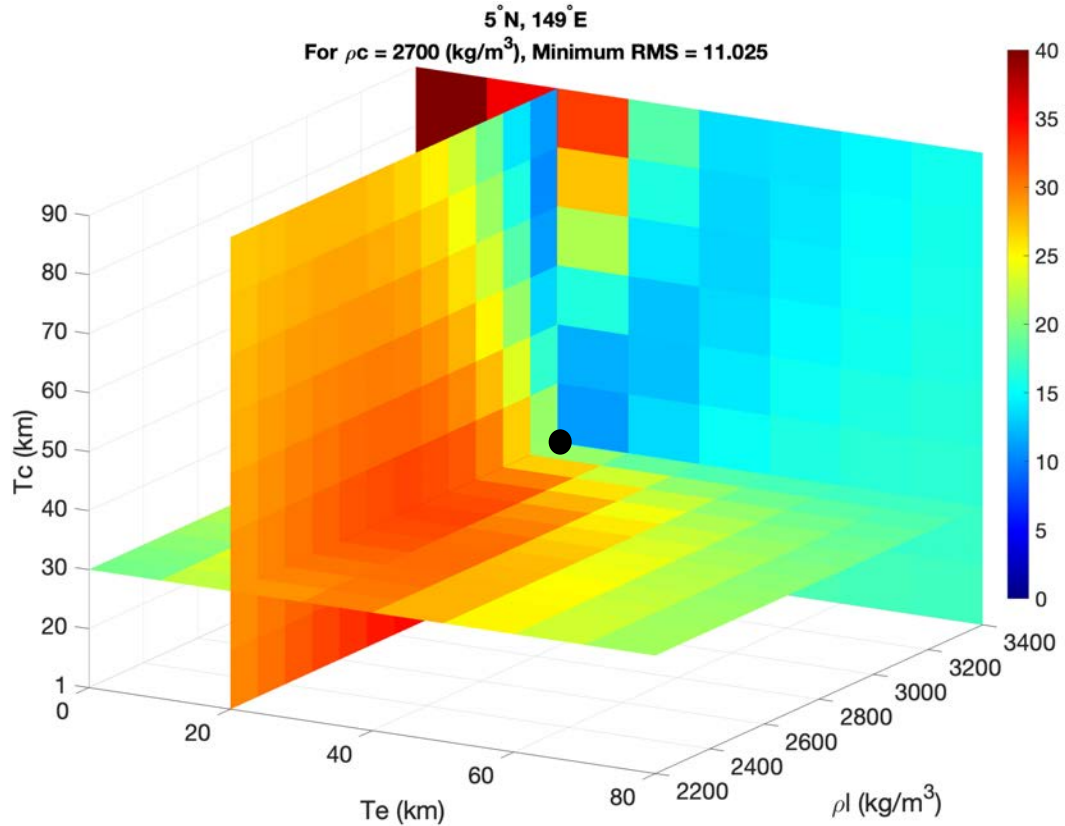


Figure 4.19 RMS space of crustal thickness, elastic thickness, and load density at location 5°S, 149°E. This plot uses a constant crustal density of 2700kgm^{-3} , which corresponds to the crustal density leading to the lowest RMS parameter combination (noted by the black circle, corresponding to Figure 4.18a).

The southernmost window on northern side of the CDB studied here is centered at 2°S, 185°E. In Figure 3.2, one can see that although in the southern hemisphere of the planet, it is still north of the CDB near a transition zone from highlands to lowlands. This location has more topographic variation and higher elevation features than any previous lowland location analyzed. The observed spectrum for this location (Figure 4.20) is distinct from previous lowlands sites. The observed admittance curve lacks sharply changing slope features (such as between degrees 75 – 100 of the window at 19°N, 116°E). Rather, its variations occur over a longer range of spectral degrees, making the

observed curve appear smoother or less jagged (for instance, the variations between degrees 30 – 45 are not as sharp). Thus, we can estimate the lower degree range of 30 – 50 that is best suited for the mass- sheet approximation.

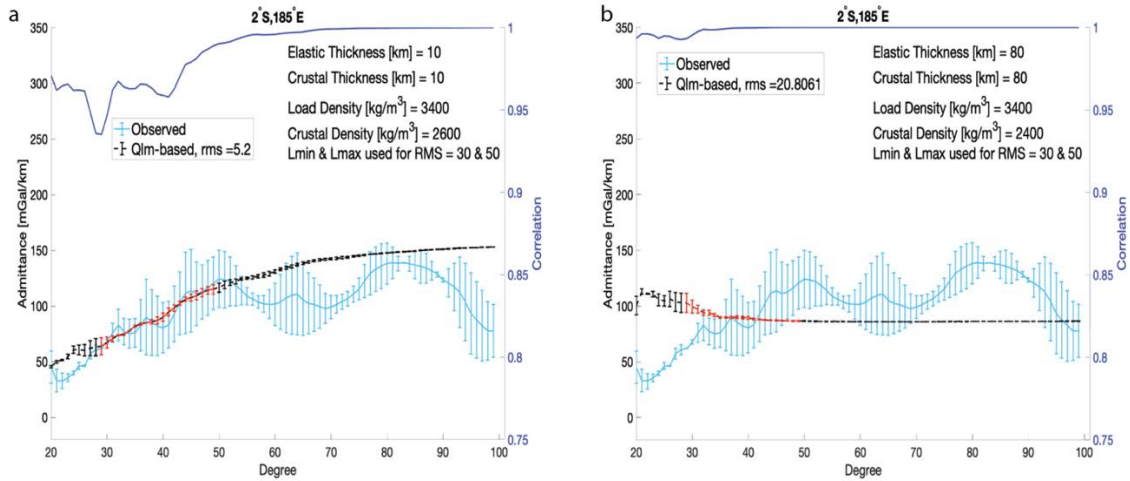


Figure 4.20 Observed (light blue) and theoretical (black) spectra for 2°S, 185°E. The modeled degree range is in red with theoretical correlation in dark blue. The parameter values used to produce each theoretical curve are given on the figure. (a) the minimum RMS case and (b) a case of an ill-fitting spectrum outside of the acceptable criteria range. Theoretical degree correlation is shown in dark blue. Vertical bars are standard error estimates on the spectra.

The minimum RMS achieved is 5.2mGal/km and Figure 4.20a shows that the calculated admittance curve is well within the error bars and matches the slope of the observed for the modeled degrees. Conversely, beyond an RMS of 20mGal/km, the theoretical spectra exclusively have incorrect slopes and do not reflect the entire range (Figure 4.20b). This remains the case until the maximum RMS of 172.18mGal/km, resulting in 12% of the total RMS space containing possible solutions. Crustal thickness and density were constrained within 10 – 30km (10 – 40km in Goossens et al., 2017) and 2200 – 3200kgm⁻³ (2400 – 3200kgm⁻³ in Goossens et al., 2017). Load density was not as

well constrained, with values of $2200 - 3200\text{kgm}^{-3}$ present, and elastic thickness is estimated between $0 - 30$ km.

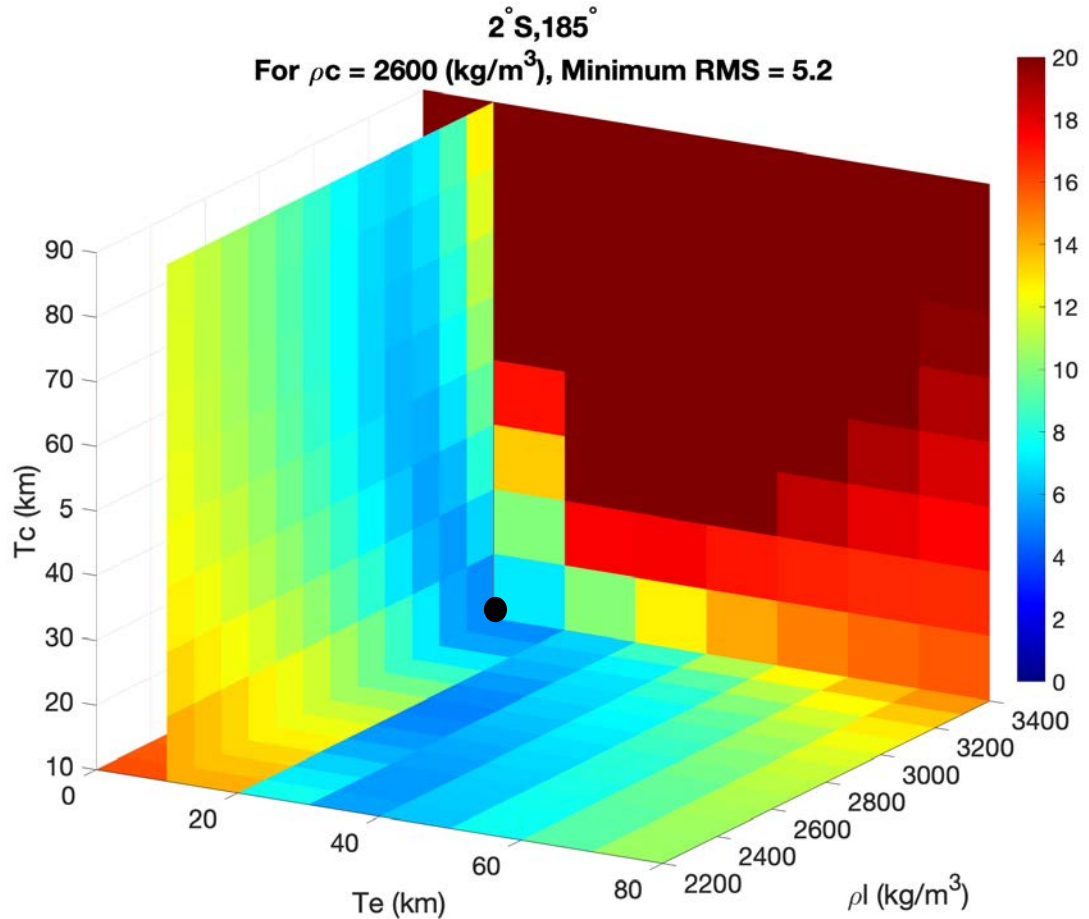


Figure 4.21 RMS space of crustal thickness, elastic thickness, and load density at location $2^{\circ}\text{S}, 185^{\circ}\text{E}$. This plot uses a constant crustal density of 2600kgm^{-3} , which corresponds to the crustal density leading to the lowest RMS parameter combination (noted by the black circle, corresponding to Figure 4.21a).

The final northern lowland location in this study is centered at $1^{\circ}\text{N}, 200^{\circ}\text{E}$. Figure 3.2 again suggests a transition zone like features of the CDB within this region and significantly more topographic variation than most other lowlands locations. The observed spectrum (Figure 4.22) has generally smooth features that can be reasonably

well fit by the mass sheet approximation for a large range of degrees. Thus, we can model degrees 30 – 50 or 40-60.

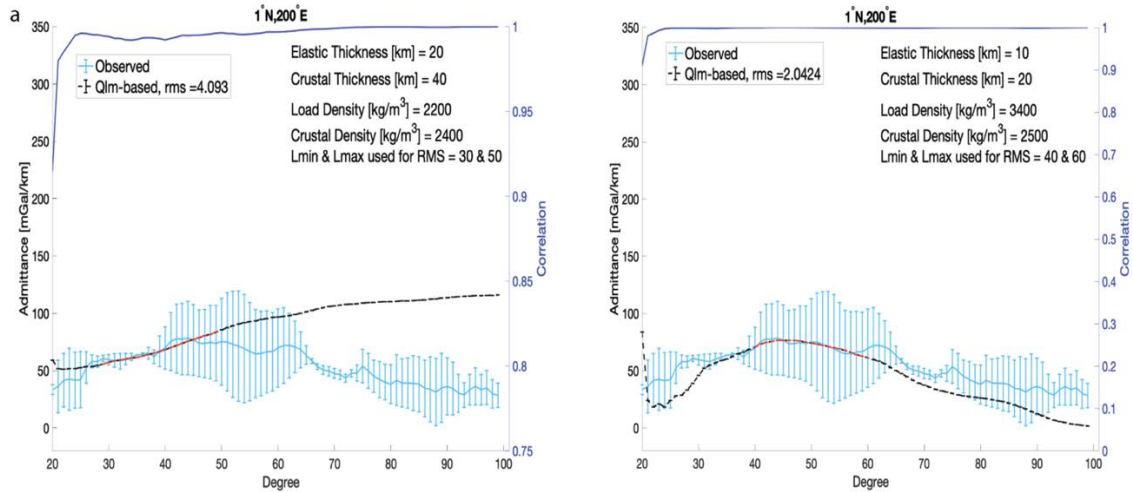


Figure 4.22 Observed (light blue) and theoretical (black) spectra for 1°N, 200°E. The modeled degree range is in red with theoretical correlation in dark blue. The parameter values used to produce each theoretical curve are given on the figure. (a) the minimum RMS case and (b) a case of an ill-fitting spectrum outside of the acceptable criteria range. Theoretical degree correlation is shown in dark blue. Vertical bars are standard error estimates on the spectra.

Figure 4.22a and b both show minimum RMS cases for two different degree ranges that are well matched by theoretical admittance curves. For Figure 4.22a using degrees 30 – 50, the minimum RMS is 4.09mGal/km with a maximum RMS of 140.91mGal/km and acceptable estimates below an RMS of 25mGal/km. This is higher than the minimum RMS using degrees 40 – 60 (Figure 4.22b), which is 2.042mGal/km. The maximum RMS for degrees 40 – 60 is 138.92mGal/km and has acceptable solutions until 20mGal/km. Although the two sets of solutions have different RMSs, the resulting parameter estimates are the same for both ranges for most of the parameters.

There is a rather wide range of possible parameter values that fit within the values constrained by Goossens et al. (2017) for crustal thickness (10 – 40km) and crustal density (2300-2600kgm⁻³). It was not possible to constrain the load density using its entire parameter space, having values between 2200-3200kgm⁻³ and elastic thickness also had a wide range, between 0 – 50km.

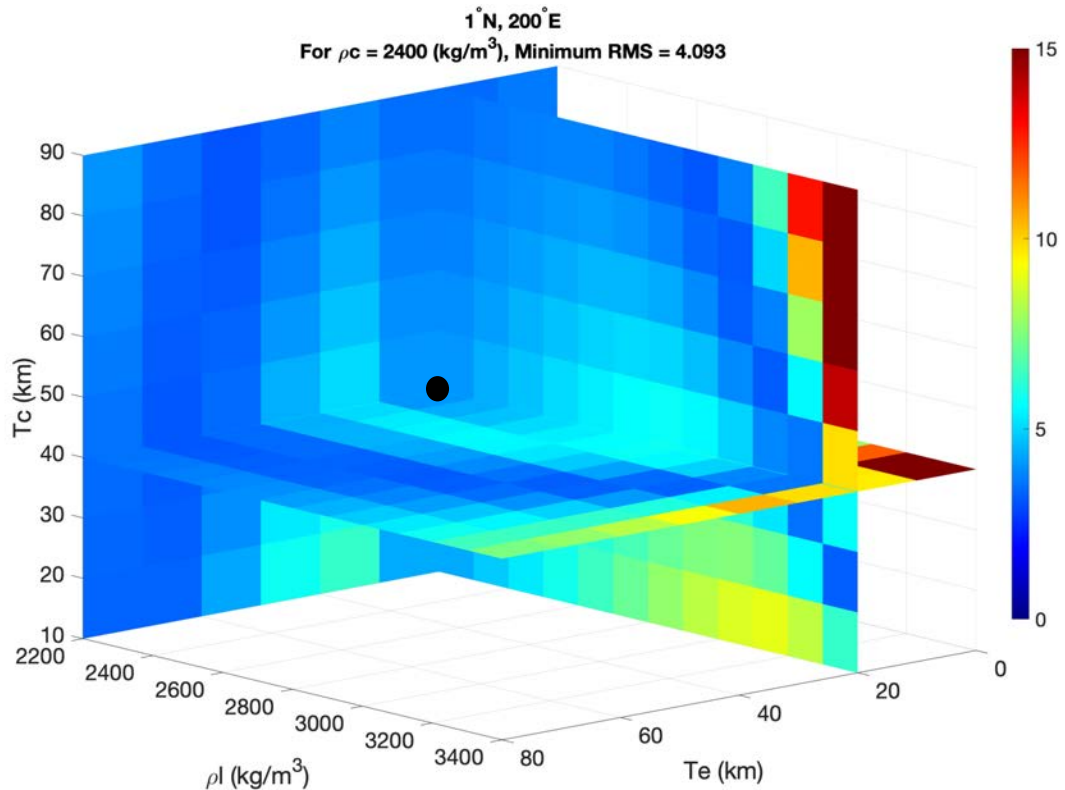


Figure 4.23 RMS space of crustal thickness, elastic thickness, and load density at location 1°S, 200°E using spectral degrees 30 -50. This plot uses a constant crustal density of 2400kgm⁻³, which corresponds to the crustal density leading to the RMS parameter combination shown in Figure 4.22a.

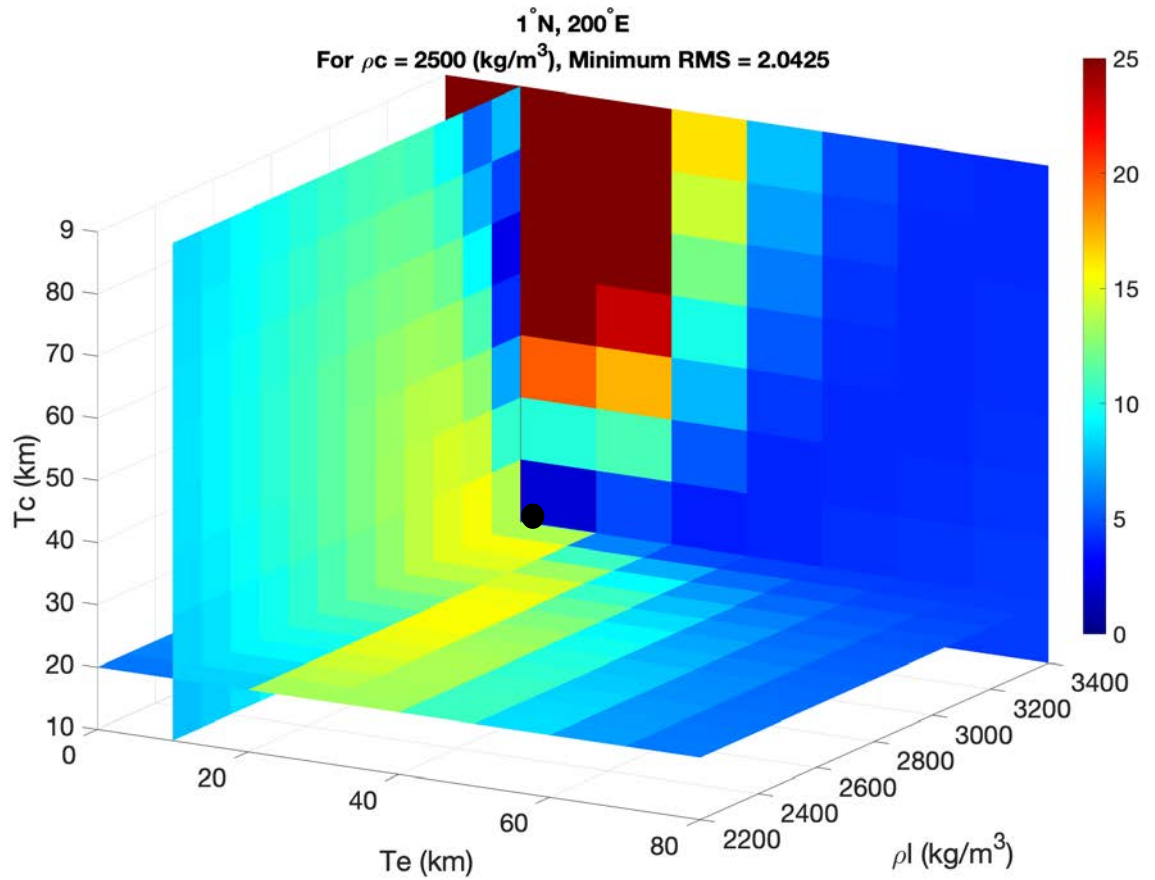


Figure 4.24 RMS space of crustal thickness, elastic thickness, and load density at location 1°S, 200°E using spectral degrees 40 - 60. This plot uses a constant crustal density of 2500 kgm^{-3} , which corresponds to the crustal density leading to the lowest RMS with reasonable parameter combination (noted by the black circle, corresponding to Figure 4.22b).

Table 4.1 Study locations, spectral range, and acceptable parameter ranges of elastic thickness, load density, crustal thickness and crustal density estimates.

	Latitude	Longitude	Spectral range	T_e [km]	ρ_t [g/cc]	T_c [km]	ρ_c [g/cc]
Highlands	10°S	98°E	48-71	10-30	2.9-3.1	50-70	2.2-2.5
	11°S	116°E	50-75	0-10	2.9-3.1	40-80	2.2-2.4
	18°S	132°E	30-50	20-50	2.3-3.2	50-70	2.2-2.5
	24°S	149°E	30-50	0-50	2.2-2.7	50-80	2.2-2.5
	32°S	165°E	40-65	20-50	2.8-3.4	40-80	2.2-2.4
	24°S	185°E	55-75	0-20	2.2-3.2	40-80	2.2-2.5
Lowlands	20°N	98°E	n/a	n/a	n/a	n/a	n/a
	19°N	116°E	30-55	0-20	2.2-3.4	10-40	2.3-2.6
	12°N	132°E	25-55	0-20	2.8-3.4	10-40	2.3-2.9
	5°N	149°E	35-65	0-30	2.6-3.4	10-30	2.5-2.9
	2°S	185°E	30-50	0-30	2.2-3.2	10-30	2.2-3.2
	1°N	200°E	30-50	0-50	2.2-3.2	10-40	2.3-2.6
	1°N	200°E	40-60	0-50	2.2-3.2	10-40	2.3-2.6

4.3 Special Cases

4.3.1 Locations centered on the CDB

To better understand the transition of crustal thickness, crustal density, load density and elastic thickness across the crustal dichotomy boundary, admittance modeling was done for three locations that are centered on the crustal dichotomy boundary, shown in Figure 4.25. The free air gravitational anomaly for the region is shown in Figure 4.26. The spherical cap window for each location straddles the highlands and lowlands regions using a 15° angular radius for the spherical cap window and a spectral bandwidth (L_w) of 17.

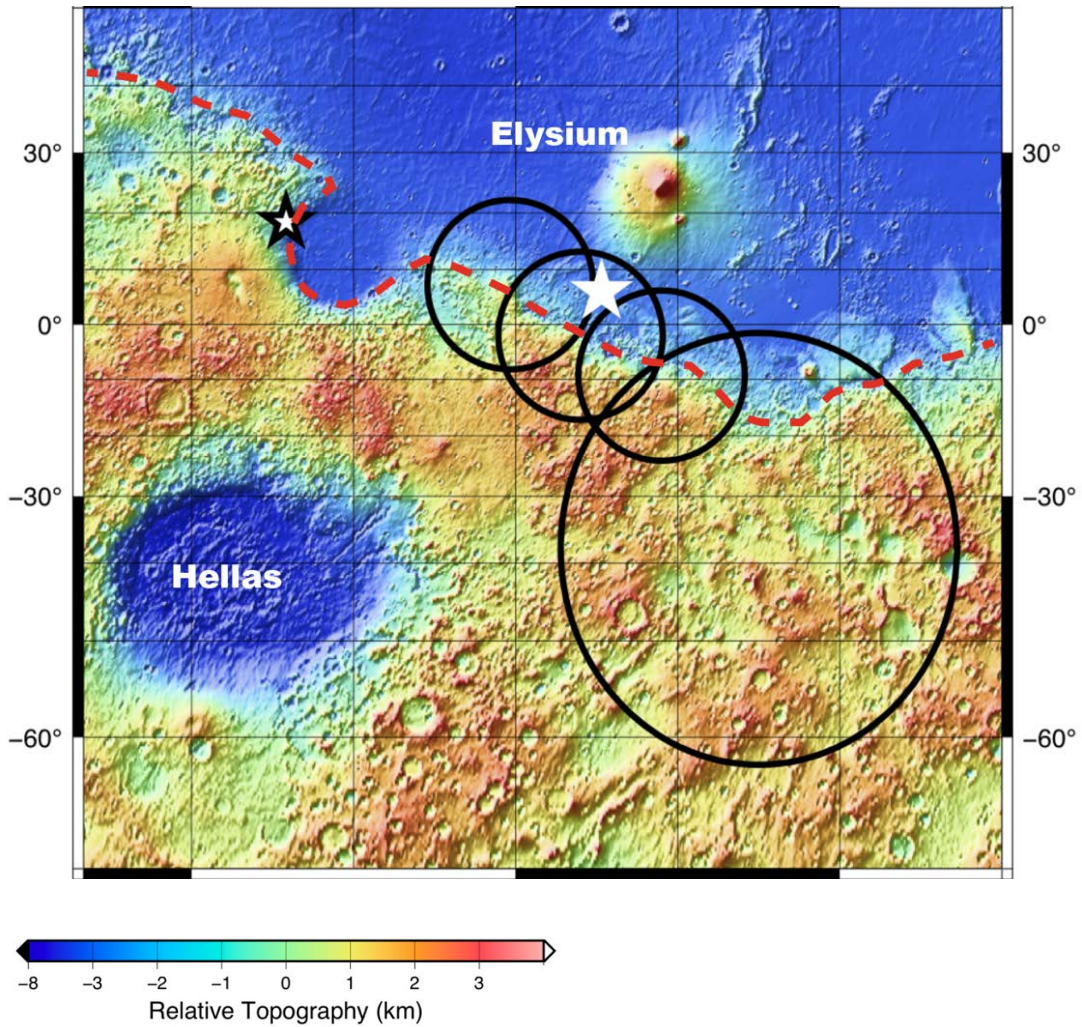


Figure 4.25 Special cases spherical cap window locations on Mola intensity and topography. White star denotes Insight landing spot, black outline star shows Perseverance rover landing spot and red dashed line approximates the CDB. The large circle shows the spherical cap of radius 30° centered on 32°S , 165°E that is discussed in section 4.3.2.

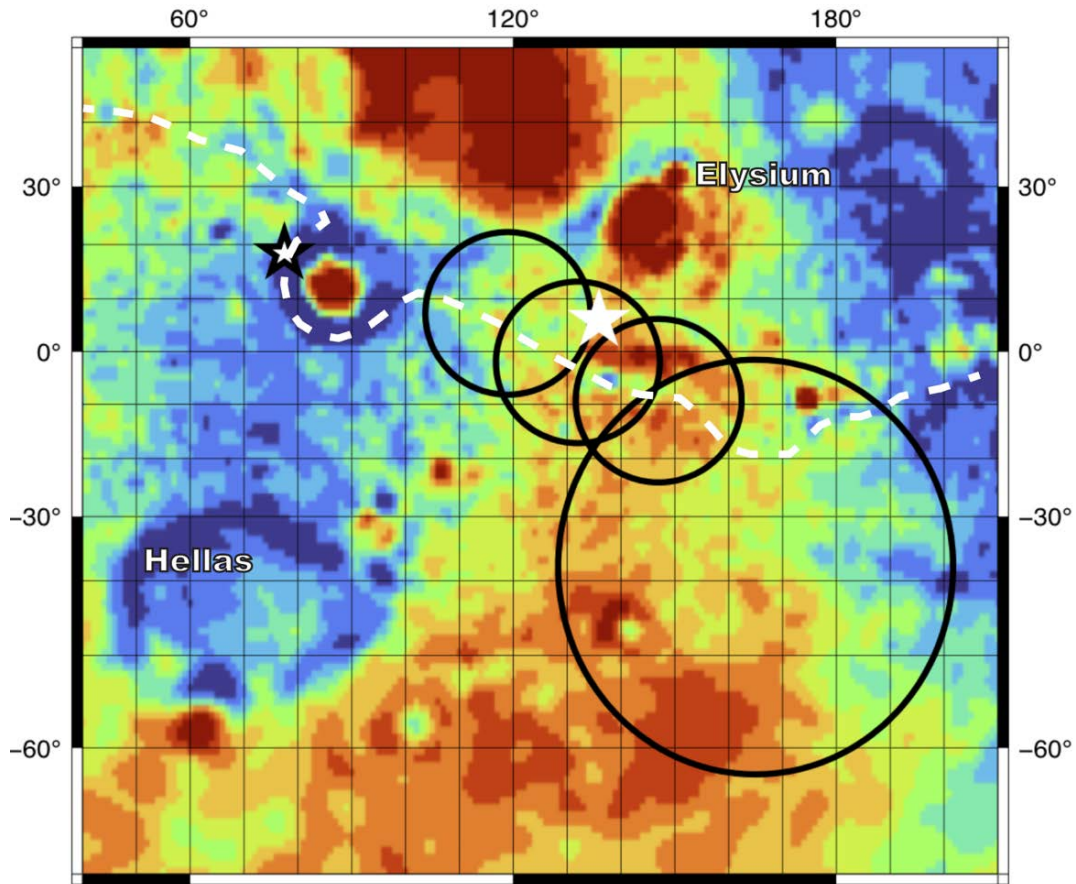


Figure 4.26 Special cases spherical cap window locations on GMM3 free air gravity anomaly. White star denotes Insight landing spot, black outline start shows Perseverance rover landing spot and white dashed line approximates the CDB.

The westernmost location is centered at 7°N, 119°E and includes portions of the Southern Highlands and Northern Lowlands within its spherical cap (Figure 4.25). There is a distinct topographic divide between low-lying and higher elevation features and thus the admittance signal represents an area of transition along the CDB. It is possible to consider theoretical admittance curves within the observed error for degrees 30 to 55, shown in Figure 4.27. The maximum RMS misfit between observed and theoretical admittance for this location is 438.69mGal/km and the minimum RMS is 2.34mGal/km. Acceptable fits that are within error bars of observed and theoretical were possible until an RMS of 15mGal/km. Using the same logic to exclude non-realistic values, 3.5% of the

total RMS space contains possible solutions. The crustal thickness is estimated to be between 30 – 70km, crustal density between 2200-2500kgm⁻³, load density between 2200 – 3200kgm⁻³ and elastic thickness between 0 – 50km.

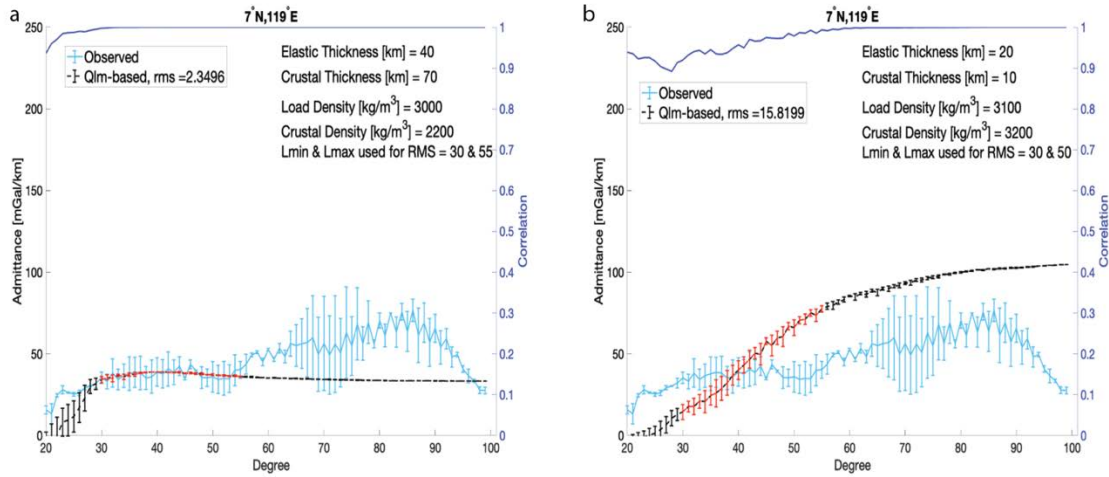


Figure 4.27 Observed (light blue) and theoretical (black) spectra for 7°N, 119°E. The modeled degree range is in red with theoretical correlation in dark blue. The parameter values used to produce each theoretical curve are given on the figure. (a) the minimum RMS case and (b) a case of an ill-fitting spectrum outside of the acceptable criteria range. Theoretical degree correlation is shown in dark blue. Vertical bars are standard error estimates on the spectra.

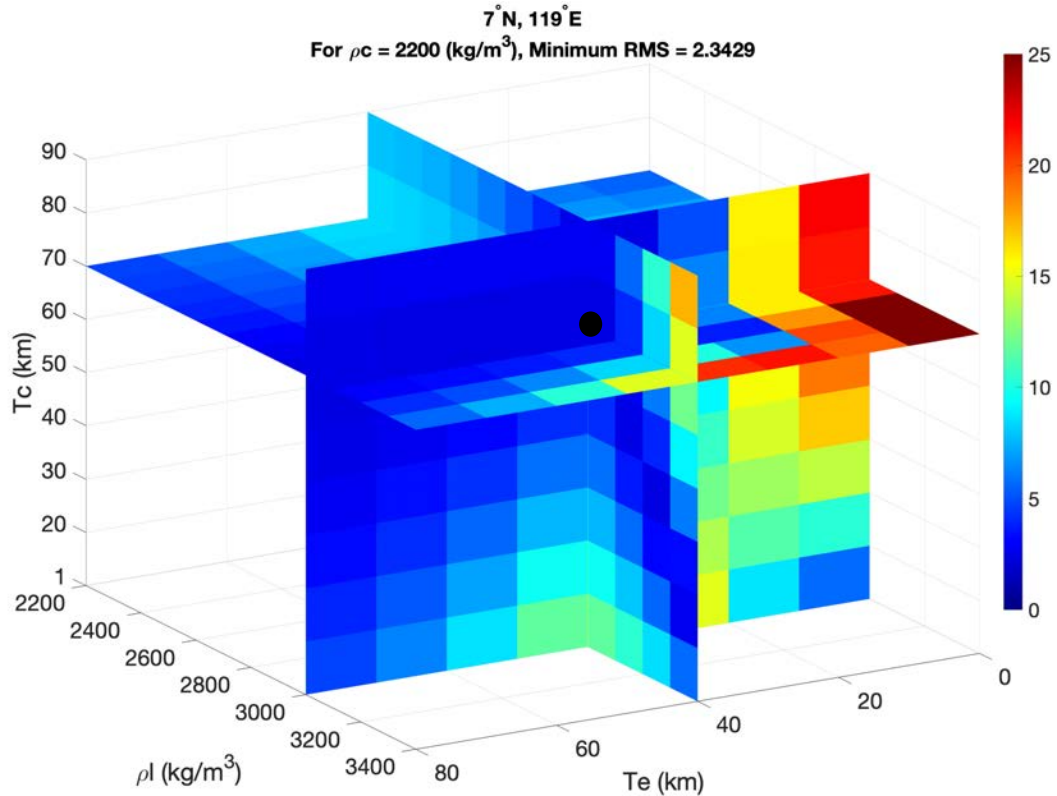


Figure 4.28 RMS space of crustal thickness, elastic thickness, and load density at location 7°N, 119°E. This plot uses a constant crustal density of 2200 kg/m^3 , which corresponds to the crustal density leading to the lowest RMS parameter combination (noted by the black circle, corresponding to Figure 4.27b).

The middle location tested along the center of the CDB is 2°S, 132°E. Figure 4.25 shows that the window encompasses portions of both the lowlands and the highlands in a relatively sharp transition. Degrees 30-60 were modeled with a minimum RMS of 3.56 mGal/km (Figure 4.29a) and theoretical curves are well within the observed error until an RMS of 15 mGal/km . With a maximum RMS of 422.32 mGal/km , 96.5% of the total RMS space can be excluded for poor fits outside of the error bars of observed and theoretical. The remaining 3.5% of the space holding acceptable solutions leads to

estimates of 40-80km for crustal thickness, 2200-2600kgm⁻³ for crustal density, 2200-3000kgm⁻³ for load density and 0-40km for elastic thickness.

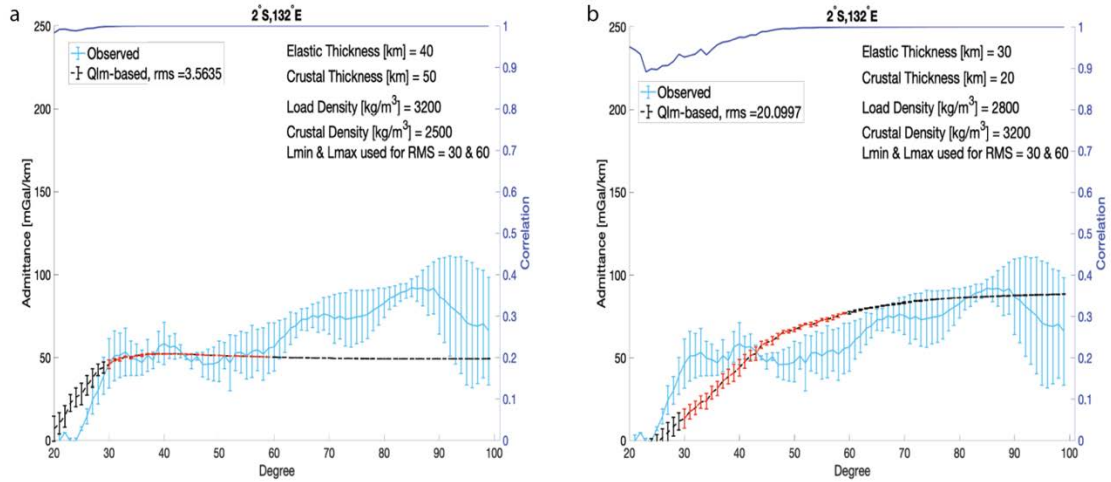


Figure 4.29 Observed (light blue) and theoretical (black) spectra for 2°S, 132°E. The modeled degree range is in red with theoretical correlation in dark blue. The parameter values used to produce each theoretical curve are given on the figure. (a) the minimum RMS case and (b) a case of an ill-fitting spectrum outside of the acceptable criteria range. Theoretical degree correlation is shown in dark blue. Vertical bars are standard error estimates on the spectra.

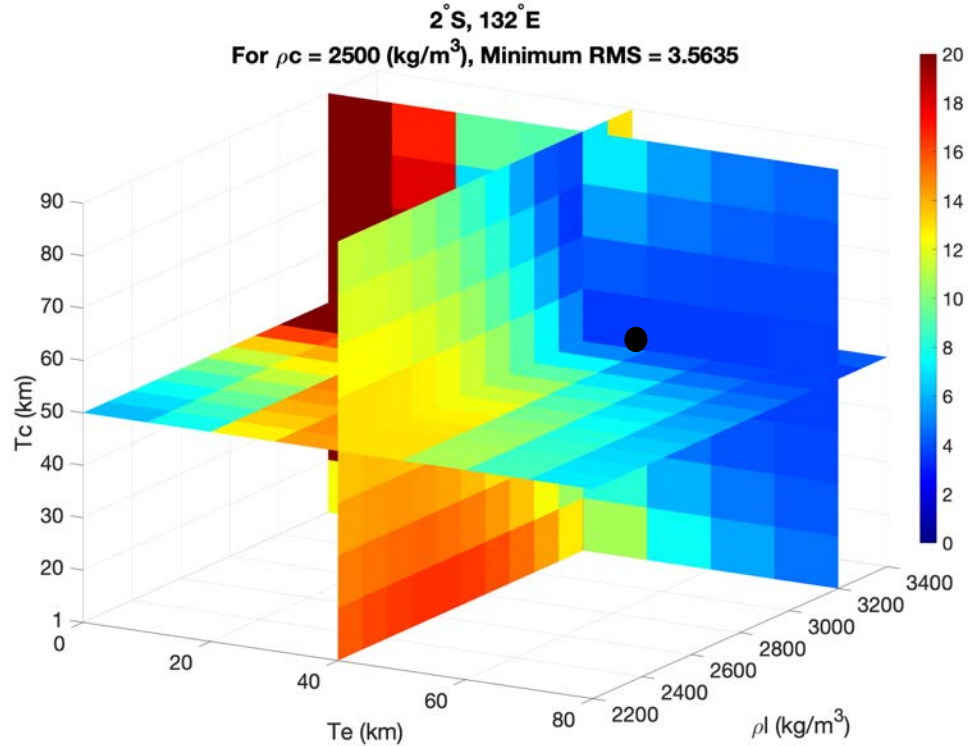


Figure 4.30 RMS space of crustal thickness, elastic thickness, and load density at location 2°S, 132°E. This plot uses a constant crustal density of 2500 kg/m^3 , which corresponds to the crustal density leading to the lowest RMS parameter combination (noted by the black circle, corresponding to Figure 4.29b).

The final spherical cap centered on the crustal dichotomy boundary is 9°S, 149°E.

The observed admittance was modeled for degrees 52 to 75. Figure 4.31b shows an attempt to model the inflection from degrees 30 – 50. Although the example does match degrees 30 – 50, there are no parameter combinations that could be considered near the observed admittance range for the rest of the spectrum. Additionally, all theoretical curves that match the inflection require an extremely high crustal thickness (90km) or crustal density (above 3200 kg/m^3) which are not reasonable for this region. Using degrees 52 to 75, theoretical curves fit within error bars of observed and theoretical from the minimum RMS of 3.19mGal/km until 25mGal/km. Thus, 5.3% of the total RMS space (maximum RMS of 477.79mGal/km) contains possible solutions. From this space,

it is estimated that crustal thickness is between 40-70km, crustal density is between 2200-2600kgm⁻³, load density is between 2200-3000kgm⁻³, and an elastic thickness between 0-40km.

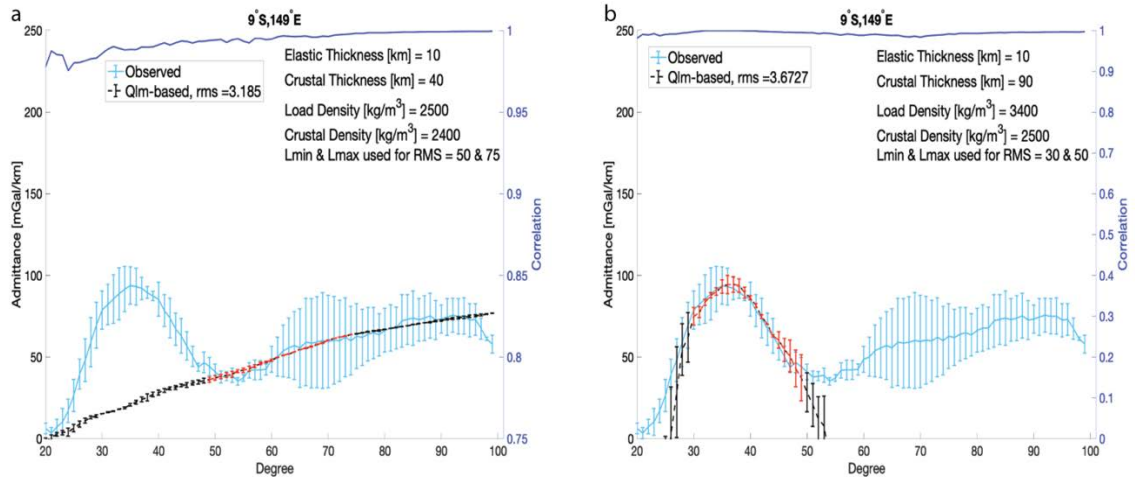


Figure 4.31 Observed (light blue) and theoretical (black) spectra for 9°S, 149°E. The modeled degree range is in red with theoretical correlation in dark blue. The parameter values used to produce each theoretical curve are given on the figure. (a) the minimum RMS case and (b) an attempt to model the peak from degrees 30 to 50, but does not fit observed admittance for the range of degrees 50 - 100. Theoretical degree correlation is shown in dark blue. Vertical bars are standard error estimates on the spectra.

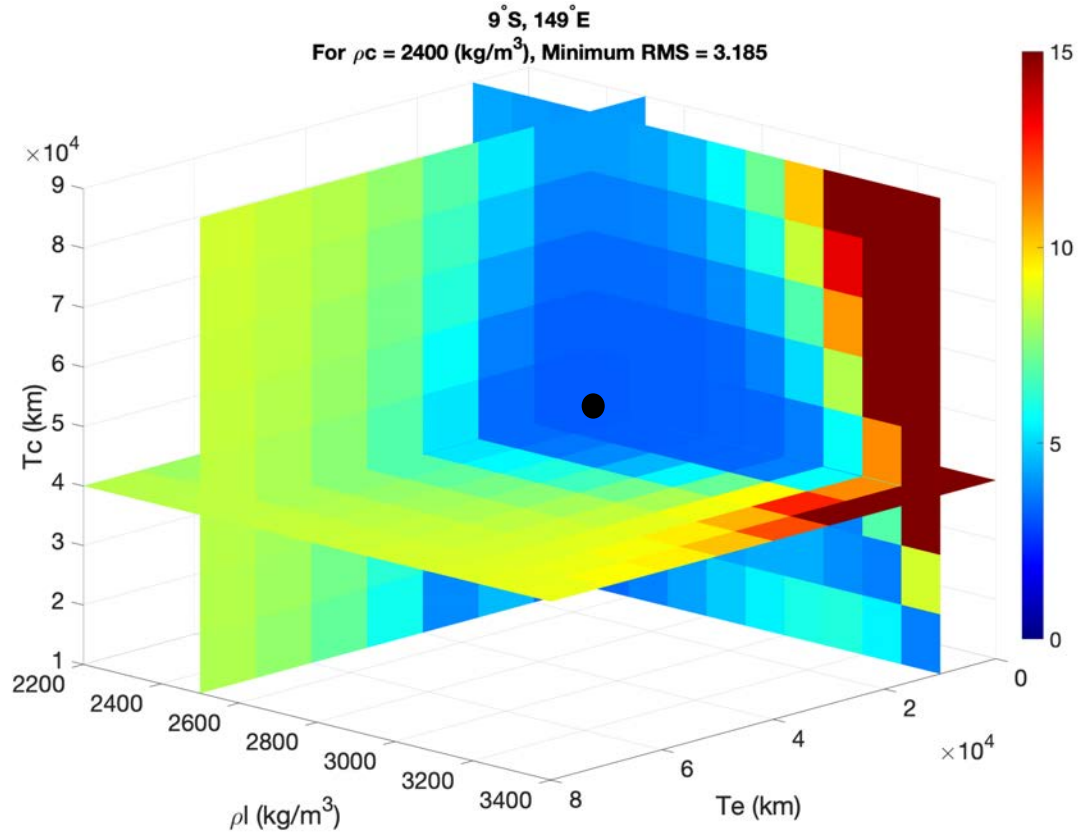


Figure 4.32 RMS space of crustal thickness, elastic thickness, and load density at location 9°S, 149°E. This plot uses a constant crustal density of 2400 kg/m^3 , which corresponds to the crustal density leading to the lowest RMS parameter combination (noted by the black circle, corresponding to Figure 4.31b).

4.3.2 Window of 30° spherical cap angular radius

In order to better understand the effect of the size of the spherical cap window on the observed and theoretical spectra, the angular radius of the spherical cap at location 32°S, 165°E was increased from 15° to 30°, shown in Figure 4.25. By doubling the window size, a larger amount of the topographic and gravitational signals, and hence lithospheric properties, are averaged together within the window. This location includes some of the lowlands (Figure 4.25) but is primarily comprised of highlands topography.

Two sets of spectral degree ranges were modeled for this location. To allow for more direct comparisons with the smaller window at the same location (Figure 4.9), spectral degrees 40 to 65 are modeled in Figure 4.32. Figure 4.32 shows the observed and modeled spectra with the increased window angular radius. From modeling degrees 40 – 65, the minimum RMS is 2.93mGal/km, reaching a maximum RMS of 452.05mGal/km. Theoretical admittance spectra do not meet the selection criteria by an RMS of 12mGal/km, which leads to all acceptable solutions being in 2.7% of the total RMS space.

Although degrees 40 – 65 allow for more direct comparison with Figure 4.9, degrees 30 – 55 (Figure 4.33) are more compatible with the mass sheet approximation and theoretical curves are more within the observed admittance errors. Using degrees 30 – 55, the minimum RMS achieved is 1.88mGal/km with a maximum RMS of 424.26mGal/km. Calculated admittance curves can be considered within the admittance error bars until an RMS of 10mGal/km (Figure 4.33).

From the increased window size and using degrees 40 - 65, the estimated crustal thickness is 50 – 80km, crustal density is between 2200-2600 kgm⁻³, load density is between 2200-3400kgm⁻³ and elastic thickness is between 10 – 50km. Using degrees 30 to 55, all parameter estimates produced the same results.

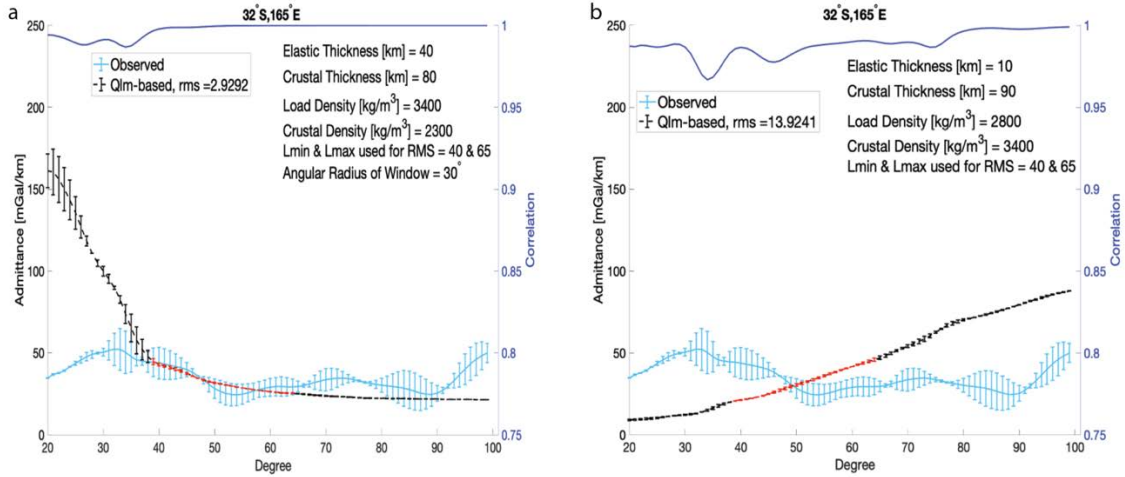


Figure 4.33 Observed (light blue) and theoretical (black) spectra for 32°S, 165°E using spectral degrees 40 to 65 and a 30° angular radius of the spherical cap window. The modeled degree range is in red with theoretical correlation in dark blue. The parameter values used to produce each theoretical curve are given on the figure. (a) the minimum RMS case and (b) a case of an ill-fitting spectrum outside of the acceptable criteria range. Theoretical degree correlation is shown in dark blue. Vertical bars are standard error estimates on the spectra.

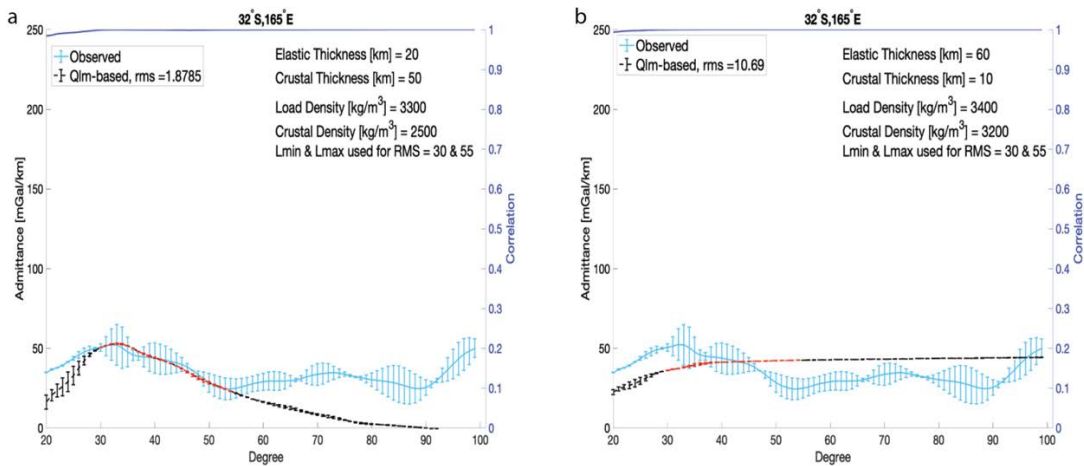


Figure 4.34 Observed (light blue) and theoretical (black) spectra for 32°S, 165°E using spectral degrees 30 to 55 and a 30° angular radius of the spherical cap window. The modeled degree range is in red with theoretical correlation in dark blue. The parameter values used to produce each theoretical curve are given on the figure. (a) the minimum RMS case and (b) a case of an ill-fitting spectrum outside of the acceptable criteria range. Theoretical degree correlation is shown in dark blue. Vertical bars are standard error estimates on the spectra.

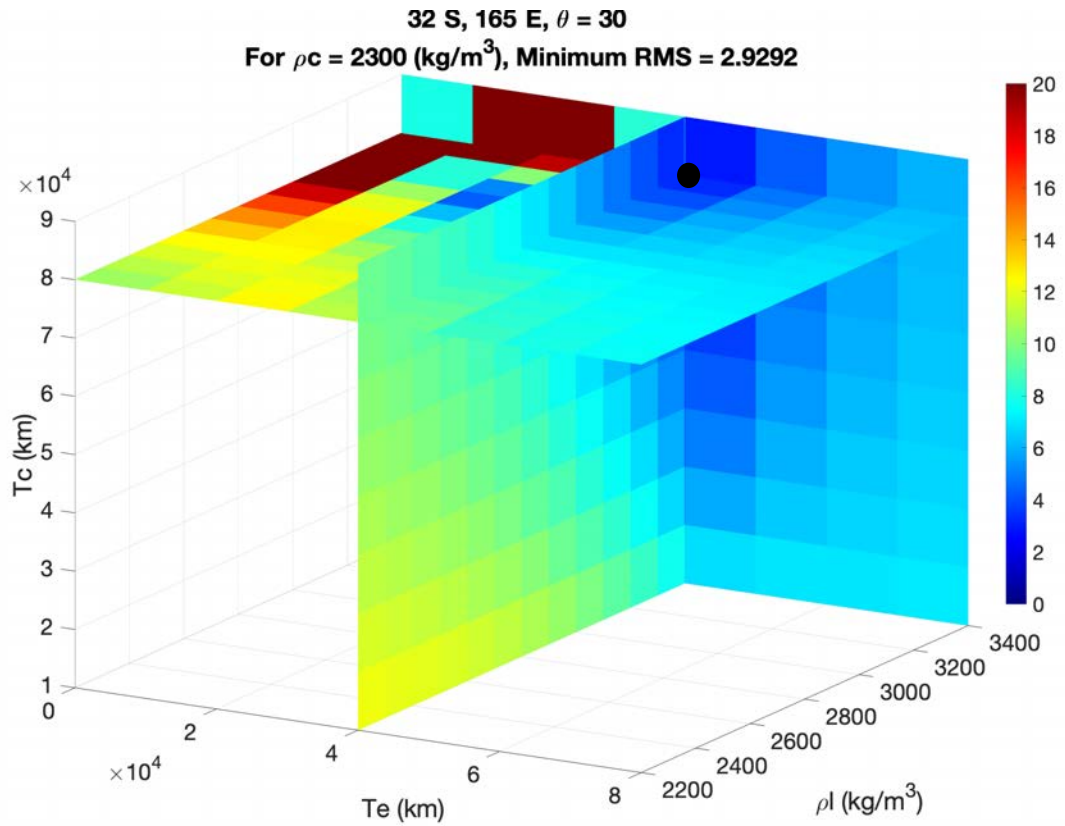


Figure 4.35 RMS space of crustal thickness, elastic thickness, and load density at location 32°S , 165°E for a 30° angular radius of the spherical cap window using spectral degrees 40 to 65. This plot uses a constant crustal density of 2300kgm^{-3} , which corresponds to the crustal density leading to the lowest RMS parameter combination (noted by the black circle, corresponding to Figure 4.32a).

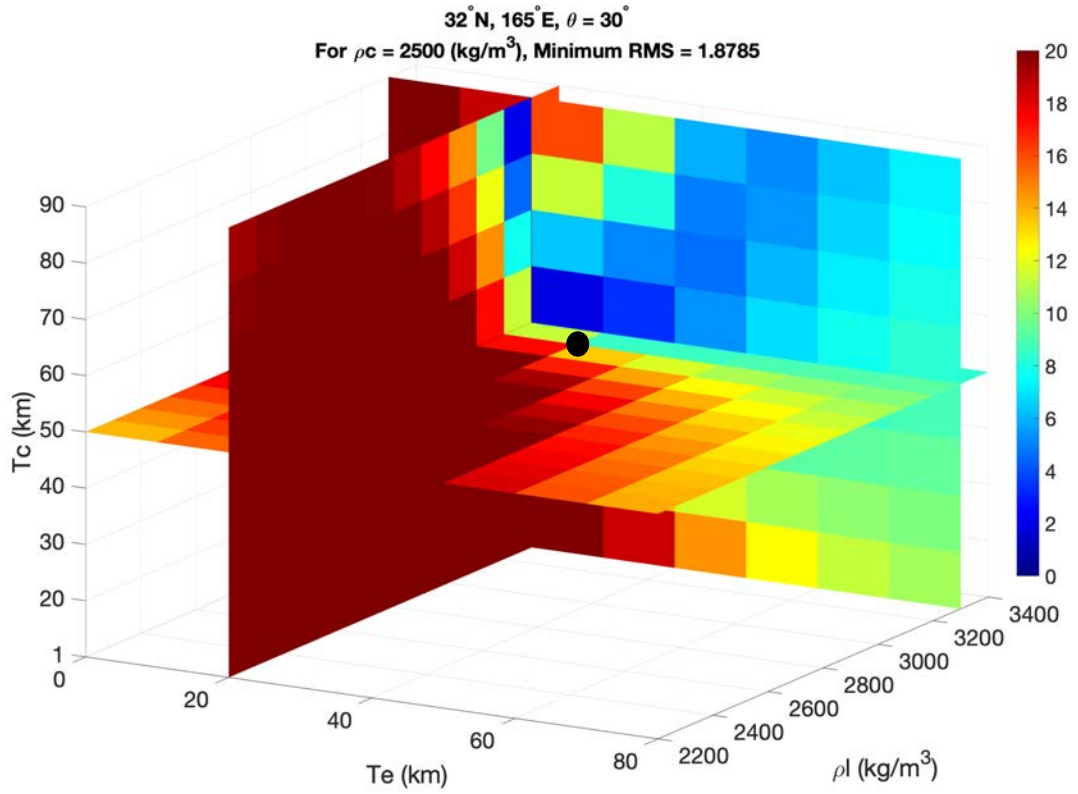


Figure 4.36 RMS space of crustal thickness, elastic thickness, and load density at location 32°S, 165°E for a 30° angular radius of the spherical cap window using spectral degrees 30 to 55. This plot uses a constant crustal density of 2500kgm⁻³, which corresponds to the crustal density leading to the lowest RMS parameter combination (noted by the black circle, corresponding to Figure 4.33a).

Table 4.2 Study locations on the CDB and their spectral range used, and acceptable parameter ranges of elastic thickness, load density, crustal thickness and crustal density estimates.

Latitude	Longitude	Spectral range	T_e [km]	ρ_l [kgm ⁻³]	T_c [km]	ρ_c [kgm ⁻³]
7°N	119°E	30-55	0-50	2200-3200	30-70	2200-2500
2°S	132°E	30-60	0-40	2200-3000	40-80	2200-2600
9°S	149°E	50-75	0-40	2200-3000	40-70	2200-2600
32°S	165°E	30-50	10-50	2200-3400	50-80	2200-2600
32°S	165°E	40-65	10-50	2200-3400	50-80	2200-2600

CHAPTER 5. DISCUSSION

5.1 Lithospheric properties across the CDB

Lithospheric properties such as crustal thickness and density have been shown to vary laterally on Mars, notably changing near the CDB (Genova et al., 2016; Goossens et al., 2017). Similarly, the parameter ranges found in this study show general trends in the transitions of crustal thickness, crustal density, load density and elastic thickness across the dichotomy boundary.

5.1.1 Crustal Thickness

Within the Northern Lowlands acceptable solution space, all parameter combinations have a crustal thickness greater than 10km and below 40km and the contours of constrained mean estimated crustal thickness for each window location are shown in Figure 5.1. Location 1°N, 200°E is an exception to this, as the exceptionally variable (for lowlands) topography may require a crustal thickness up to 50km. The middle two locations, 5°N, 149°E and 2°S, 185°E, are estimated to have a maximum elastic thickness of 30km. It is noted that no parameters could be estimated for 20°N, 98°E. Most estimates of elastic thickness on Mars are for specific physiographic features of interest, such as Tharsis, Olympus Mons, Elysium, several large and small volcanoes, Valles Marineris and polar deposits (McGovern et al., 2002; McKenzie et al., 2002; Hoogenboom and Smrekar, 2006; Grott and Breuer, 2010; Broquet and Wieczorek, 2019), and there are few studies that cover broad highlands and lowlands regions across the CDB. Moreover, crustal thickness is least resolved using the mass sheet approximation as seen in Figure 3.1. Hence, we further constrained them by their similarity to crustal thickness values from the models presented in Goossens et al. (2017).

Their first model, which applies a constant, standard crustal density of 2900kgm^{-3} , estimates crustal thicknesses between 10-30km for the Northern Lowlands side of the CDB in our study region. This is slightly lower than our 10-40km range. Estimates from their second model (using laterally varying crustal density) are between 20-30km, which is within, but better constrained than our range. The estimates of Genova et al. (2016) are slightly thicker, between 20-40km. A global crustal thickness map from Thor (2016) (constructed via subtracting the final (measurable) subsurface topography after flexure from the final surface topography after flexure) show very similar estimates of 10 – 40km in the Northern Lowlands region. Further, Ojha et al. (2014) explored a region of Elysium Planitia close to the InSight landing spot, which is near locations 12°N , 132°E and 5°N , 149°E of this study. Their method used a geophysical loading modeling including top and bottom loads to predict admittance by varying elastic parameters and lithospheric properties for window widths corresponding to an L_{win} of 15. They estimate a crustal thickness of 10-50km, which has a thicker maximum than our estimates of 10-30km for that region.

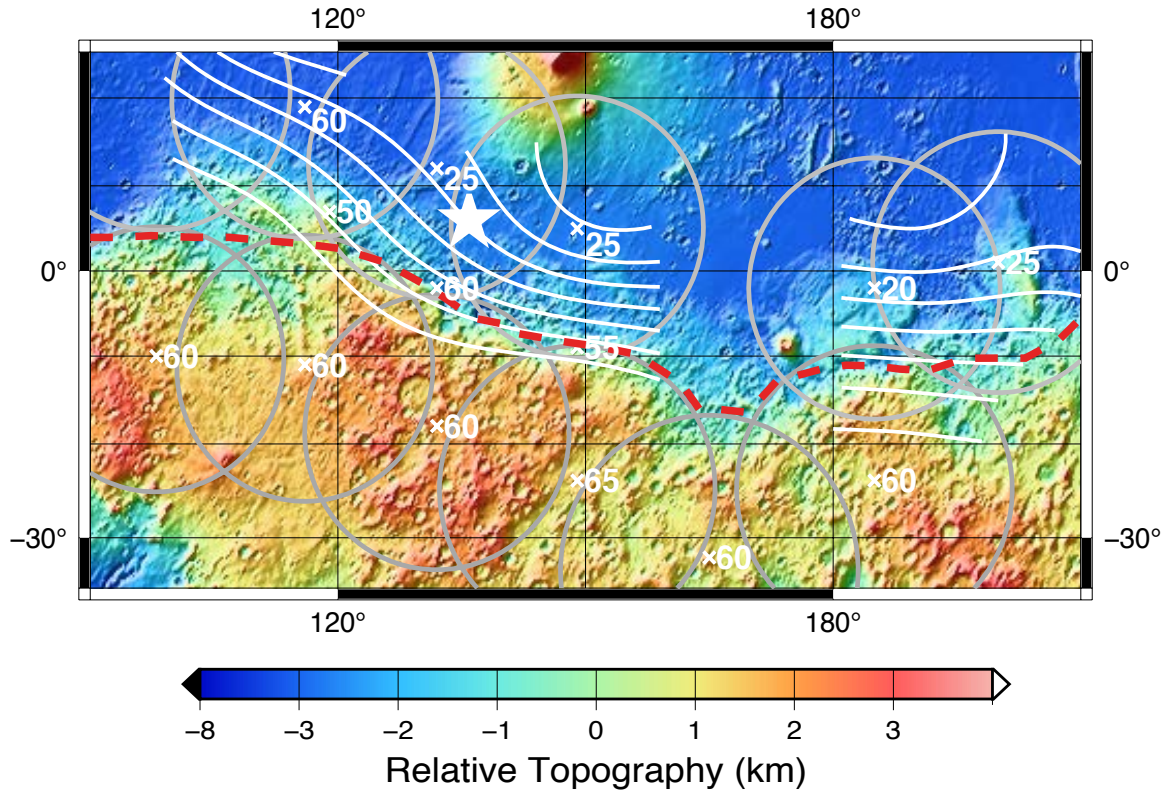


Figure 5.1 Contours (white lines) of the mean estimated crustal thickness for the range of possible estimates at each study location and spherical cap windows (gray circles) over MOLA topography. The mean value for each location is noted near an “x” at the center of the spherical cap. Spherical cap windows centered on the boundary are not shown, but their center and associated estimate are marked. The approximate CDB is shown by the red dashed line with InSight landing site marked by a white star. Contours that are greater than 10° away from an estimate are not connected and it is noted that drawing contours with this few points may be misleading.

The three locations centered directly on the dichotomy boundary for this study estimate crustal thicknesses between 30-70km, 40-80km and 40-70km (Figure 5.1). These minimum values (30 and 40km) are the same as our maximum estimates (30-40km) for Northern Lowlands locations near the middle of the study region. This suggests there might be overlap between the values of crustal thickness for the Northern Highlands and CDB, and thus a less sharp transition. The crustal thickness map from Genova et al. (2016) and the constant density model of Goossens et al. (2017) agree with

our ranges. These estimates have a slightly thicker maximum than those of Thor (2016), who calculates a crustal thickness between 40 – 60km directly on the zone of transition.

The mass-sheet approximation for admittance modeling produced higher crustal thickness estimates in the Southern Highlands than the Northern lowlands. The Southern Highlands have a minimum crustal thickness of 40km and a maximum of 80km from this study. This is a similar range to the estimates from windows directly on the CDB, which could suggest a less sharp transition from the boundary into the Southern Highlands (Figure 5.1). However, it is noted that the 10km resolution for crustal thickness creates large estimate ranges, thus there may be less overlap in crustal thickness in reality. Our estimates have a higher maximum value than predicted by the variable density model of Goossens et al. (2017), which are between 40-60km for this region. The constant density model, however, has values of 40 – 80km which match our predicted range. Genova et al. (2016) also predicts values within our range from 50-80km. A lower crustal thickness for the Southern Highlands region, between 50-60km, is estimated by Thor (2016).

Constraining the crustal thickness results via the estimates of other studies is necessary because the theoretical mass sheet-based admittance model does not well constrain crustal thickness (Figure 3.1), thus external information is needed. The crustal thickness estimates of Goossens et al. (2017) and Genova et al. (2016) are based on different crustal density assumptions and so cover a large range of possible crustal thicknesses. Thus, although the results are constrained using external information, they still cover a breadth of realistic possibilities.

5.1.2 Crustal Density

Similar to crustal thickness, there is a distinction between crustal density values in the lowlands and highlands. It is possible to constrain crustal density within a range of 200-500kgm⁻³ between the maximum and minimum estimate at most locations using the theoretical admittance and the models of Goossens et al. (2017). Northern Lowlands crustal density estimates commonly appear to range from 2300 kgm⁻³ to 2900kgm⁻³ with one high value of 3200kgm⁻³ at 2°S, 185°E, while the density range of the Southern Highlands crustal density is 2200-2500kgm⁻³. Directly along the transition zone, crustal density ranges from 2200-2600kgm⁻³. This is roughly consistent with the results of Goossens et al. (2017) density variation model, although they attain very high values of 3,000-3200kgm⁻³ beyond 10° northeast of the CDB over a very broad region of the lowlands (a region not investigated in this study). Other studies, such as Ojha et al. (2014), Genova et al. (2016), Thor (2016), the constant density model of Goossens et al. (2017) and Ding et al. (2019) used a constant crustal density of 2900kgm⁻³. Goossens et al. (2017) suggested higher porosity as the cause to explain low densities in the highlands. We further interpret this as impacts induced fracturing of Southern Highlands of Mars as impacts are ubiquitously observed in the highlands. These results and interpretations are also consistent with new InSight related investigations (Cottaar and Koelemeijer, 2021; Khan et al., 2021; Knapmeyer-Endrun et al., 2021).

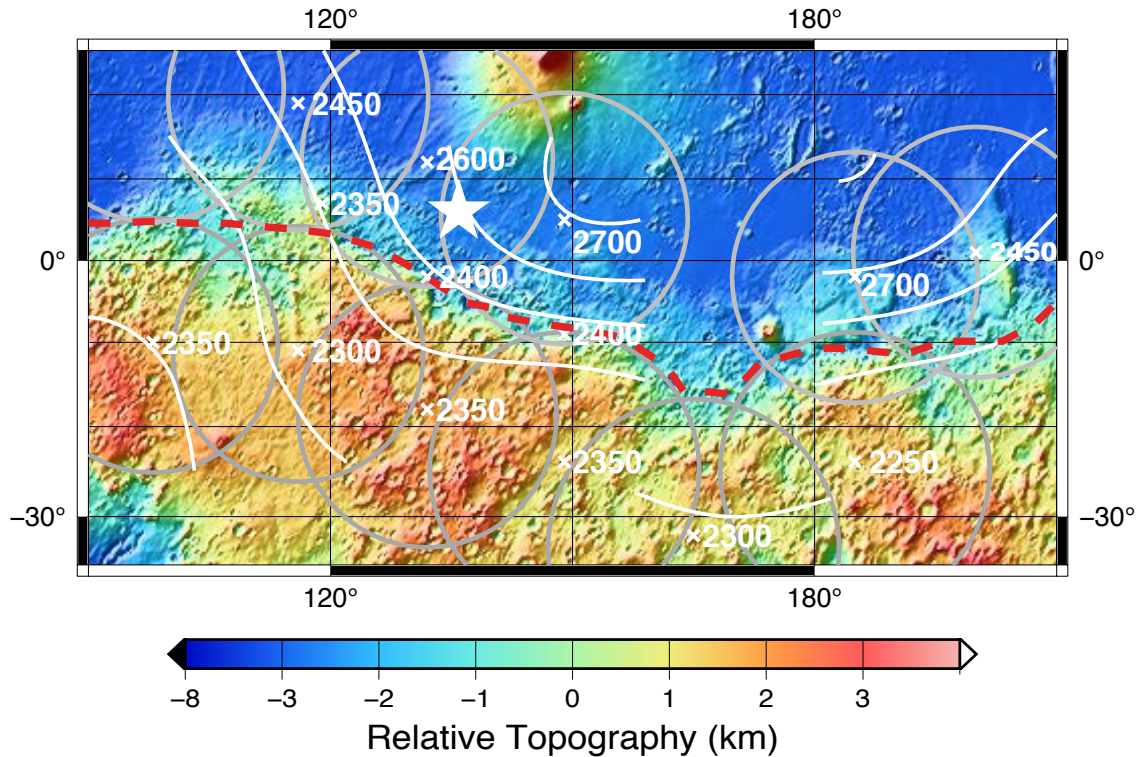


Figure 5.2 Contours (white lines) of the mean estimated crustal density (kgm^{-3}) for the range of possible estimates at each study location and spherical cap windows (gray circles) over MOLA topography. The mean value for each location is noted near an “x” at the center of the spherical cap. Spherical cap windows centered on the boundary are not shown, but their center and associated estimate are marked. The approximate CDB is shown by the red dashed line with InSight landing site marked by a white star. Contours that are greater than 10° away from an estimate are not connected and it is noted that drawing contours with this few points may be misleading.

In this study, most locations have substantial overlap between the range of crustal density estimates for windows located on opposing sides of the CDB. Locations 12°N , 132°E and 5°N , 149°E have a crustal density of $2300\text{-}2900\text{kgm}^{-3}$ and $2500\text{-}2900\text{kgm}^{-3}$, which overlap with the boundary estimate at 2°S , 132°E of $2200\text{-}2600\text{kgm}^{-3}$ leading into $2200\text{-}2500\text{kgm}^{-3}$ for both 18°S , 132°E and 24°S , 149°E . These ranges share many values, but the Northern Lowlands maximum is more dense than the Southern Highlands. The same is true for the region west of these locations. Parameter values for locations directly

on the boundary similarly overlap with the Southern Highlands results. Generally, this could imply that the crustal density change appears gradual (Figure 5.2) because of large window size needed for the study to consider the longest possible wavelengths. Better information on the nature of the change could be obtained by computing parameters from a densely sampled and possibly somewhat smaller windows. The laterally varying crustal density model of Goossens et al. (2017) shows a similar trend to Figure 5.2, where there is a substantial increase in crustal density north of the CDB, but no sharp transition.

5.1.3 Load Density

Most locations modeled in this study have a large range of load densities, as many values produced results well within the admittance error estimates. With many locations including all tested values (2200-3400kgm⁻³) in the acceptable solution space, a lateral trend is difficult to identify. Load density has been shown to vary on Mars, particularly for specific physiographic features such as volcanoes (Broquet and Wieczorek, 2019); however, the mass sheet approximation and RMS selection criteria may not be best suited for selecting load density for this region of the CDB.

5.1.4 Elastic Thickness

Elastic thickness is generally well-constrained, as the difference between the maximum and minimum estimate for most locations is 30km or less (two exceptions are 24°S, 149°E and 1°N,200°E which are each estimated to be 0-50km). Estimates are generally lower on the northern side of the boundary (less than 30km) than the southern. Some southern locations have a smaller range of thin elastic thickness (often 10 or 20km), but for others the spread of values is larger (up to 50km). On the contrary, the

northern regions, which all have a minimum of 0km (although due to the 10km modeling interval it could be up to 5km). On the boundary, estimates are between those of the Northern Lowlands and Southern Highlands values across the CDB. Again, this implies a gradual, but distinct, difference between northern and southern elastic thickness (the change appears gradual because of large window size needed for the study to have the longest possible wavelengths). Further, the contour patterns on Figures 5.3 and 5.4 reflect some overlap of Northern Lowlands and Southern Highlands estimates and do not suggest sharp transition. None of the acceptable solutions for either region required an elastic thickness greater than 50km.

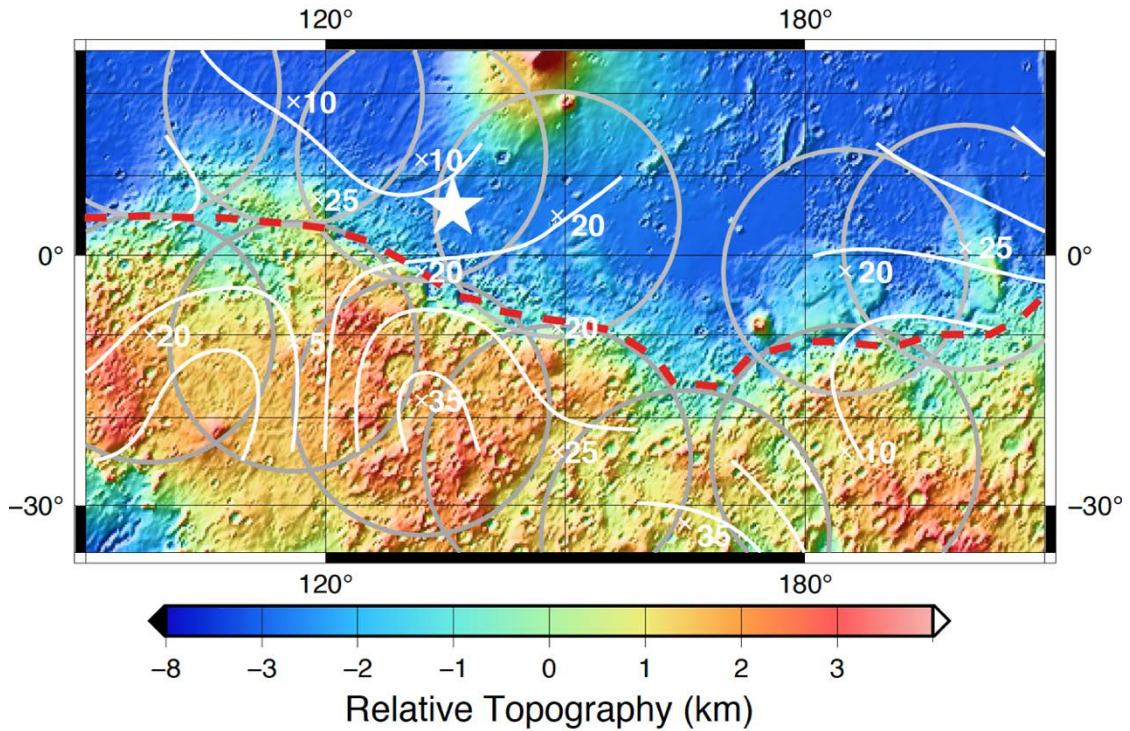


Figure 5.3 Contours (white lines) of the mean estimated elastic thickness for the range of possible estimates at each study location and spherical cap windows (gray circles) over MOLA topography. The mean value for each location is noted near an “x” at the center of the spherical cap. Spherical cap windows centered on the boundary are not shown, but their center and associated estimate are marked. The approximate CDB is shown by the red dashed line with InSight landing site marked by a white star. Contours that are greater than 10° away from an estimate are not connected and it is noted that drawing contours on this few points may be misleading.

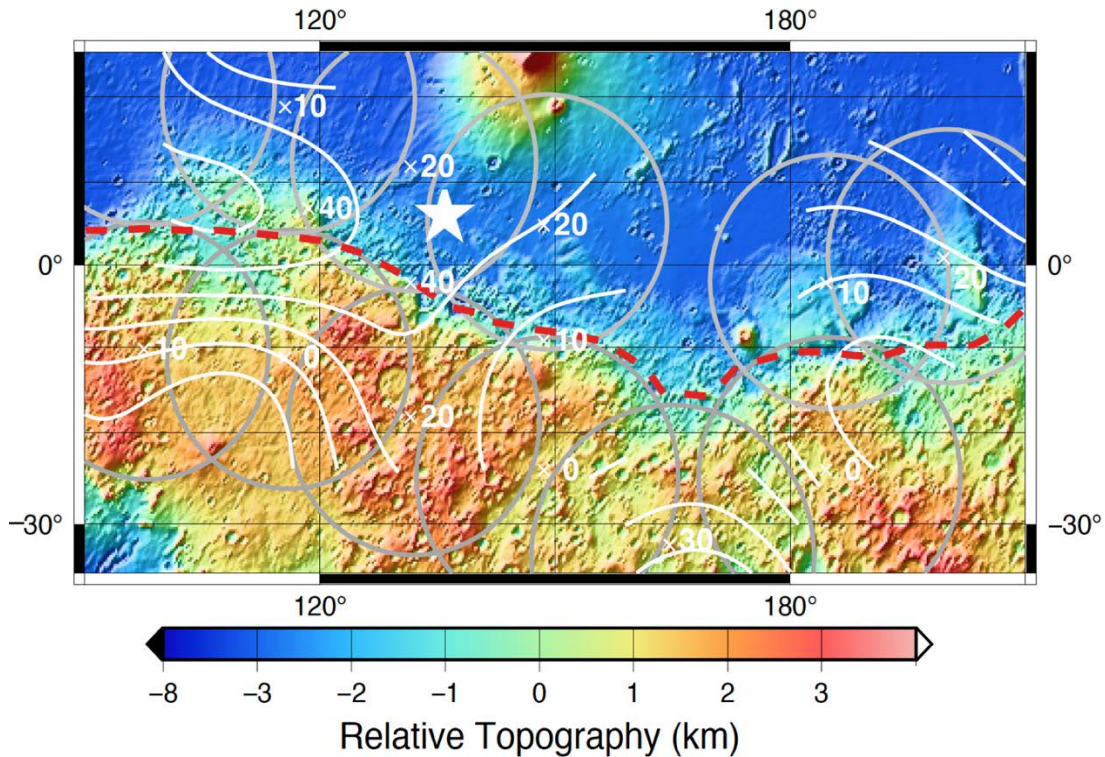


Figure 5.4 Contours (white lines) of the elastic thickness corresponding to the minimum RMS parameter combination for each study location and spherical cap windows (gray circles) over MOLA topography. The mean value for each location is noted near an “x” at the center of the spherical cap. Spherical cap windows centered on the boundary are not shown, but their center and associated estimate are marked. The approximate CDB is shown by the red dashed line with InSight landing site marked by a white star. Contours that are greater than 10° away from an estimate are not connected and it is noted that drawing contours on this few points may be misleading.

Northern Lowlands values on the western side of the study region (locations 12°N, 132°E and 5°N, 149°E) are estimated to be 0-20km, which increase in their range to 0-30km and 0-40km towards the eastern side (locations 2°S, 185°E and 1°N, 200°E, Figure 5.1). Several global elastic thickness maps computed from the multitaper analysis using SHTOOLS are provided by Thor (2016). His results using two tapers and an angular radius of the spherical cap window of 15° for our study region are estimated to be less than 50km. His estimates for some regions of the Northern Lowland are slightly

thicker (40-55km, and a few > 100 km) than the maximum 40km estimated in this study, whereas his Southern Highlands estimates (0-50km) are similar to those predicted here (0-50km). A global model of the elastic thickness at the time of topographic loading is provided by Kalousov et al. (2010). Their estimates were calculated by inverting the geoid and topography using a Gaussian window moved in steps of 5 degrees across the planet. For the region studied here, all values of elastic thickness are below 50km and unfortunately their elastic thickness values are difficult to estimate precisely because of their color scale. Similar to this study, there is an increase from near-zero km in the Northern Lowlands region to 25-40 in the Southern Highlands. The area of transition directly on the CDB is not sharply estimated and ranges from approximately 15-25km.

The results of predicting admittance by varying parameters for a region near the InSight landing spot (white star in Figure 3.2) in Ojha et al. (2014), who also estimated bottom-to-top crustal load ratio of 0.8, give elastic thickness between 10-30km. The locations from this study that are on the Northern Lowlands side of the CDB (12°N,132°E and 5°N,149°E) have estimates of 0-20km and 0-30km, which are very similar. Further, Ding et al. (2019) performed joint inversions of admittance and correlation to determine loading and flexural parameters of specific physiographic features. Their estimates for Elysium volcanic region and Utopia basin are near our Northern Lowlands study region and provide estimates of greater than 55km and less than 50km, respectively. Since we were not modeling Elysium Mons volcano specifically, but only the lowlands between the volcanic region and the CDB, their estimates are not directly comparable to ours. The region of Utopia basin that they modeled was closer to our Northern Lowlands locations and all of our estimates are well within their range of less than 50km.

Generally, it was found that in order to maintain a stable theoretical correlation between gravity and topography greater than 0.7, the estimated elastic thickness were always less than crustal thickness. Occasionally, a parameter combination with larger elastic thickness than crustal thickness could match the observed admittance signal within observed error, but this always produced an unreasonably low correlation estimate. This could imply that the strength of the lithosphere cannot exceed the thickness of the crust for that region; areas with low crustal thickness will generally have a lower elastic thickness and thus be more isostatically supported since zero elastic thickness suggests perfect Airy isostasy. With generally larger elastic thickness in the south, the lithosphere will not bend as much as the north in response to loading. It is noted that estimating parameter ranges from large and widely separated windows will automatically lead to less sharp transitions. To better understand how sharp the transition of lithospheric properties is, one could use a more densely sampled and possibly somewhat smaller windows as well as methods that detect crustal thickness and its variation better (in the mass sheet formulation it is the least sensitive parameter, see Figure 3.1).

From the parameter trends, one could interpret that this region of the Northern Lowlands could have previously had similar elastic thickness as the high values of neighboring Southern Highlands (0-50km). The large impacts that modified the northern hemisphere into the Northern Lowlands (Wilhelms and Squyres, 1984; Andrews-Hanna and Zuber, 2008) probably also increased the crustal density and reduced crustal thickness as well as effective elastic thickness (due to inelastic deformation/flow, Burov and Diament, 1995). The regions of thin elastic thickness in the Southern Highlands (11°S, 116°E and 24°S, 185°E) may be anomalous in terms of their mechanical properties

from changes in the lithosphere caused by other thermo-tectonic processes, ultimately freezing-in the mechanical strength of the lithosphere (e.g., Burov and Diament, 1995; Albert and Phillips, 2000).

5.2 Effect of increased window size

The angular radius of the spherical cap window determines the physical size of the resulting localized region and thus plays a major role in parameter estimation. Lithospheric properties could vary on a physically smaller scale than the window (i.e., less than 1,800km for a window with an angular radius of 15°); however, all values for a single property within the spherical cap are considered collectively. There is a tradeoff between using a window size that is small enough to capture spatial parameter changes and computational time/expense (as running models for many locations is time consuming and thus computationally very expensive).

Figures 4.9 and 4.33 show the effect of doubling the angular radius for a spherical cap centered at 32°S , 165°E . Although the observed signal resulting from the 30° angular radius (θ) window (Figure 4.33) is smoother than that of the smaller region (Figure 4.9), the larger window admittance was more difficult to reproduce theoretically. The minimum RMS for the $\theta = 15^\circ$ region is 1.98mGal/km, while the minimum for the $\theta = 30^\circ$ window is 2.93mGal/km. This is not an exceedingly large RMS difference, but the fits of acceptable theoretical solutions from the smaller window better represent the observed signal. In Figure 4.3, degrees 20 – 35 and 65 – 100 were difficult to fit within the observed error while matching degrees 40 - 65, and this was the case for all acceptable solutions.

Increasing the window size produced a larger range of acceptable parameter space, i.e., there are more parameter combinations that are within error bars of observed and theoretical and use reasonable values. Comparing Tables 4.1 and 4.2, crustal density, load density and elastic thickness are less well constrained for the large window. Thus, doubling the window size may still provide reasonable estimates, but it would be unlikely to capture the extent of variability along the CDB. Each location in Table 4.1 has different results, suggesting that lithospheric properties may change on a scale less than 1,800km. Such changes would be averaged together by a larger window, and thus be less representative of the physical situation. It would be reasonable to decrease window size along this region to see smaller scale changes; however, $\theta = 30^\circ$ might be beyond a useful window size.

5.3 Suitability of the mass-sheet approximation for admittance modeling

Results from the Southern Highlands side and directly on the CDB are generally better constrained, are more likely to fit within error bars of observed and theoretical and have lower minimum RMS than those on the northern side of the boundary. Thus, the mass sheet approximation may be better suited for estimating admittances from the southern region of the planet.

Observed spectra in the northern lowlands often have sharply changing slopes, which could be due to noise. The observed admittance signal for the window over 20°N , 98°E could not be matched by the mass-sheet approximation (Figure 4.13). This region has extremely flat topography (Figure 3.2); however, it encompasses a large positive free-air gravitational anomaly at the center of Isidis crater, large negative anomalies near the

crater rim and relatively large anomalies throughout the rest of the region (Figure 1.2). It has been shown by Hoogenboom and Smrekar (2006) that areas of low topography and large free air gravitational anomaly have noisy admittance signals. This is understandable as admittance involves division of free-air gravity by topography and noise in gravity will increase noise in the observed admittance. In general, for the Bouguer slab or mass-sheet approximation to be valid one needs sufficient variation of elevation and the elevation variation in many flat-lying northern lowland locations may not be sufficient. These factors could be contributing to the difficulty of modeling a number of the northern regions, including 20°N, 98°E. Locations 19°N, 116°E, 12°N, 132°E, and 5°N, 149°E also have large gravitational anomalies from sources further north, near the CDB and Elysium volcano (Figure 1.2). These locations could be estimated (although theoretical curves do not fit within error bars of observed and theoretical as well as many of the other northern lowland locations, Figures 4.14-4.19) because though low-lying, they encompass slightly more topographic variation. The two Northern Lowlands locations that were best estimated by the mass-sheet approximation (2°S, 185°E and 1°N, 200°E) have substantially higher elevation topographic features with the large free air gravitational anomalies (Figure 3.2 and Figure 1.2). Southern locations do not include as large free air gravitational anomalies and have much greater topographic variation (Figure 3.2 and Figure 1.2).

Another source of noise contributing to the difficulty of modeling some windowed regions is the localization process. When localizing the admittance signal, a spectral bandwidth (L_{win}) is selected so that the spectra power concentration is greater than 99% at the center of the window (Broquet and Wiczorek, 2019). Towards the edges

of the window, however, data weights decrease (zeroing out beyond the window). Because of this, the edges of the windows have less power and therefore do not contribute meaningfully to the solution. This is one of the reasons windows much smaller than 15° radius would not be very effective in estimating lithospheric properties with the mass-sheet approximation (which appears suitable for regions without distinct physiographic features based on this study).

A further consideration for the suitability of this method is the computational expense of constructing and localizing the theoretical gravitational potential for a large parameter space. Computational expense in geophysical modeling is directly related to resolution; increasing the number of windows to be modeled or using a finer scale of possible values will substantially increase the amount of time and storage needed to run the calculations. When running all parts of the computation on a laptop computer (MacBook Pro, 2019), one window location took approximately two weeks to fully compute theoretical admittances for the full parameter space. This was significantly reduced to three to four days per window by using the Lipsomb Compute Cluster (LCC) at University of Kentucky. However, the LCC timeframe can often be increased due to downed, drained or busy nodes being unavailable. Increasing the resolution of this study by decreasing window size (thus investigating more locations to cover the same spatial area) or using a finer parameter space (i.e., decreasing crustal and elastic thickness steps from 10km to 1km and / or decreasing crustal and load density steps from 100kgm^{-3} to 50kgm^{-3}) would create further computational demand. Thus, although increasing resolution would help better constrain parameter estimations, there is an increase in computation time associated with that.

The first computational step in creating the localized theoretical admittance is constructing the Q_1 transfer function (Eqn. 3.2) and calculating global theoretical gravitational potential. In this step, the entire parameter space is examined (i.e., all crustal density, crustal thickness, load density and elastic thickness values to be tested). Using the parameter space tested here, this creates 13,689 unique global theoretical signals (without subsurface loads) and typically required 2-4 days to run on the LCC. Running this initial step for all locations was time consuming. However, we only recently realized that the global spherical harmonic gravitational coefficients for each parameter combination are the same regardless of its location and the coefficients only become different after localization to particular geographic location. Therefore, it is not necessary to re-construct the global theoretical gravitational signal before proceeding to calculate the localized admittance for each window; one could run the global theoretical gravitational computation once and use the same theoretical spherical harmonic gravitational coefficients in all localized admittance calculations. This step would optimize the method and save potentially weeks of computational time, allowing computation of many more locations and a finer parameter space.

5.4 Inclusion of subsurface loads

One major difference between the mass-sheet approximation as used here and that of Broquet and Wieczorek (2019) is the inclusion of loading ratios (the ratio of the amount of surface and subsurface loading) for in phase loads. Although there are methods of including arbitrary phase differences between surface and internal loads (an extension of the model used by Forsyth, 1985, presented in Wieczorek, 2007), all loads are assumed in-phase in Broquet and Wieczorek (2019). In-phase loading ratio is useful for geologic

situations such as volcanoes where there might be substantial internal material influencing the observed admittance. However, here we assume that in and around CDB, away from specific physiographic features, there is minimal in-phase internal loading, if any, and the loads are completely out-of-phase (corresponding to a loading ratio of 0). This assumption is also borne out by Broquet and Wieczorek (2019) cases of broad and small volcanoes where their derived load ratio is close to zero.

Many of the observed admittances have peaks in the signal that are difficult to estimate by the mass-sheet approximation, such as Figure 4.13. Similar features are present in some of the observed admittance curves from volcanoes modeled by Broquet and Wieczorek (2019). They are able to match theoretical curves to the inflections within observed error for a range of degrees using finite amplitude topographic loads and associated depressed lithosphere. For large volcanoes, these peaks could be related to internal loads that are in phase with topography. If there are internal loads located within our study windows, then the assumption of a zero load ratio would not account for and thus not correctly estimate them. The mass-sheet approximations for locations with significant peaks in observed admittance signals might be improved by including loading ratios for in-phase internal loads. By this logic, most locations south of the CDB may not be as affected by internal loads; the observed admittance spectra at these locations are generally smooth or have less significant inflections that are well matched by theoretical curves using the mass sheet approximation for surface loading only. This would be best tested by including a range of loading ratios in the mass sheet approximation calculation and comparing the fits to those presented here. However, this would increase

computational demand substantially as the number of unique theoretical gravitational signals would be multiplied by the number of load ratios tested.

CHAPTER 6. CONCLUSION

As one of the most distinctive global crustal features of Mars, the Crustal Dichotomy Boundary (CDB) is a key element for understanding the thermal evolution and tectonic history of Mars. Knowledge of how lithospheric and rheological properties vary across the CDB can improve understanding of the formation of the dichotomy and thus differences in crustal evolution across it. Crustal thickness, crustal density and load density are important parameters for this, and elastic thickness is a key indication of the thermal and rheological conditions at the time of CDB formation.

A number of spectral admittance modeling studies on Mars have estimated the elastic thickness of specific physiographic features of interest (e.g., McGovern et al., 2002; McKenzie et al., 2002; Grott and Wieczorek, 2012; Ojha et al., 2014; Broquet and Wieczorek, 2019; Ding et al., 2019), or explored global variations (Kalousov et al., 2010, and Thor, 2016). However, such studies have not used admittance modeling to explore regional scale lithospheric properties specifically across the CDB. Additionally, we include laterally varying estimates of lithospheric properties including crustal thickness, crustal density and load density. Similar admittance modeling for elastic thickness, load density and crustal density of large and small volcanoes was recently done by Broquet and Wieczorek (2019); we employ a simplified approach of their method by using the mass-sheet approximation (which is appropriate for broad regions without specific physiographic features) without subsurface loading. Additionally, we considered non-uniqueness in the potential fields by not solely relying on the minimum RMS and visually examined a large range of admittance fits to identify acceptable parameters within the noise estimates and thus have compiled ranges of feasible estimates.

There is a distinct difference in crustal properties across this region of the CDB, but our results do not suggest a sharp transition. Crustal density is likely higher in the Northern Lowlands (a maximum estimate of 3200kgm^{-3}) than the Southern Highlands (a maximum estimate of 2500kgm^{-3}). The low crustal densities of the highlands are attributed to fracture porosity caused by a large number of impacts. No elastic thickness estimates were over 50km, with many ranged between 0-30km for the Northern Lowlands and between 0-50km for the Southern Highlands. In most regions, estimates across the boundary show a larger elastic estimate in the highlands than the lowlands with overlapping or intermediate values on the boundary. This could be interpreted as a transition between properties across the boundary; however, we have only a few determinations in the region of the boundary southwest of the Elysium Mons.

This region of the Northern Lowlands could have originally had similar elastic thickness as the high values of neighboring Southern Highlands, and the large impacts that re-molded the northern hemisphere into the Northern Lowlands (Wilhelms and Squyres, 1984; Andrews-Hanna and Zuber, 2008) also may have increased the crustal density and reduced elastic thickness. A couple of the estimates of the elastic thickness in the Southern Highland are much thinner than their surrounding highlands and lowlands estimates (Figures 5.3 and 5.4). These small values could partly be due to other local thermo-tectonic processes such as freezing-in of the mechanical strength of the lithosphere at the time of the formation of these regions or a later major geotectonic activity in the regions.

In general, the mass-sheet approximation is useful for making first order approximations of crustal density and elastic thickness for this region of the CDB as long

as there is sufficient topographic variation in the analysis window. However, load density was generally not well-constrained and thus the mass-sheet may not be well-suited for estimating load density across the CDB or similar regions with broad variations. Studies with finer spatial and parameter space resolution would further clarify the transition of lithospheric properties across the CDB and it is worth continuing the study over the rest of the planet despite the time-consuming nature of selecting feasible solutions within the error bars of observed and theoretical admittance. Inclusion of subsurface loads and random loading phase differences could improve estimates made by this model by better fitting inflections in the observed admittance variation.

APPENDIX A.

Examples of spectra that are acceptable within error estimates of both observed and theoretical admittance curves

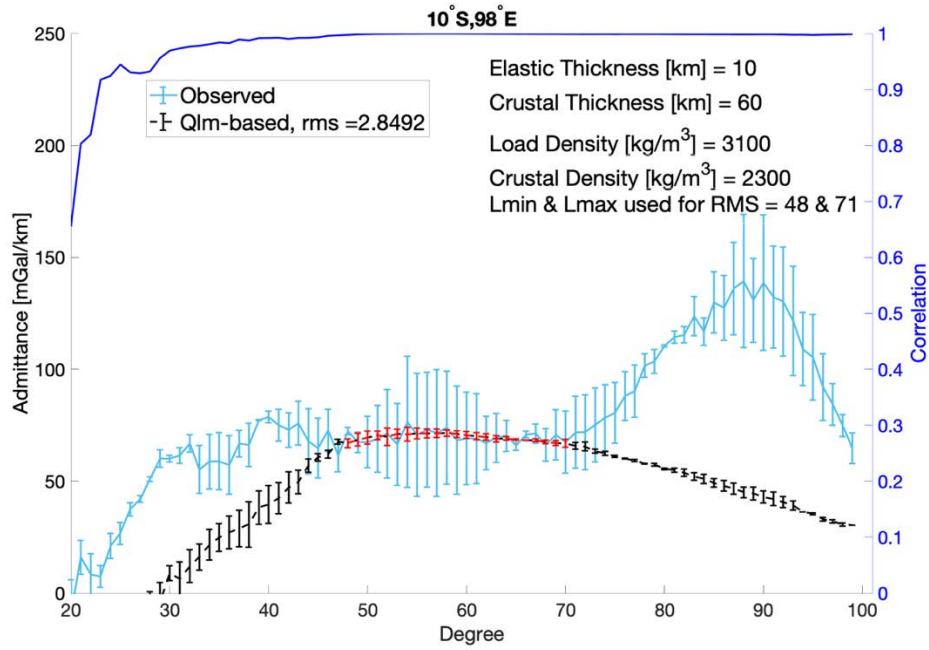


Figure A. 1 An observed (light blue) and theoretical (black) spectra for 10°S, 98°E. The modeled degree range is in red with theoretical correlation in dark blue. The theoretical signal is from a parameter combination producing an RMS close to the minimum RMS. The parameter values used to produce each theoretical curve are given on the figure. Theoretical degree correlation is shown in dark blue. Vertical bars are standard error estimates on the spectra.

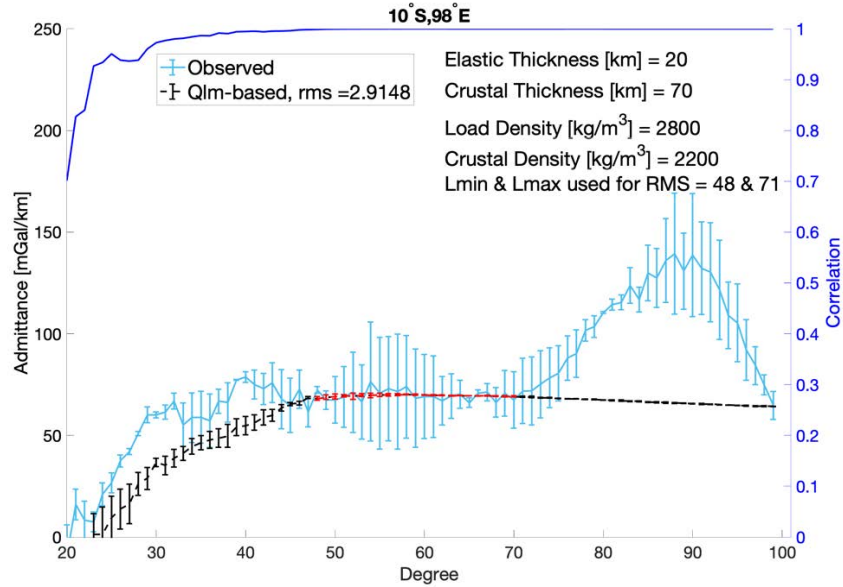


Figure A. 2 An observed (light blue) and theoretical (black) spectra for 10°S, 98°E. The modeled degree range is in red with theoretical correlation in dark blue. The theoretical signal is from a parameter combination producing an RMS close to the minimum RMS. The parameter values used to produce each theoretical curve are given on the figure. Theoretical degree correlation is shown in dark blue. Vertical bars are standard error estimates on the spectra.

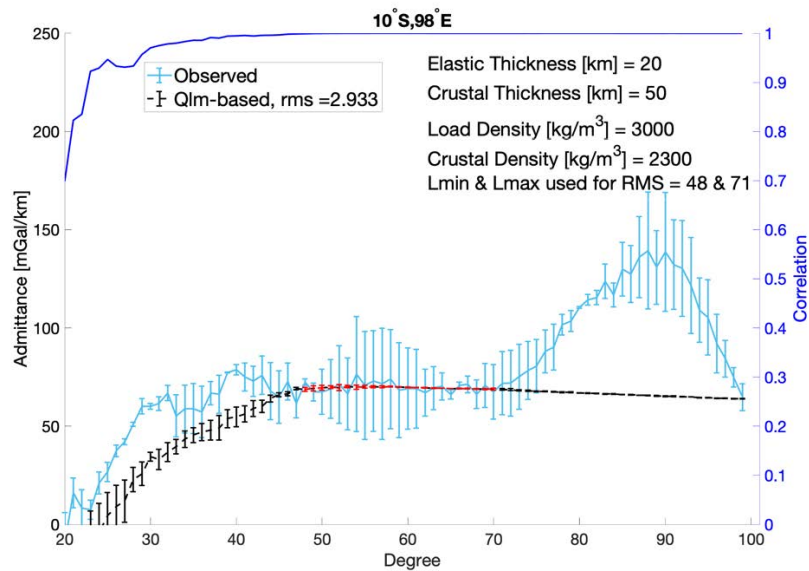


Figure A. 3 An observed (light blue) and theoretical (black) spectra for 10°S, 98°E. The modeled degree range is in red with theoretical correlation in dark blue. The theoretical signal is from a parameter combination producing an RMS close to the minimum RMS. The parameter values used to produce each theoretical curve are given on the figure. Theoretical degree correlation is shown in dark blue. Vertical bars are standard error estimates on the spectra.

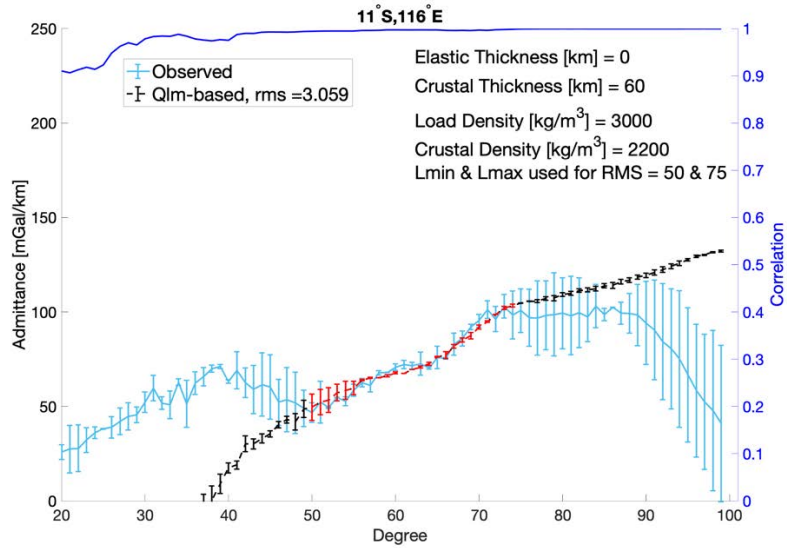


Figure A. 4 An observed (light blue) and theoretical (black) spectra for 11°S, 116°E. The modeled degree range is in red with theoretical correlation in dark blue. The theoretical signal is from a parameter combination producing an RMS close to the minimum RMS. The parameter values used to produce each theoretical curve are given on the figure. Theoretical degree correlation is shown in dark blue. Vertical bars are standard error estimates on the spectra.

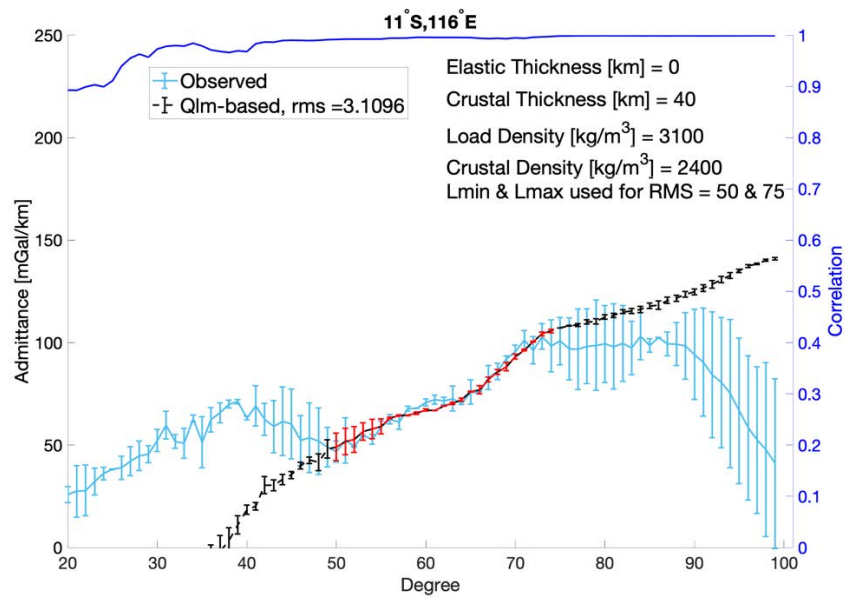


Figure A. 5 An observed (light blue) and theoretical (black) spectra for 11°S, 116°E. The modeled degree range is in red with theoretical correlation in dark blue. The theoretical signal is from a parameter combination producing an RMS close to the minimum RMS. The parameter values used to produce each theoretical curve are given on the figure. Theoretical degree correlation is shown in dark blue. Vertical bars are standard error estimates on the spectra.

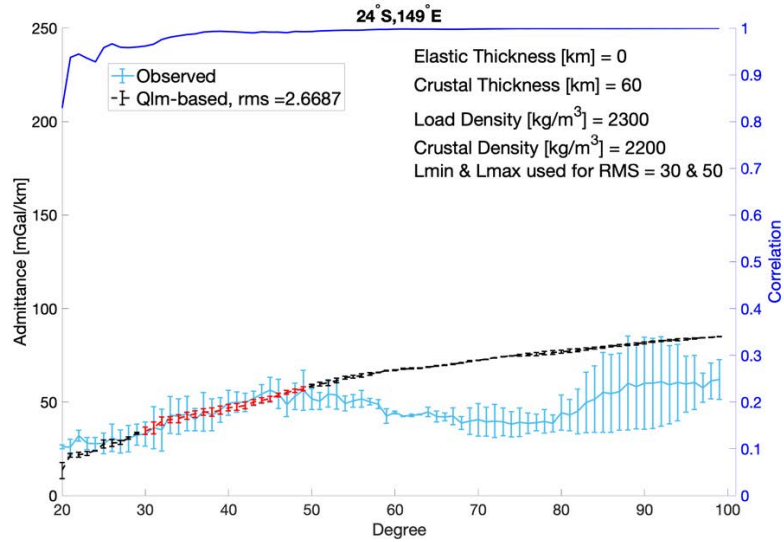


Figure A. 6 An observed (light blue) and theoretical (black) spectra for 24°S, 149°E. The modeled degree range is in red with theoretical correlation in dark blue. The theoretical signal is from a parameter combination producing an RMS close to the minimum RMS. The parameter values used to produce each theoretical curve are given on the figure. Theoretical degree correlation is shown in dark blue. Vertical bars are standard error estimates on the spectra.

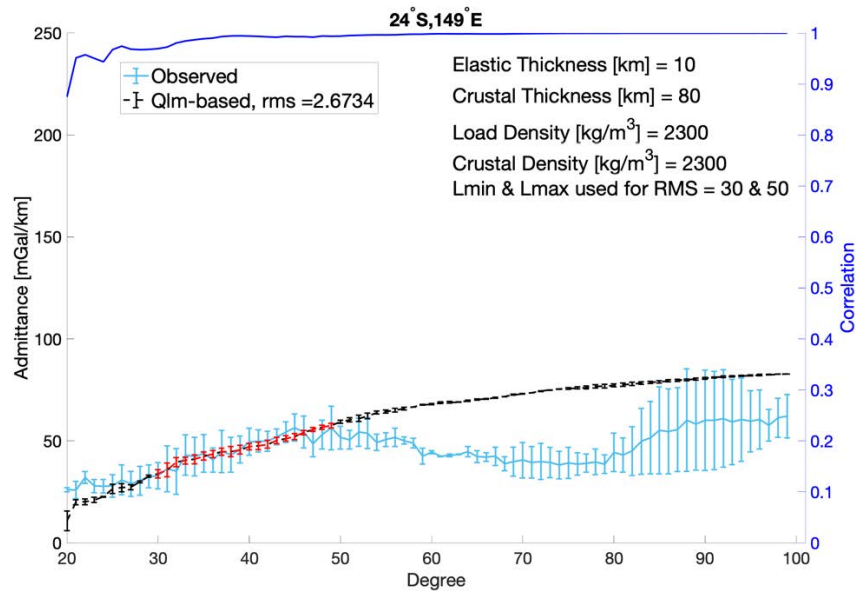


Figure A. 7 An observed (light blue) and theoretical (black) spectra for 24°S, 149°E. The modeled degree range is in red with theoretical correlation in dark blue. The theoretical signal is from a parameter combination producing an RMS close to the minimum RMS. The parameter values used to produce each theoretical curve are given on the figure. Theoretical degree correlation is shown in dark blue. Vertical bars are standard error estimates on the spectra.

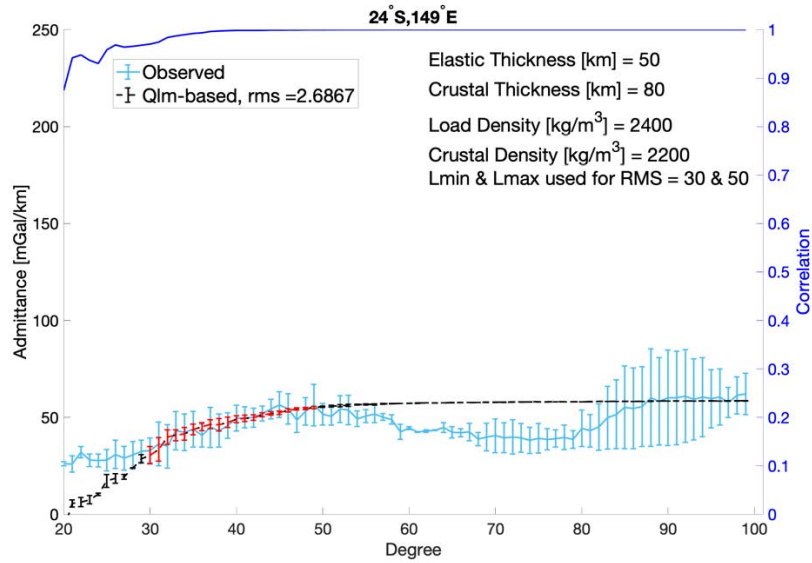


Figure A. 8 An observed (light blue) and theoretical (black) spectra for 24°S, 149°E. The modeled degree range is in red with theoretical correlation in dark blue. The theoretical signal is from a parameter combination producing an RMS close to the minimum RMS. The parameter values used to produce each theoretical curve are given on the figure. Theoretical degree correlation is shown in dark blue. Vertical bars are standard error estimates on the spectra.

APPENDIX B

A schematic diagram of spherical cap window and Airy and flexural isostasy.

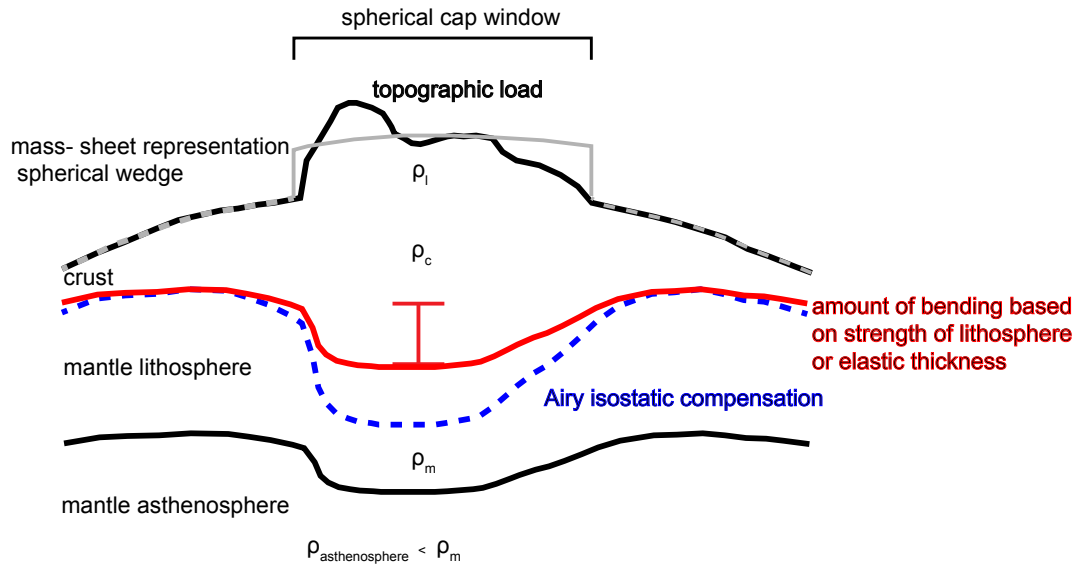


Figure B. 1 Conceptual representation of the Bouguer mass-sheet approximation method. The mass-sheet approximation does not represent short wavelength irregularities in local topography (black) but is using a Bouguer slab (grey) to approximate the topographic signal within the spherical cap window (shown at top of figure).

A lithosphere with little elastic strength (blue dashed line) would bend substantially in response to the topographic load as it is primarily supported by Airy isostasy. However, if the lithosphere has elastic strength, the amount of Airy isostatic compensation, and thus bending, is reduced (red line) and more spread out. The elastic thickness of this lithosphere is shown by the red I. The mass-sheet approximation can still be used to distinguish the amount of lithospheric bending in the absence of internal loads.

References

- Acuña, M. H., et al. (1999), Global Distribution of Crustal Magnetization Discovered by the Mars Global Surveyor MAG/ER Experiment, *Science*, 284, 790-793.
- Aharonson, O., Zuber, M. T., and Rothman, D. H. (2001), Statistics of Mars' topography from the Mars orbiter laser altimeter: slopes, correlations, and physical models, *Journal of Geophysical Research*, 109, 723-735.
- Albert, R. A., and Phillips, R. (2000), Paleoflexure, *Geophysical Research Letters*, 27, 23852388, doi:<https://doi.org/10.1029/2000GL011816>.
- Andrews-Hanna, J. C., and Zuber, M. T. (2008), The Borealis basin and the origin of the martian crustal dichotomy, *Nature*, 453, 1212-1215.
- Banks, R. J., Francis, S. C., and Hipkin, F. G. (2000), Effects of loads in the upper crust on estimates of the elastic thickness of the lithosphere, *Geophysical Journal International*, 145, 291-299.
- Belleguic, V., Lognonné, P., and Wieczorek, M. (2005), Constraints on the Martian lithosphere from gravity and topography data, *Journal of Geophysical Research: Planets*, 110, doi:10.1029/2005JE002437.
- Broquet, A., and Wieczorek, M. (2019), The Gravitational Signature of Martian Volcanoes, *Journal of Geophysical Research: Planets*, 2045-2086, doi:10.1029/2019je005959.
- Burov, E., and Diament, M. (1995), The effective elastic thickness (T_e) of continental lithosphere: What does it really mean?, *Journal of Geophysical Research*, 100, 3905-3927.
- Carr, M. H., and Head, J. W. (2010), Geologic History of Mars, *Earth and Planetary Science Letters*, 294, 185-203, doi:10.1016/j.epsl.2009.06.042.
- Cottaar, S., and Koelemeijer, P. (2021), The interior of Mars revealed, *Science*, 373(6553), 388-389.
- Ding, M., Lin, J., Gu, C., Huang, Q., and Zuber, M. T. (2019), Variations in Martian Lithospheric Strength Based on Gravity/Topography Analysis, *American Geophysical Union*, 124, doi:10.1029/2019JE005937.
- Forsyth, D. W. (1985), Subsurface Loading and Estimates of the Flexural Rigidity of Continental Lithosphere, *Journal of Geophysical Research*, 90, 12623-12632.
- Frey, H. V. (2006), Impact constraints on the age and origin of the lowlands of Mars, *Geophysics Research Letters* 33, doi:10.1029/2005GL024484.
- Genova, A., Goossens, S., Lemoine, F. G., Mazarico, E., Neumann, G. A., Smith, D. E., and Zuber, M. (2016), Seasonal and static gravity field of Mars from MGS, Mars Odyssey and MRO radio science., *Icarus*, 272, 228-245.
- Goossens, S., Sabaka, T. J., Genova, A., Mazarico, E., Nicholas, J. B., and Neumann, G. A. (2017), Evidence for a low bulk crustal density for Mars from gravity and topography, *Geophysical Research Letters*, 44, 7686-7694, doi:10.1002/2017GL074172.
- Grott, M., and Breuer, D. (2010), On the spatial variability of the Martian elastic lithosphere thickness: Evidence for mantle plumes?, *Journal of Geophysical Research : Planets*, 115, doi:10.1029/2009JE003456.
- Head, J. W., Kreslavsky, M. A., and Pratt, S. (2002), Northern lowlands of Mars: evidence for widespread volcanic flooding and tectonic deformation in the Hesperian period., *Journal of Geophysical Research*(107), doi:10.1029/2000JE001445.

- Hinze, W., von Frese, R., and Saad, A. (2013), *Gravity and Magnetic Exploration Principles, Practices, and Applications.*, Cambridge.
- Hoogenboom, T., and Smrekar, S. E. (2006), Elastic thickness estimates for the northern lowlands of Mars., *Earth and Planetary Science Letters*, 248, 830-839.
- Kalousov, K., Souček, O., and Čadež, O. (2010), Global model of elastic lithosphere thickness of Mars, *European Planetary Science Congress 2010*, 5(EPSC2010-608).
- Khan, A., et al. (2021), Upper mantle structure of Mars from InSight seismic data, *Science*, 373(6553), 434-438.
- Knapmeyer-Endrun, B., et al. (2021), Thickness and structure of the martian crust from InSight seismic data, *Science*, 373(6553), 438-442.
- Kraus, H. (1967), *Thin elastic shells: An introduction to the theoretical foundations and the analysis of their static and dynamic behavior*, 467 pp., New York: John Wiley.
- Marinova, M. M., Aharonson, O., and Asphaug, E. (2008), Mega-impact formation of the Mars hemispheric dichotomy., *Nature*, 453, 1216-1219.
- McGovern, P. J., Solomon, S. C., Smith, D. E., Zuber, M. T., Simons, M., Wieczorek, M. A., Phillips, R. J., Neumann, G. A., Aharonson, O., and Head, J. W. (2002), Localized gravity/ topography admittance and correlation spectra on Mars: Implications for regional and global evolution., *Journal of Geophysical Research : Planets*, 107.
- McKenzie, D., Barnett, D. N., and Yuan, D. N. (2002), The relationship between Martian gravity and topography., *Earth and Planetary Science Letters*, 195, 1-16, doi:10.1016/S0012-821X(01)00555-6.
- Montgomery, D. R., Som, S. M., Jackson, M. P. A., Schreiber, B. C., Gillespie, A. R., and Adams, J. B. (2009), Continental-scale salt-tectonics on Mars and the origin of Valles Marineris and associated outflow channels, *Geological Society of America Bulletin*, 121, 117-133.
- Neumann, G. A., Zuber, M. T., Wieczorek, M. A., McGovern, P. J., Lemoine, F. G., and Smith, D. E. (2004), Crustal Structure of Mars from gravity and topography, *Journal of Geophysical Research*, 109(E08002), doi:10.1029/2004JE002262.
- Nimmo, F. (2002), Admittance estimates of mean crustal thickness and density at the Martian hemispheric dichotomy, *Journal of Geophysical Research E: Planets*, 107(11), doi:10.1029/2000je001488.
- Nimmo, F., and Tanaka, K. (2005), Early crustal evolution of Mars, *Annual Reviews of Earth and Planetary Sciences.*, 33, 133-161.
- Ojha, L., Smrekar, S., and D., N. (2014), Geophysical Investigation of the InSight Landing Site, in *45th Lunar and Planetary Science Conference*, edited, Virtual.
- Phillips, R. J., et al. (2001), Ancient geodynamics and global-scale hydrology on Mars, *Science*, 291, 2587-2591.
- Sleep, N. H. (1994), Martian plate tectonics, *Journal of Geophysical Research* 99, 5639-5655.
- Solomon, S. C., et al. (2005), New perspectives on ancient Mars., *Science* 307, 1214-1220, doi:10.1126/science.1101812.
- Thor, R. (2016), Mapping the Thickness of the Martian Elastic Lithosphere using Maximum Likelihood Estimation., 88 pp, Delft University of Technology.
- Turcotte, D., and Schubert, G. (1982), *Geodynamics Second Edition*, Cambridge University Press.

- Turcotte, D., Shcherbakov, R., Malamud, B., and Kucinskas, A. (2002), Is the Martian crust also the Martian elastic lithosphere?, *Journal of Geophysical Research : Planets*, *107*, doi:10.1029/2001JE001594.
- Turcotte, D., Willemann, R. J., Haxby, W. F., and Norberry, J. (1981), Role of membrane stresses in the support of planetary topography, *Journal of Geophysical Research*, *86*, 3951-3959, doi:doi.org/10.1029/JB086iB05p03951.
- Watters, T., McGovern, P., and Irwin, I. R. (2007), Hemispheres Apart: The Crustal Dichotomy on Mars, *Annual Reviews of Earth and Planetary Sciences*, *35*, 621-652, doi:10.1146/annurev.earth.
- Wessel, P., Luis, J. F., Uieda, L., Scharroo, R., Wobbe, F., Smith, W. H. F., and Tian, D. (2019), The Generic Mapping Tools version 6, *Geochemistry, Geophysics, Geosystems*, *20*, 5556-5564, doi:<https://doi.org/10.1029/2019GC008515>.
- Wieczorek, and Zuber, M. (2004), Thickness of the Martian crust: Improved constraints from geoid-to-topography ratios., *Journal of Geophysical Research : Planets*, *109*, doi:10.1029/2003je002153.
- Wieczorek, M. (2007), Gravity and Topography of the Terrestrial Planets., *Treatise on Geophysics*, (10), 165-206.
- Wieczorek, M. A., and Meschede, M. (2018), SHTools: Tools for Working with Spherical Harmonics, *Geochemistry, Geophysics, Geosystems*, *19*(8), 2574-2592, doi:10.1029/2018GC007529.
- Wieczorek, M. A., and Simons, F. J. (2005), Localized spectral analysis on the sphere, *Geophysical Journal International*, *162*(3), 655-675, doi:10.1111/j.1365-246X.2005.02687.x.
- Wilhelms, D. E., and Squyres, S. W. (1984), The martian hemispheric dichotomy may be due to a giant impact, *Nature*, *309*, 138-140.
- Zhong, S., and Zuber, M. T. (2001), Degree-1 mantle convection and the crustal dichotomy on Mars, *Earth and Planetary Science Letters*, *189*, 75-84.
- Zuber, M., Solomon, S., Phillips, R., Smith, D., Tyler, G., Aharonson, O., Balmino, G., Banerdt, W., Head, J., and Johnson, C. (2000), Internal structure and early thermal evolution of Mars from Mars Global Surveyor topography and gravity, *Science*, *287*, doi:10.1126/science.287.5459.1788.

VITA

Aspen Marie Davis

Education

B.S. Geophysical Engineering (2019)

Colorado School of Mines, 80401

Experience

Graduate Teaching / Research Assistant

Planetary Geophysics Lab

Department of Earth and Environmental Sciences

University of Kentucky, 40506

Undergraduate Research Assistant

Department of Geophysics

Colorado School of Mines, 80401